Novel Acquisition Strategies for Dissolution Dynamic Nuclear Polarisation

Thesis submitted to the University of Nottingham for the degree of

Doctor of Philosophy

Ben P. McGeorge-Henderson MSci (Hons)

May 21, 2017

Abstract

Dynamic Nuclear Polarisation (DNP) produced molecules with spin polarisation levels that are up to three orders of magnitude larger than their thermal equilibrium values. Most DNP mechanisms work at temperatures of 2 K and lower, meaning that the sample is stored in the solid-state. Combining DNP with a rapid temperature jump to room temperature allows liquid-state NMR analysis with a signal that is five orders of magnitude higher than observed with thermal polarisation. However, the information obtained during a dissolution experiment is limited by the intrinsic liquid-state longitudinal relaxation of the spins of interest. This thesis looks to increase the information acquired in a number of ways. First, by developing a new dissolution system for the dual iso-centre magnet it was possible to reproducibly perform enhanced NMR acquisition 600 ms following sample dissolution. This has allowed the observation of hyperpolarised ^{13}C spins with T_1 times as low as 200 ms. Complimentary information can be obtained following sample dissolution by observing multiple spin species simultaneously. ^{13}C and ^{15}N spins are both polarised by microwave irradiation of the same frequency, so both can be analysed during a single dissolution DNP experiment. A novel probe has been used that contains six individual ^{13}C microcoils. These coils are separated in space and operate independently. This probe, in conjunction with dissolution DNP, can be used for observing dynamic molecular information on the time scale of 200 ms, however with further development this time scale should drop to less than 100 ms while maintaining a required minimum spectral resolution. Initial tests have been performed with both thermally polarised and hyperpolarised samples.

Acknowledgements

An eminent scientist[1] is purported to have once said:

"If you judge a fish by its ability to climb a tree, it will live its whole life believing that it is stupid."

Well, as I speak to you now, from one of the lower branches of the great Oak academia, my scaly tail flapping in the gentle spring breeze, I hope this document stands as some evidence as to what a fish can achieve when it really doesn't know when to quit. However, such a feat of aquatic mountaineering is only possible with an elaborate and comprehensive set of ropes, carabiners, harnesses and other assorted pieces of adventurous equipment. Just such a set can be found within the walls of the Sir Peter Mansfield Imaging Centre[2], and not just the one under Fraser's desk. Without the individuals who inhabit the Centre on a daily basis I simply wouldn't have managed to get through it all.

I would like to start with Sankeerth Hebbar. One of the greatest human beings I have ever met. His kindness and infinite patience, even in the face of my ineptitude, still surprises me. Next is Edward Axell Breeds. Some part of me still believes he doesn't exist, and that my PhD was simply badly advertised and somewhat less exciting sequel to *Fight Club*. It's always nice to share the pain.

---

[1] The quote was first attributed to Einstein in the 2004 self-help book *The Rhythm of Life: Living Every Day with Passion and Purpose* by Matthew Kelly, however there is no evidence that the great man ever actually said it.

[2] née Magnetic Resonance Centre

The rest of the k-team: Adam of Gaunt, Dan Wisniefski, Jamie Barr (briefly, at least), James Wilman (wherever you are now), Jim Leggett, Peter Roberts, Grzegorz Kwiatkowski and Antonio Gennaro (I loved you the best). Those labs will be the end of us all.

And everyone else in the Centre: George, Simon, Andy, Clementine, Fraser, Ellie, Ben T, Ben H, Chrissy B, Elena K, Elena B, Olivier, Sam (Wharton), Jim, Mobeen, Lesley, Liz, Chen, Glynn, Molly, Nic, Matt Brookes, Matt Cronin, Tom Allen, David Lilburn, Joe Six. There are many more that I am forgetting here (its a neurological coping-mechanism). Everyone in the centre has helped me along the road.

My stupendously amazing girlfriend Jessica. You've had to put up with the fall-out of my frustrations and even in the lowest points, you've always made my day so much better.

I would also like to thank Graham Smith and Alexey Potapov for agreeing to conduct my *viva voce*. You made the experience much better than I ever would have expected. And, of course, I would like to thank my supervisor Walter Köckenberger for your support over these four years.

Thank you all for the kindness and fun. I suppose all that is left for me to do is remind you of the wise words of Admiral Ackbar:

"It's a trap!"

Dedication

Of course, this is dedicated to my mum and dad, whom, for reasons beyond the comprehension of science, allow me to pick that most awkward path and are continually there to pick up the pieces.

Contents

List of Figures

List of Tables

Acronyms

CE . . . . Cross Effect

CP . . . . Cross Polarisation

CPMG . . . . Carr-Purcell-Meiboom-Gill pulse sequence

dDNP . . . . Dissolution Dynamic Nuclear Polarisation

DNP . . . . Dynamic Nuclear Polarisation

EPR/ESR . . . . . . Electron Paramagnetic (Spin) Resonance

MAS . . . . Magic Angle Spinning

NMR . . . . Nuclear Magnetic Resonance

QOB . . . . Quasi-Optic Bench

SE . . . . Solid Effect

TJ-DNP . . . . Temperature Jump Dynamic Nuclear Polarisation

TM . . . . Thermal Mixing

ZBD . . . . Zero Bias Detector

1

Introduction

Nuclear Magnetic Resonance provides unparalleled access to the chemical world. NMR's ability to give both spectroscopic and structural information has rightly placed it as one of chemistry's top analytical tools. NMR exploits the effect that magnetic fields have on subatomic particles, and that energy-state population differences that arise from the subtle change in the energy levels of quantum spin states. These states represent the alignment of a component of the intrinsic angular moment (spin) parallel or anti-parallel with the externally applied magnetic field. This *Zeeman splitting* of energy levels is very small and hence the difference in the population of each level, which is governed by Boltzmann statistics, is almost imperceivable. Traditionally, to increase the observed NMR signal, scientists and engineers have pursued higher and higher magnetic field strengths in order to increase nuclear polarisation. Modern NMR magnets are made of advanced superconducting alloys that can easily produce magnetic fields on the order of tens of Tesla. However, it is becoming increasingly difficult to continue the trend and over the last decade scientists have been looking for other ways to increase nuclear polarisation.

This led back to the 1950s with the work of Albert Overhauser [1] and later Anatole Abragam and Maurice Goldman [2, 3]. Their work focused on the idea that the polarisation can be transferred between different subatomic particles. In samples that contain particles that are particularly susceptible to magnetic fields, such

as free-radical electrons, it is possible to transfer this polarisation onto other, less susceptible, spins. Electrons intrinsically have a polarisation which is nearly three orders of magnitude higher than any nucleus ($\gamma_{\text{electron}} > 660\gamma_{\text{proton}}$) so transferring electronic polarisation to any nucleus grants significant levels of signal enhancement. This is process is termed Dynamic Nuclear Polarisation (DNP).

Efficient DNP processes occur in cryogenically cooled solid-state samples. But in recent times, work pioneered by Jan Henrik Ardenkjær-Larsen *et al.* [4] demonstrated that that the signal could be enhanced further by rapidly heating the sample back up into the liquid state. The advantage of this technique is two-fold: Firstly the signal enhancement factor afforded by the temperature jump is a ratio of the initial and final temperature. This factor is multiplicative with that of the DNP; suddenly, nuclear enhancements that were on the order of hundreds were now in the tens of thousands. Secondly, once the sample is in the liquid state, molecular motion within the sample averages out anisotropic interactions and produces sharp spectral peaks. The heating method introduced by Ardenkjær-Larsen *et al.* involves heating and dissolving the cold sample with a super-heated solvent and then injecting it into a waiting NMR probe. For this reason, the technique developed was named dissolution-DNP

The limiting factor of the enhanced signal produced by dissolution-DNP is the liquid-state nuclear relaxation time T_1. Over the course of five T_1s the nuclear spin polarisation will return to its equilibrium state. For many molecules the enhanced signal will be entirely lost after only a few seconds. It is therefore imperative to acquire as much information about the sample as possible before the signal decays.

Initially, this document will introduce the relevant information required to understand the experimental work carried out. Chapter two presents the basic underpinnings of a NMR experiment and how theoretical frameworks have been cre-

ated to model the observed DNP processes. Following this, chapter three gives an overview of the instrumentation required to perform NMR and DNP experiments. Chapter four seeks to provide the context for how the system fits with the academic community at large and how experiments performed compare with those performed by other groups.

Chapters five, six and seven introduce the experimental work conducted during this project. This work seeks to explore three methods for increasing the data obtained from a dissolution-DNP experiment. Firstly, a new solvent delivery system has been devised to take full advantage of the dual iso-centre magnet here in Nottingham. The fast liquid-state nuclear relaxation processes begin as soon as the sample is melted, so by decreasing the time between dissolution and signal acquisition, more of the enhanced signal is retained and observed. Chapter 5 shows how this new set-up was designed and tested, along with a series of dissolution-DNP tests that demonstrate the ability of the system to acquire signals around 600 ms after dissolution. Two further methods are introduced in chapters 6 and 7. Rather than further optimising the dissolution process, these chapters describe novel acquisition strategies that attempt to increase the data obtained from a dissolution experiment.

Different spin species are effected differently by the microwave fields used to induce DNP. However some spins, such as ^{13}C and ^{15}N, demonstrate DNP profiles that overlap significantly. In such cases, experiments designed to polarise one of these spin species will automatically also polarise the other. Chapter 6 introduces the concept of multi-nuclear DNP as a method for obtaining multiple sets of complimentary nuclear information from a single dissolution experiment. The method has been used to acquired single scan spectral information from both ^{13}C and ^{15}N spins in N-Acetyl-L-Aspartic acid samples, with both spins at natural abundance.

Chapter eight develops the concept of using multiple channels to increase data ac-

quisition, this time by using six fully independent ^{13}C coils to acquire multiple sets of carbon data concurrently. The chapter describes the interfacing of the six-coil probe with the dissolution-DNP set-up. Initial simulations and results, based on dissolution DNP of spin labelled sodium acetate, suggest that the probe is capable of increasing the time resolution of dissolution experiments through staggered NMR acquisition.

Finally, chapter 8 presents the conclusions drawn from the performed experiments and outlines some of the future work required to develop the techniques further.

2

The Theory of Nuclear Magnetic Resonance

Nuclear Magnetic Resonance is a branch of Spectroscopy, which is here understood in it's broadest sense to encompass all studies of the nature of the energy levels of material systems and of the transitions between them through absorption or emission of electromagnetic radiation

— Anatole Abragam *The Principles of Nuclear Magnetism*

2.1 Introduction

Magnetic resonance (MR) techniques use magnetic fields to induce subtle differences in the populations occupying energy levels of atomic particles. *Nuclear Magnetic Resonance* (NMR) and *Electron Paramagnetic Resonance* (EPR) are fundamentally similar techniques, however they propose substantially different problems when it comes to practical implementation. The divergence of methods is mostly down to the difference in how strongly an electron and a nucleus experiences an externally applied magnetic field.

As will be discussed, Dynamic Nuclear Polarisation (DNP) requires the manipula-

tion of both nuclear and electron spins. Hence this composite technique demands an appreciation of both phenomena. This chapter will introduce the underlying physics of spin resonance for both nuclear and electron spin species and how they come together to form a nascent picture of DNP processes. The principles outlined in this chapter drive the design of NMR, EPR and DNP hardware, therefore they must be appreciated. It is, however, beyond the scope of this document to give a comprehensive description of all DNP theories.

2.1.1 The Nuclear Spin

The atomic nucleus is composed of the nucleons: protons and neutrons. These sub-atomic particles have non-zero magnetic moments and therefore interact with magnetic fields [5]. The external field provides an orientation dependent potential energy

$$E = -\vec{\mu} \cdot \vec{B}, \tag{2.1}$$

where $\vec{\mu}$ is the magnetic moment vector of the nucleon and $\vec{B}$ is the magnetic field vector [6, 7]. Both nucleons are spin-$\frac{1}{2}$ particles, therefore the magnetic moment vector included in equation 2.1 can only have two orientations: one with a component parallel to the external magnetic field vector $\vec{B}$; and one with a component anti-parallel. Using equation 2.1 to determine the energy associated with each orientation (or, from now on: *energy states*) it becomes apparent that they have different energies.

The nucleons require jumps between these energy states in order to try and minimise the force acting on them. In the quantum regime, jumps between energy states are mediated through the absorption and emission of photons. Planck's eponymous equation states that the energy of a photon and its frequency are linked by

$$E_{\text{photon}} = h\nu, \qquad\qquad (2.2)$$

where ν is the frequency and $\hbar$ is Planck's constant[1] [8].

As the energy gap that spans the jumps between energy states is well defined, so is the frequency of the photons that are emitted during these jumps. The energy gaps, and the emitted photons, are characteristic of the chemical environment of the nuclear spin, hence by observing and analysing these photons, spectroscopic information about these spins can be gathered.

Not all of the nucleons that make up the nucleus contribute to the interaction with an external field. As nucleons are Fermionic by nature, they are governed by the Pauli exclusion principle [9]. This asserts that two Fermions cannot occupy the same quantum state at the same time. In the nuclear shell structure, the nucleons will fill the available states from the lowest energy upwards. The nucleons are spin-half, so the degeneracy of the shell states is doubled and nucleons pair up as the shells are filled.

The different species of nucleon i.e. protons and neutrons, fill up separate nuclear shells. Nuclei that are comprised of equal numbers of both neutrons and protons will produce no observable spin effects. In situations where is an odd number of protons or neutrons or both then the spin of the nucleus will be non-zero and it will be observable using NMR. There are no steadfast rules for predicting the spin of a nucleus with an arbitrary combination of protons and neutrons, however for small nuclei, such as those used in this project, the nuclear spin can be obtained by finding which orbital state the odd nucleon occupies. In the case when there are an odd number of both protons and neutrons, the net spin of nucleus is a combination both spins. Whether the two spin states add or subtract from each other is

---

[1]$h = 6.6260700 \times 10^{-34} \, \text{J s}$

dependent on the parity of both states [10].

2.1.2 Spin precession

The Stern-Gerlach experiment performed in 1922 confirmed that some particles have intrinsic non-degenerate states in the presence of a magnetic field [11]. These states were determined to be evidence that particles had quantised angular momentum, like a spinning-top that can only spin at a small number of set rates. The development of the quantum theory of spin shows that this picture is not conceptually accurate; quantum spin has no classical equivalent, however the mathematics of the analogy broadly hold true for most experiments so this semi-classical picture has remained. In an external field, the quantum states are split along the magnetic field vector, however the magnetic moment of the spin is described as precessing around this vector at a characteristic rate, the *Larmor frequency*.

The Larmor frequency is dependent on the applied magnetic field strength and the extent to which the spin feels that field. It can be calculated using the equation

$$\omega_{\mathrm{n}} = \frac{-g_{\mathrm{n}}\mu_{\mathrm{N}}}{\hbar}B_0 = -\gamma B_0, \tag{2.3}$$

where

$$\hbar = \frac{h}{2\pi}. \tag{2.4}$$

Here the sensitivity of the nucleus to the field is governed by the g-factor of the nucleus (g_{n}) and the nuclear magneton (μ_{N}) which is the natural unit of nuclear magnetic moment[2]. The effects of these characteristics are usually bundled together into a single parameter that describes the strength of interaction with the magnetic field, the *gyromagnetic ratio*. Table 2.1 shows the gyromagnetic ratio, natural abundance and typical resonant frequencies for spins relevant to this project [12].

---

[2] $\mu_{\mathrm{N}} = 5.050783699 \times 10^{-27}$ J T^{-1}

The Larmor frequencies of nuclei are in the radio frequency range. This is important as it means that the energy of the photons both absorbed and emitted during quantum transitions will be in this RF regime. The hardware required for the production and detection of RF signals is discussed further in chapter 3.5.

Spin	γ (MHzT^{-1})	NA(%)	ω at 3.35 T (MHz)	ω at 9.4 T(MHz)
Hydrogen	42.576	100	142.63	400.21
Carbon-13	10.705	1.07	35.86	100.63
Nitrogen-15	−4.316	0.368	14.46	40.57
Free electron	−28024.95	100	93890	263000

Table 2.1: Gyromagnetic ratio for spin species that are relevant for this project. The gyromagnetic ratio is a phenomenological parameter relats the strength of the magnetic moment developed by a spin and the magnetic field that causes the moment to occur. The gyromagnetic ratio of the free electron is around 3 orders of magnitude larger than those of the nuclei, this is the basis of the separation between the disciplines of NMR and EPR.

2.1.3 The Electron Spin

Table 2.1 shows that the gyromagnetic ratio of the electron is significantly larger than that of the nucleus with the highest ratio: Hydrogen ($\gamma_{\text{electron}}/\gamma_{\text{hydrogen}} \approx$ 660). It also shows that the Larmor frequency of the electron, at typical field strengths, has moved out of the RF regime into the microwave regime. As will be discussed, this shift in frequency causes a substantial difference in experimental design [13].

The interaction between spins and the external field is usually orientation dependent. In this project, NMR spectra were predominantly obtained from samples in the liquid-state. In this state, the rapid molecular tumbling averages out the anisotropy of the chemical shifts and narrow resonances are observed. In the solid state this tumbling does not take place and the spectra obtained display resonances that are two or three orders of magnitude wider.
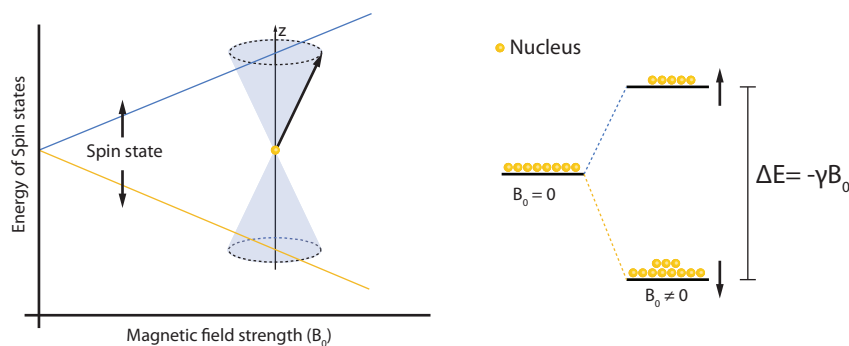
Figure 2.1: LEFT: *In the presence of a magnetic field, the spin states become non degenerate. The energy gap between the two levels is linearly dependent on the strength of the applied magnetic field.* RIGHT: *Once the spin states become non-degenerate, the equilibrium statistical distribution of spins between the two levels become unequal, with the lower energy state will having a small excess of nuclei. This discrepancy of populations is known as the polarisation of the ensemble. By perturbing an ensemble and observing its return to equilibrium, the nuclear environment can be probed.*

While the analysis of chemical shift anisotropy of nuclear spins is not a focus of this project, it is important to consider the various factors that broaden the spectra obtained from electronic spins as these factors provide information about which DNP pathways are being exploited during the experiment.

The orientational dependence of the electronic g-factor is characterised by its *g-tensor* [14]. This diagonal tensor provides the principal x, y and z components of the electron-field interaction:

$$
g_e = \begin{pmatrix} g_{xx} & 0 & 0 \\ 0 & g_{yy} & 0 \\ 0 & 0 & g_{zz} \end{pmatrix}.
\tag{2.5}
$$

In solid-state samples, anisotropy of the g-tensor gives rise to broad resonances for electrons that have z, x or y components aligned with the external field vector. Anisotropic interactions, such as the g-tensor, lead to broadening of the EPR line

shape. There are two distinct forms of line broadening in EPR spectra.

Homogeneous broadening

Homogeneous broadening is the distribution of electronic spin frequencies due to electron dipolar interactions that, averaged over time, affect all the electronic spins equally [15]. Homogeneously broadened EPR spectra display a Lorentzian distribution of frequencies for the observed spins. During an experiment, the saturation of such electron spins will be uniform over the spectral peaks. The width of a homogeneously broadened resonance provides information about the lifetime of the quantum states that produce the resonance. As will be discussed in a later section, the relaxation times play a crucial part of the study of magnetic resonance, including DNP.

Inhomogeneous broadening

Inhomogeneous broadening is the result of anisotropic and location dependent perturbations of the electronic energy states. Inhomogeneous effects, such as the g-tensor outlined above, provide a larger distribution of electronic resonances that generally approximate to a Gaussian distribution. Such spectra are made up of *spin packets* that act independently under microwave irradiation. It is possible to 'burn a hole' in an inhomogeneously broadened EPR spectrum by saturating spin packets of certain frequencies [16]. Upon continued irradiation, off-resonant spin packets close to the irradiation frequency will also begin to saturate through a process known as *spectral diffusion* [17]. This processes is mediated by the electronic dipolar interactions between neighbouring spin packets.

As will be discussed later in this chapter, the nature of the free radical electron has an impact on the forms of DNP that take place within the sample. By studying the characteristics of different free radicals it has been possible to design new free radical molecules that maximise the efficiency of DNP processes. A comprehensive review of the efficacy of a broad range of radicals can be found in [18].

2.1.4 Spin Polarisation

In the presence of an external field the energy associated with spins that are aligned with and against the field diverge. For nuclei that have a positive gyromagnetic ratio, the spins slightly prefer to orient themselves parallel with the field[3]. The problem them becomes one of statistical mechanics. An ensemble of spins in a sample is stopped from entirely populating the lower energy level by its thermal contact with the spin's local environment[4]. This input of energy means that the equilibrium distribution of spins in the different states follows the temperature-dependent Boltzmann distribution.

At room temperatures, the polarisation of an ensemble of spins is incredibly small. Manipulation of the Boltzmann distribution allows this polarisation to be calculated by

$$\frac{N_+ - N_-}{N_+ + N_-} = \tanh\left(\frac{\gamma \hbar B_0}{2 k_B T}\right), \tag{2.6}$$

where $N_\pm$ are the populations of the up (+) and down (-) nuclear spin states. T is the sample temperature and k_B is the Boltzmann constant[5].

For Hydrogen at room temperature (290 K), experiencing a reasonable field strength (3.35 T) there will be a spin polarisation of $1.18 \mathrm{x} 10^{-5}$. So only around 12 nuclear spins in every one million will contribute to the observed NMR signal. In the same conditions over 7700 electron spins will contribute to the EPR signal. Figure 2.2 shows the polarisation of spins as a function of temperature, at a field strength of 3.35 T. Below 2 K, the electron polarisation tends to unity.

---

[3]Conversely spins that display a negative gyromagnetic ratio, such as ^{15}N, will tend to orient anti-parallel with the field.

[4]Known as the lattice, a term which originated in sold-state NMR but has persisted in the lexicon of the liquid-state spectroscopist.

[5]$k_B = 1.38064852 \times 10^{-23} \mathrm{m^2\,kg\,s^{-2}\,K^{-1}}$
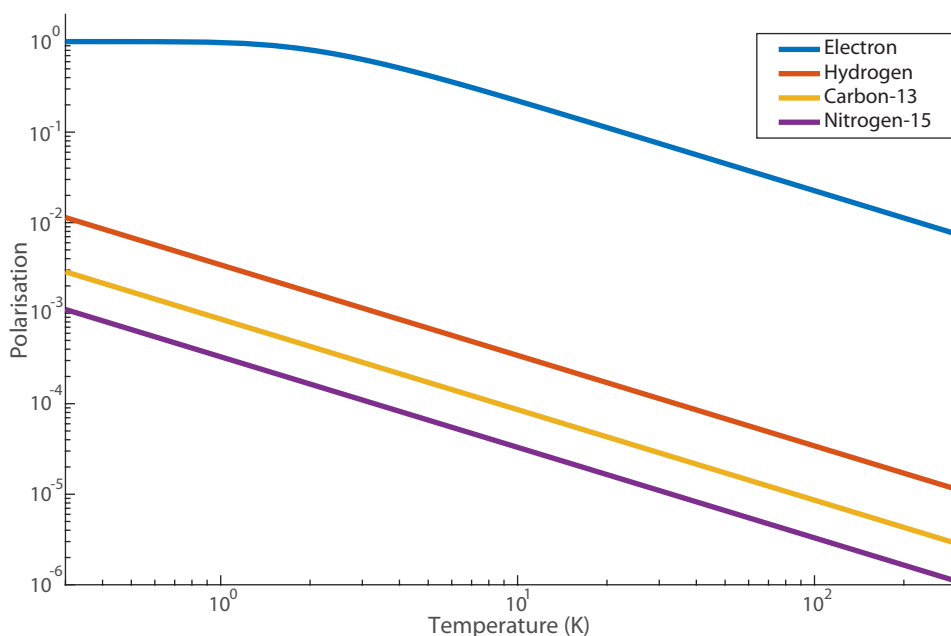
Figure 2.2: Boltzmann spin polarisation as a function of temperature - at a field strength of 3.35 T

2.1.5 The Magnetisation Vector

In equilibrium, the resultant magnetic moment of the ensemble of spins aligns with the magnetic field. Many of the macroscopic physical characteristics observed from an ensemble of spins can be explained by the manipulation of this *magnetisation vector*. It is important to note that the equilibrium that gives rise to the magnetisation vector is a dynamic equilibrium. Individual spins will be continually jumping between the possible energy states but across a large number of spins the average vector is maintained.

Convention states that the z-axis of the Cartesian coordinate system lies along the externally applied magnetic field vector. The plane orthogonal to the z-axis is referred to as the x-y plane. An important concept in this picture is the projection of vectors either onto the z axis or onto the x-y plane. In equilibrium, while there is a net magnetisation vector due to the slight polarisation of the spins, there is no quantisation or polarisation of spins in either the x or y directions. This means that

the magnetisation vector does not have a component in the x-y plane, it is parallel with the z axis. As will be discussed in later sections, NMR experiments use resonant coils to produce and observe magnetic fields that are orthogonal to the static magnetic field, in the x-y plane. To analyse the magnetic properties of nuclei, the bulk magnetisation vector must be rotated such that it has a components along one, or both, of the x and y axes. The dynamics of the magnetisation in the x-y plane can then be observed by the NMR spectrometer.

2.1.6 The Bloch Equations

The dynamics of the magnetisation vector are described mathematically by the *Bloch equations*. These equations, introduced by Felix Bloch in the 1940s, are essentially the equations of motion of a perturbed magnetisation vector [19]. The equations are generally presented independently for components along the x, y and z axes.

$$\frac{d\mathbf{M}_x}{dt} = \gamma(\mathbf{M}(t) \times \mathbf{B}(t))_x - \frac{\mathbf{M}_x(t)}{T_2}, \tag{2.7}$$

$$\frac{d\mathbf{M}_y}{dt} = \gamma(\mathbf{M}(t) \times \mathbf{B}(t))_y - \frac{\mathbf{M}_y(t)}{T_2}, \tag{2.8}$$

$$\frac{d\mathbf{M}_z}{dt} = \gamma(\mathbf{M}(t) \times \mathbf{B}(t))_z - \frac{\mathbf{M}_z(t) - M_0}{T_1}. \tag{2.9}$$

Here $\mathbf{M}(t)$ is the dynamics of the magnetisation vector and $\mathbf{M}(t)_i \{i = x, y, z\}$ are the components along each axis. $\mathbf{B}(t)_i \{i = x, y, z\}$ are the time dependent components of the applied magnetic field. Before and after the pulse the components $\mathbf{B}(t)_x$ & $\mathbf{B}(t)_y$ will be zero. The dissipative terms at the end of each equation drive the system back to its equilibrium. These terms are descriptors for all of the relaxation processes that return the spins back to their preferred states. The terms T_1 and T_2 are characteristic relaxation rates and are fundamental to both DNP and

NMR in general. The physical basis for spin relaxation requires insight into the various interactions and fluctuations that dissipate energy within the system. Models quantitatively predicting the processes of nuclear spin relaxation are continually being theorised and improved upon [20, 21]. However, combining all of the various sources of spin relaxation into two phenomenological processes is adequate for an experimentalist's approach to NMR.

2.1.7 Longitudinal relaxation

By rotating the magnetisation vector, the system is pushed away from its equilibrium. Longitudinal relaxation encompasses the relaxation processes that return the z component of the magnetisation vector to its equilibrium magnitude. This is an important characteristic for DNP experiments as it indicates the lifetime of any hyperpolarisation that is bestowed onto nuclear spins. Longitudinal relaxation is a process that is based on energy exchange between the spin ensemble and its environment. It can be measured through an inversion recovery experiment. During this experiment, the initial equilibrium magnetisation vector is rotated 180° by a pulse. This pulse is followed by an evolution time t_{inv} and a second pulse, this one 90°. By varying t_{inv} the signal can be fitted to the equation

$$M(t_{inv}) = M_0 \left[1 - 2 \exp\left(\frac{-t_{inv}}{T_1} \right) \right].$$

(2.10)

This experiment is shown in figure 2.3.

2.1.8 Transverse relaxation

When there is no orthogonally applied B_1 field perpendicular from the axis of the static field, there is no quantification of the angular momentum. This means that the magnetisation vector can have any orientation on the x-y plane. However, immediately after a pulse, the magnetisation vectors of individual spins are correlated along a certain direction[6]. However, the lattice is a dynamic system. Molecular

---

[6]For example, after a $\left(\frac{\pi}{2}\right)_x$ pulse, the magnetisation vectors will sum to point along the y axis.
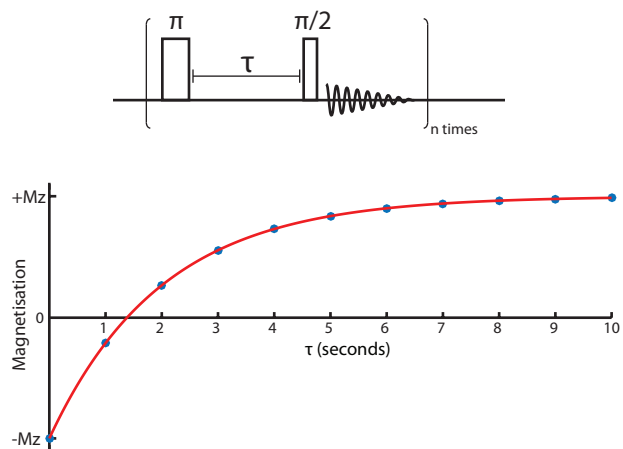
Figure 2.3: TOP: T1 can be measured through an inversion recover experiment. The pulse sequence of the inversion recovery is shown. An initial π pulse inverts the magnetisation from its equilibrium value. After a delay τ a $\frac{\pi}{2}$ pulse transfers some of the magnetisation into the x-y plane for observation. The phase and magnitude of the observed signal is dependent on how much the magnetisation vector has recovered towards it equilibrium value. BOTTOM: By incrementing the delay τ across successive scans, the relaxation dynamics of the magnetisation vector can be observed. The data can then be fitted with equation 2.10. This simulation shows 10 data points acquired at 1 s intervals, in this case the spin has a T_1 time of 2 s.

motion, neighbouring spin and lattice vibrations mean that the local magnetic field experienced by an individual spin is constantly changing. As the procession frequency of the spin is field dependent, any variations in the local field will produce different rates of procession. On the time-scale of an NMR experiment, these fluctuations in field will be averaged, meaning that the local spin has an effective procession frequency which is close to the chemically-shielded Larmor frequency of that spin. Across the ensemble there are will be a range of these different procession frequencies, meaning that during the procession that follows a NMR pulse, there will be a 'fanning out', or dephasing, of the individual magnetisation vectors. This loss of ensemble coherence is known as the transverse relaxation. As the fanning occurs, the magnitude of the total magnetisation vector in the x-y plane decreases until it disappears entirely. Spin ensembles that experience a wider range of fields
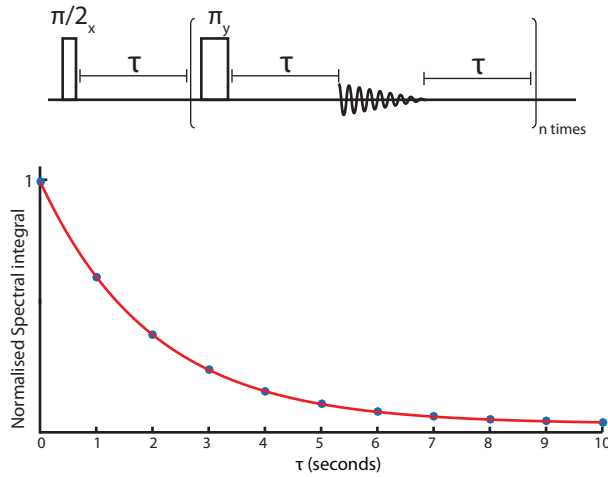
Figure 2.4: TOP: The Carr-Purcell-Meiboom-Gill (CPMG) pulse sequence. The CPMG sequence uses a train of π pulses to create a succession of spin echoes. The integrals of these spin echoes will decay at a rate of $1/T2$. BOTTOM: Simulated decay of normalised signal integral during the CPMG sequence. This simulation show the decaying signal with a T2 time constant 2 s.

will dephase more quickly.

This process of dephasing can be corrected by applying a π pulse after the initial $\pi/2$. This inverts the magnetisation vector in plane; a magnetisation vector which was placed along y after the first pulse will be aligned along -y after the second. The various magnetic fields, which caused the initial dephasing, now work in reverse to realign and producing a spin echo. The advantage of spin echoes is that they remove many of the line broadening effects of the imperfect NMR system. They can be formed because the nuclear T_2 relaxation time is always shorter than the T_1 time.

T_2 versus $T_2{}^\star$

Decades of engineering have gone into improving the NMR system, however it remains imperfect. The observed transverse relaxation of a sample of interest is not purely down to inter- and intra-nuclear effects. Other parameters such as the homogeneity of both the static magnetic field and applied pulses will subtly distort

the ideal case. The *effective* transverse relaxation is then the combination of both the nuclear and external effects and is denoted as T_2^* [22]. T_2^* is always shorter than T_2, and is the cause of the envelope of the free induction decay observed during an experiment.

2.2 Quantum mechanical description of Spin

The classical description of a magnetisation vector is useful for visualising many of the observations made during MR experiments. However it does not describe the underlying physical principles of what takes place during such experiments. Rather, a purely quantum 'bottom-up' approach is required to fully understand the system and its dynamics.

This process looks at spins individually first and then builds up the picture to include interactions between spins in the sample. By creating operators such as the Hamiltonian and then applying them to the wave-function of the system, it is possible to mathematically extract information that is analogous to that found in a NMR experiment.

2.2.1 Spin Operators

The mathematical constructs that describes a spin's interaction with the external field are known as the Pauli matrices. These matrices are usually presented in terms of the x, y and z components with respect to the applied magnetic field vector:

$$\hat{I}_x = \frac{1}{2}\begin{pmatrix} 0 & 1 \\ 1 & 0 \end{pmatrix}, \qquad \hat{I}_y = \frac{1}{2}\begin{pmatrix} 0 & -i \\ i & 0 \end{pmatrix}, \qquad \hat{I}_z = \frac{1}{2}\begin{pmatrix} 1 & 0 \\ 0 & -1 \end{pmatrix}. \qquad (2.11)$$

These terms can be used in the construction of other operators to define component specific terms. For example, these matrices are fundamental to the creation of a

Hamiltonian for an ensemble of spins in which terms such as the splitting of energy levels is orientation dependent.

2.2.2 The Density Matrix

One of the postulates of quantum mechanics is that before measurement, the wave-function that describes a system is constructed as a superposition of all its possible eigenstates

$$|\Psi(t)\rangle = \sum_{n=1}^{N} c_n(t) |n\rangle, \tag{2.12}$$

where $|c_n|^2$ is the probability of finding the particle in state $|n\rangle$. It is therefore possible to calculate the probabilities of a spin being in a certain state by computing the outer product of the wave-function [23]:

$$\hat{\rho} = |\Psi\rangle\langle\Psi| = \begin{pmatrix} c_1 \\ c_2 \\ \vdots \\ c_n \end{pmatrix} \begin{pmatrix} c_1^* & c_2^* & \cdots & c_n^* \end{pmatrix} = \begin{pmatrix} c_1 c_1^* & c_2 c_1^* & \cdots & c_n c_1^* \\ c_1 c_2^* & c_1 c_1^* & & \\ \vdots & & \ddots & \\ c_1 c_n^* & & & c_n c_n^* \end{pmatrix}. \tag{2.13}$$

For ensembles of N spins, the wave-function of the system will be a Kronecker product of all the individual wave-functions of individual spins,

$$|\Psi\rangle_{\text{ensemble}} = |\Psi_1\rangle \otimes |\Psi_2\rangle \cdots \otimes |\Psi_N\rangle \tag{2.14}$$

The resultant density matrix of such an ensemble will have dimensions of $M^N \times M^N$ where M is the number of accessible states for each spin e.g. 2 for spin-$1/2$ particles. The dynamics of a spin ensemble can be determined through the Liouville-von Neumann equation

$$i\hbar \frac{\partial \hat{\rho}}{\partial t} = \left[\hat{H}, \hat{\rho} \right]. \tag{2.15}$$

where $\left[\hat{H}, \hat{\rho} \right]$ is the commutation of the density matrix and the Hamiltonian which describes the total energy of the spin system. The density matrix fully describes the

probability distribution of the spin ensemble. Therefore it can be used to determine expectation values of the system. By taking the trace of the combined density matrix and spin operator the expectation value of that operator is returned, following the equation

$$\langle \hat{I}_Z \rangle = \text{Tr} \left(\hat{\rho} \hat{I}_z \right).$$ (2.16)

Calculating this value gives the likely outcome that will be observed during an experiment.

2.3 Hamiltonians

In quantum systems, the Hamiltonian of a system describes the total energy of that system [24]. For the case of magnetic resonance, only energies that are directly related to interactions with the external magnetic field and with other magnetic moments within the sample are needed. For DNP, the spin ensembles encountered contain both electronic and nuclear spins so contributions from both species need to be used in the construction of the Hamiltonian. When dealing with both nuclei and electrons it is customary to label nuclear terms I and electronic terms S. The Hamiltonian $\hat{H}$ of a spin system in a magnetic field is given as:

$$\hat{H} = \hat{H}_{ZS} + \hat{H}_{ZI} + \hat{H}_{II} + \hat{H}_{SI} + \hat{H}_{SS},$$ (2.17)

where

- $\hat{H}_{ZS}$ - electronic Zeeman interaction with the external field,

- $\hat{H}_{ZI}$ - nuclear Zeeman interactions with the external field,

- $\hat{H}_{II}$ - interactions between nuclear spin,

- $\hat{H}_{SI}$ - interactions between electrons and nuclear spins,

- $\hat{H}_{SS}$ - interactions between electrons.

Zeeman Hamiltonian

Nuclear Zeeman

As has been introduced, in the presence of a magnetic field the energy associated with the nuclear spin states becomes non-degenerate. In its most basic form the nuclear Zeeman Hamiltonian of a single nuclear spin, in a field B_0, is of the form:

$$\hat{H}_{ZI} = -\gamma B_0 \hat{I}_z = -\omega \hat{I}_z,$$ (2.18)

where γ is the gyromagnetic ratio of the nuclear spin species and ω is its Larmor procession frequency. This expression be extended by the inclusion of the chemical shift of the nucleus. This is included as a factor of the external field as

$$\omega = -\gamma B_{\text{effective}} = -\gamma(1 - \sigma)B_0.$$ (2.19)

Chemical shift is the spectroscopic basis of NMR. Isolated spins resonate perfectly at a frequency provided by equation 2.18. If all spins output photons of this frequency then the determination of different spins would not be possible. Shielding of the external magnetic fields by the chemical environment subtly shifts the observed frequency of the spins, creating an effective magnetic field ($B_{\text{effective}}$) which is different to the static field. The shift is described by the chemical shielding value σ and is small compared to the resonant frequency of the nucleus hence chemical shifts are normally quoted in units of parts per million (ppm) of the frequency calculated in equation 2.18.

Electronic Zeeman

Electrons are affected by the external magnetic field to a much greater degree, this plays out as an much larger value of the electron's gyromagnetic ratio. It also means that the orientational dependence of the interaction between the electron and the field can not be neglected.

$$\hat{H}_{ZS} = -\mathbf{g}\mu_B B_0 \hat{S}_Z, \tag{2.20}$$

where $\mathbf{g}$ is the anisotropic g-tensor (discussed in §2.1.3) and μ_B is the Bohr magneton[7].

2.3.1 Ensemble of spins

The Hamiltonians presented above are for individual spins. To mathematically consider an ensemble of spins, each spin would have its own associated Zeeman energy, these terms simply sum together. The individual spin also cause fields that effect their local spin neighbourhood. These effects are described mathematically by the various interaction Hamiltonians.
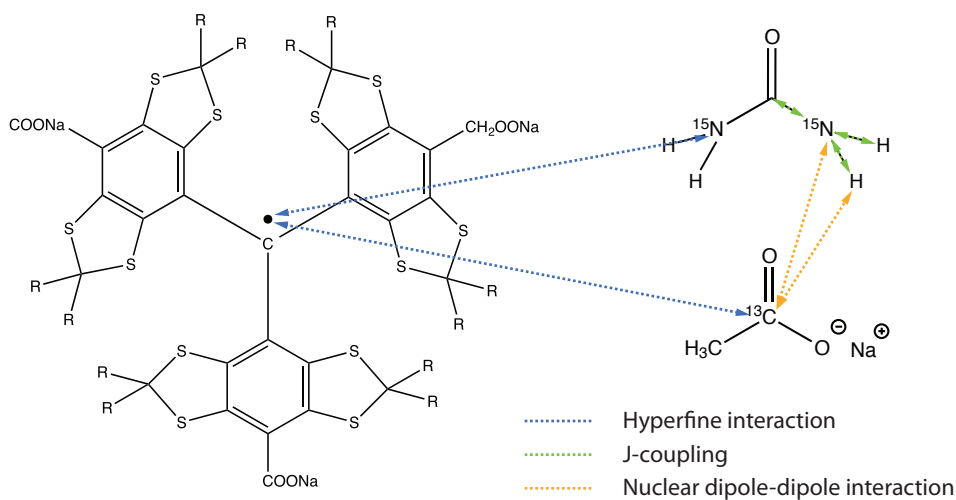
Figure 2.5: In a sample that contains multiple spin species, interactions between the spins, as well as the Zeeman interaction with the external field, will affect the energy levels of each spin. Here the free-radical electron spin on Trityl-OX63 (left) and the nuclear spins of Urea (right, top) and Sodium Acetate (right, bottom) are labelled with examples of the main inter-spin interactions. Quadrupolar interactions have been neglected in this diagram as they are not relevant to this project.

---

[7]$\mu_B = 9.27400 \times 10^{-24} \, \text{J T}^{-1}$

Nuclear J-coupling

Intra-molecular interactions between spins is known as J-coupling and is mediated through the electrons that form the chemical bonds. For an s-orbital electron that forms part of the chemical bond, there is a non-zero probability that it will overlap with the nucleus, this is known as the Fermi contact term. This means that the spin state of a nucleus has an effect on that of the covalently shared electron. The Pauli exclusion principle then forces the second covalently shared electron into the opposite spin state where its own Fermi contact term affects the second nuclear spin. The value of this interaction is entirely dependent on the characteristics (such as length and angle) of the covalent bond, however this parameters can be bundled together in to a single, interaction specific, coefficient J, which has the units of Hertz. The Hamiltonian of the J-coupling interaction is

$$\hat{H}_J = 2\pi J \hat{I}_{Z_1} \hat{I}_{Z_2}, \tag{2.21}$$

where J is the strength of the J-coupling. J-coupling is the cause of the splitting of spectral peaks into multiplets in NMR experiments, the value of J can be measured by the frequency difference between the individual peaks of a multiplet pattern.

Dipolar interactions

In an ensemble of spins, each individual spin acts as a magnetic dipole, the fields of which will directly interact with its local neighbourhood through space. These dipole-dipole interactions are the basis of many of the observations made during the DNP experiment, including the polarisation transfer itself. The general equation for dipolar interaction Hamiltonian, between two spins I and S, is

$$\hat{H}_{DD} = -\frac{\mu_0 \gamma_I \gamma_S \hbar}{4\pi r^3} \left(\hat{I} \cdot \hat{S} - \frac{3}{r^2}(\hat{I} \cdot \hat{r})(\hat{S} \cdot \hat{r}) \right), \tag{2.22}$$

where $\hat{r}$ is the inter-spin vector. Expanding 2.22 provides an extensive 'dipolar alphabet' which full characterises the interaction between the two spins. However, at

modern NMR field strengths, not all of the terms are necessary for understanding the dynamics of these interactions during an experiment [25]. The useful terms are those that commute with the Zeeman Hamiltonian of the observed spin, this is known as the secular approximation of the interaction. This approximation shows that only interactions that are parallel to the applied magnetic field will be observed during the experiment. Dipolar interactions are orientation dependent, this means that in liquid-state samples the rapid tumbling of the molecules quickly averages the interactions out to zero. They are therefore not observed in the majority of liquid-state NMR experiments. In the solid-state, the molecules will not be tumbling rapidly enough to remove them from acquired spectra. Analysis of these interactions in the solid-state is extensively used to determine structural properties of molecules.

Nuclear dipole-dipole interaction

The nuclear dipole-dipole interaction is the through space coupling of two nuclear spins, following the secular approximation presented above, the Hamiltonian is given by

$$\hat{H}_{II} = \frac{\mu_0 \gamma_1 \gamma_2 \hbar (1 - 3\cos^2\theta)}{4\pi r^3} \left[\hat{I}_{Z_1} \hat{I}_{Z_2} - \frac{1}{4} \left(\hat{I}_{+_1} \hat{I}_{-_2} + \hat{I}_{-_1} \hat{I}_{+_2} \right) \right], \qquad (2.23)$$

where

$$\hat{I}_{\pm} = \hat{I}_x \pm i\hat{I}_y. \qquad (2.24)$$

The dipolar coupling between nuclear spins allows energy-conserving 'flip-flops' to exchange magnetisation between the spins. In solid-state samples at thermal equilibrium, this effect can be observed through multi-dimensional spectroscopy, and provide important structural information. However, during DNP experiments spin diffusion also plays an important role in transferring the enhanced polarisation from 'core' nuclei that are close to the free electrons to the 'bulk' nuclei that make up the majority of the lattice.
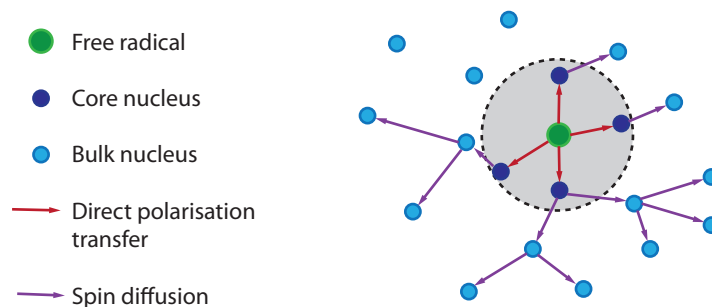
Figure 2.6: Illustration of spin diffusion for DNP. The free radical electron, in green, will directly polarise the nearby 'core' nuclei through the applied DNP pathway. As the hyperfine interaction between the electrons and nuclei are distance dependent, the effects of this interaction will be limited to a shell with a finite radium. Nuclei within this radius will therefore be directly polarised. Nuclei outside of this radius will not effected enough by the electron to induce a build-up of polarisation. Rather, the core nuclei will radiate out polarisation through spin diffusion.

Dipolar Hyperfine Interactions

The dipolar interaction between electronic and nuclear spins is known as the hyperfine interaction. In nuclear-nuclear couplings, the secular approximation holds because the coupling strength is around five to eight orders of magnitude smaller than the nuclear Zeeman interaction [26]. However, in the hyperfine interaction, the interaction strength between the electron and the nucleus is only two orders of magnitude smaller than the nuclear Zeeman interaction and cannot be ignored. This means that additional terms are included in the dipole hyperfine interaction, this is the pseudo-secular approximation.

$$\hat{H}_{SI} = \frac{\mu_0 \gamma_1 \gamma_2 \hbar}{4\pi r^3} \left[A\hat{I}_z\hat{S}_z + B_\pm \hat{I}_\pm \hat{S}_z. \right],$$ (2.25)

where r is the inter-spin distance and θ is the angle between them with respect to the z-axis. The coefficient A is

$$A = \left(1 - 3\cos^2\theta\right), \qquad (2.26)$$

for the same reason that it appears in equation 2.23. The additional term of equation 2.25, with coefficient $B_\pm$ is the result of the pseudo-secular approximation. These terms arise because the electronic Zeeman state has an influence on the quantisation axis of the nucleus, tipping the nuclear spin state vector into the transverse plane. Mathematically, this term is defined as

$$B_\pm = -\frac{3}{2}\sin(\theta)\cos(\theta)e^{\mp i\phi}. \qquad (2.27)$$
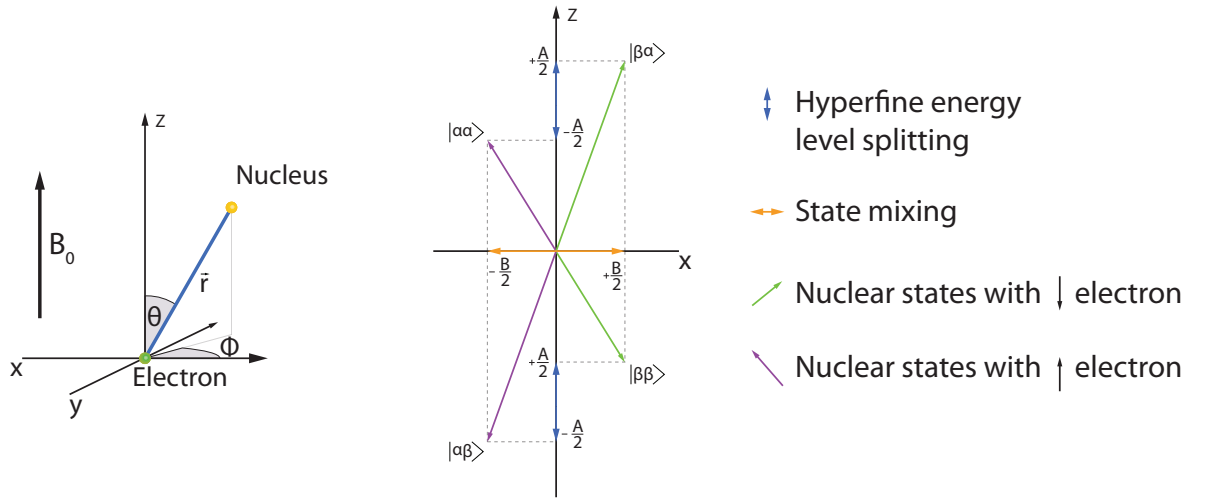
Figure 2.7: LEFT: The geometric parameters used in the hyperfine Hamiltonian. RIGHT: The nuclear quantisation axis is different depending on the electronic spin state. The hyperfine coefficient A describes the change (of $\pm\frac{A}{2}$) in z-projection of the magnetisation vector due to the electronic state. Coefficient B shows how much of the nuclear quantisation axis is tipped into the x-y plane. It is the mixing of states caused by this tipping that allows some of the quantum transitions that are exploited during a DNP experiment. This will be discussed further in section 2.5.

Electron-electron interaction

The dipolar interaction between electron spins is analogous to that between nuclei. Again it takes the form given in equation 2.22. Dipolar interactions between

electrons plays a crucial role in mediating DNP processes such as Cross Effect and Thermal Mixing. The components of the electron dipolar interaction that need to be retained to simulate the spin dynamics depends strongly on the type and concentration of the free electrons being observed. Information about how inter-electron distances alter DNP processes has lead to the development of bi-radicals that increase nuclear polarisation by modulation of the electronic dipole interaction [18].

2.4 The NMR experiment

2.4.1 Radio Frequency Pulses

In the early days of NMR, the B_1 field was applied as a continuous wave (CW). In order to excite all transitions within the sample, either the B_1 field frequency, or the static B_0 field was slowly swept across the expected chemical shift bandwidth. In such experiments, the sweep needs to be slow to adequately excite each resonance in the sample.

By applying short, high-power r.f. pulses to the sample it is possible to excite the full range of resonances in one go. The bandwidth of such a pulse is inversely proportional to its duration:

$$\Delta = \frac{1}{4t_p} \tag{2.28}$$

where t_p is the pulse duration (usually on the order a few μs). In the magnetisation vector model of an ensemble of spins, such pulses rotate the vector from its equilibrium position along the z axis. The angle, θ, through which the vector rotates is known as the flip angle of the pulse and is defined as

$$\theta = \gamma B_1 t_p, \tag{2.29}$$

where γ is the gyromagnetic ratio of the spins being manipulated and B_1 is the strength of the magnetic field applied orthogonally to the static field.

Typically, spectrometers allow the control of two aspects of the pulse to determine its flip angle: duration and pulse power[8]. The duration is equivalent to t_p in equation 2.29. The pulse power, defined either directly in Watts or in amplifier attenuation is a measure of the amount of current that is being sent through the NMR probe. Pulse power and B_1 field strength are related through the characteristics of the NMR probe being used, this will be discussed at more length in chapter 3.5. An understanding of how pulse power translates into applied magnetic field is not necessary for most experimental conditions where the relevant information can be determined by calibrating the $90°$ pulse for the probe. This involves fixing one of variable parameters of equation 2.29 and acquiring a set of spectra while varying the other. The number of observed spins is proportional to $\sin(\theta)$, so by incrementing one variable the integrals of the obtained spectra should vary sinusoidally. The useful parameters of the $90°$ and $180°$ flip angles can be used to determine the flip angle of any arbitrary modulation of the pulse parameter that was initially incremented.

Pulse Power in Hertz

When using equation 2.29 it is clear that different combinations of pulse power and duration can achieve the same flip angle. It is therefore useful to define the 'speed' at which the rotation occurs. In the rotating frame, the on-resonance oscillating rf-pulse acts like a top hat function with the effective B_1 field being turned 'on' for the pulse duration. During the pulse, the magnetisation vector will process around the B_1 axis in the same way it does around the static field in the laboratory frame. This rotation can be characterised as the time it takes for the magnetisation vector to perform a complete $360°$ rotation about the applied axis. As this time in on

---

[8]The phase of the pulse is crucial to some types of NMR experiment and it is also controlled by the spectrometer. However a consideration of phase in not necessary for this project.

the order of 10^{-4} s, it is preferred to give the number of rotations that would be completed in one second, in units of Hertz. Once this number is obtained then it becomes straightforward to determine the pulse duration necessary to obtain a 90$^\text{o}$ pulse.

2.4.2   The Free Induction Decay

The Free Induction Delay (FID) is the experimentally observed outcome of the Bloch dynamics of the magnetisation vector. FIDs form the basis for many of the observations made in NMR experiments. As such, the oscillating magnetic field produced by the nuclear spins induce an Electromotive force (emf) on the resonant coil. This voltage can then be recorded by the spectrometer. The resonant coils used in NMR experiments are designed to produce, and subsequently detect, magnetic fields that are orthogonal to static magnetic field B_0. The induced voltage is representative of those orthogonal fields and hence are an observation of a components of the magnetic field in the x-y plane. A complete FID contains complex information that represents both the x component and y component of the magnetisation separately. Figure 2.8 shows how the x and y components of the Bloch equations are observed as the real and imaginary components of the FID. T_2 relaxation causes both components to decay to zero.

2.4.3   The Fourier Transform

The Fourier Transform (FT) is the mathematical tool that allows signals resolved in time to be broken down into a sum of frequency components [27]. In cases where the observed signals are composed of a finite number of discrete frequencies (such as NMR) the Fourier transform reveals the spectroscopic information. In MRI experiments, the Fourier transform gives a set of spatial frequencies that, when combined, produce an image of the sample. In NMR spectroscopy, the frequencies obtained from the Fourier Transform are the set of transitions with energies described by the nuclear Hamiltonian discussed in section 2.3.
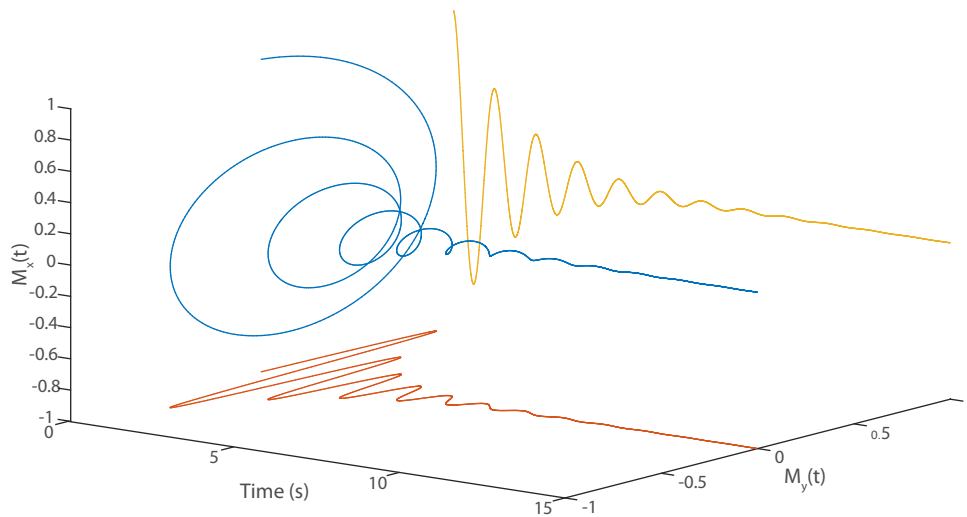
Figure 2.8: BLUE: 3D plot of x and y magnetisation as a function of time following a NMR pulse. ORANGE & YELLOW: x and y projections of the magnetisation as a function of time following a NMR pulse. In this simulation a magnetisation vector was constructed with a procession frequency of 1 Hz. The evolution of vector was simulated using the Bloch equations with a characteristic T_2 relaxation time constant of 3 s.

The relationship between a time domain function $F(t)$ and its frequency domain counterpart $G(\nu)$ is given mathematically by

$$G(\nu) = \int_{-\infty}^{\infty} e^{-2\pi i\nu t} F(t) dt. \tag{2.30}$$

This equation shows the continuous Fourier transform. In practice the discrete Fourier transform is used. This transformation provides frequency components of a finite number of frequency bins within your spectral window. As will be discussed in section 3.5 the width of the bins, and hence the resolution of the resulting spectrum, is dependent on the acquisition parameters of the spectrometer.
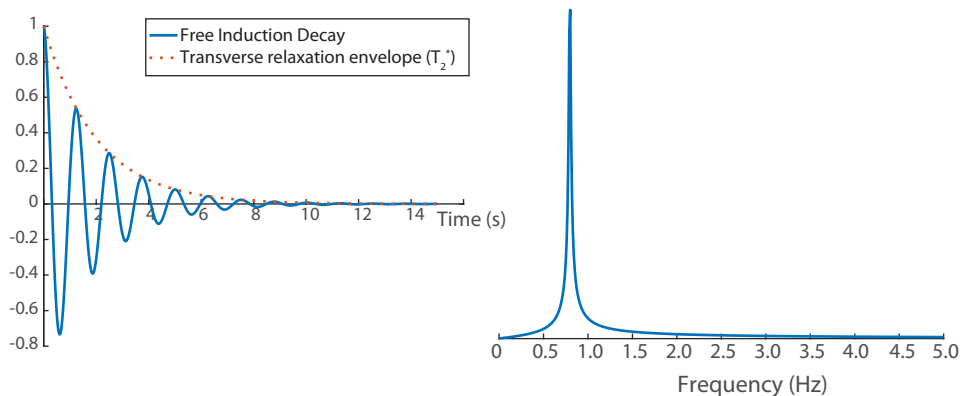
Figure 2.9: Example of a Free Induction Decay (FID) and spectrum obtained through the Fourier transform. LEFT: The envelope of the signal shows an exponential decay with a time constant T_2^*. RIGHT: The spectrum obtained through the Fourier transform of the FID. The broadening of the peak is due to T_2^*. This relaxation is the combined effect of the rate of dephasing of the nuclear spins and the dispersion of Larmor frequencies caused by inhomogeneities of the static magnetic field

2.5   Dynamic Nuclear Polarisation

Dynamic Nuclear Polarisation (DNP) was first proposed by Overhauser in the 1950s. He stated that nuclei in metals would display significantly larger spin polarisation if conduction band electrons were magnetically saturated [1]. Overhauser's theories were experimentally verified by Carver and Slichter [28]. Later, Abragam and Goldman discovered similar processes in other solids [2]. At the time however, microwave technology was not capable of taking full advantage of these DNP effects.

The real renaissance in DNP was trigger by two separate developments, first the work of Griffin and co-workers in MIT in incorporating DNP into solid-state Magic Angle Spinning (MAS) NMR [29]. Signal enhancements of around 40 were observed in ^{13}C signals produced by polystyrene doped with BDPA. The second development came with the first dissolution DNP experiments performed by Jan Henrik Ardenkjaer-Larsen and co-workers in Malmø [4, 30]. Using a fast dissolu-

tion system meant that the polarisation gain from the DNP effects could be supplemented further by a rapid temperature change. The dissolution process requires that the time taken for temperature jump and sample transfer is on the order of, or quicker than, the liquid-state nuclear T_1 time of the molecule of interest. When the dissolution time is significantly faster than nuclear relaxation, then the maximum possible polarisation enhancement from the temperature jump is simply the ratio of the two temperatures[9].

The sections below will go into detail about some of the principle effects that are thought to contribute to the polarisation enhancement of nuclear spins at cryogenic temperatures. It is important to note, however, that these theories are simplified models based on the interactions between the electrons and the nuclear spins. Experimentally, combinations of these and perhaps other effects will increase the nuclear signal. As will be shown, the models that are used to predict DNP effects are extremely dependent on sample composition, applied magnetic field, sample temperature etc.

2.5.1 The Solid Effect

The Solid Effect (SE) is the simplest of the proposed low-temperature DNP mechanisms [31]. It can be modelled by a two-spin system containing one electron and one spin-$\frac{1}{2}$ nucleus. In the solid state, the hyperfine interaction described in section 2.3.1 is not averaged out, so the mixing of states remains. Figure 2.10 shows the four energy levels associated with a nucleus coupled to a free radical electron [26]. There are six possible transitions between the four levels. First there are four single quantum transitions which describe the absorbed and emitted photons associated with NMR and EPR experiments. There are also two further transitions that involve both spins simultaneously changing state. These transitions are known as *for-*

---

[9]This assumes that the applied magnetic field remains constant throughout the experiment. In practice, the dissolution procedure transfers the sample between two magnets. In this case the change in field also needs to be included.

bidden transitions as they demonstrate single processes during which the magnetic quantum number does not change by one ($\Delta m_s \neq 1$). During these forbidden transitions, the magnetic quantum number changes by zero or two. For this reason these transitions are known as the zero quantum transition (ZQT: $\Delta m_s = 0$) and the double quantum transition (DQT: $\Delta m_s = 2$).
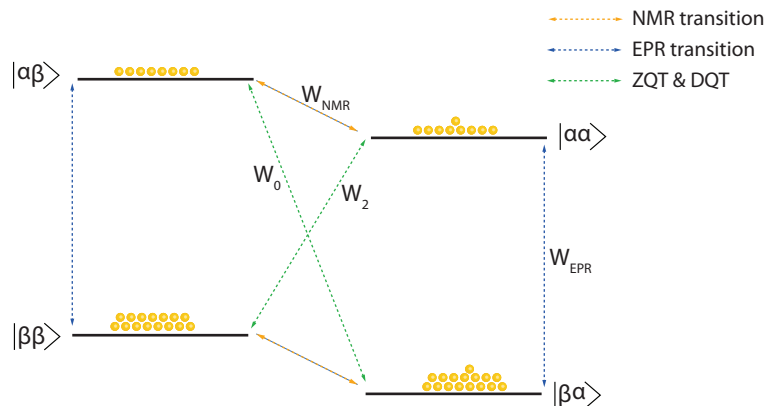
Figure 2.10: The four level system used in the Solid Effect description of DNP. Before the inclusion of the hyperfine interaction, the four states that make up this diagram are 'pure' states that are simply made of combinations of the up and down states of each spin. Upon its inclusion, the hyperfine interaction mixes the energy states such that there is a small amount of admixture of the neighbouring state. This subtly allows the previously forbidden transitions such that the application of microwaves at these transitions will drive the transfer of polarisation from the electron onto the nucleus.

For a four level system constructed of pure spin up and spin down states, these forbidden transitions cannot be accessed by the nuclear spins. However, the state mixing produced by the hyperfine interaction, discussed in section 2.3.1, gives the transitions a small probability which is proportional to the amount of mixing. At cryogenic temperatures, the electronic polarisation tends to unity[10]. As this happens, the effect of the $B_\pm$ hyperfine coefficient on the nuclear spin ensemble increases and the state mixing increases. It follows intuitively that to maximise the transfer of spins through the forbidden transitions, then the system should be driven by an oscillating magnetic field with energy equal to the difference between

---

[10]Assuming a B_O field strength of at least 3 T

two states. This leads to the SE resonance condition:

$$\omega_{\mathrm{mw}} = \omega_{\mathrm{S}} \pm \omega_{\mathrm{I}}. \tag{2.31}$$

At these frequencies one of the ZQ or DQ transitions is satisfied. This attempts to equalise the populations of the energy levels involved, by flipping both spins. However, as the electronic spin relaxation is significantly faster than the equivalent nuclear relaxation, the electron quickly returns to its equilibrium state leaving the nucleus deposited in the opposite spin state to that it started in. For example, when the DQT is driven with microwave irradiation, a transfer of population betweeen the states $|\beta\beta\rangle$ and $|\alpha\alpha\rangle$ is driven. Electronic relaxation takes the system down to the $|\beta\alpha\rangle$ state, effectively transferring the nuclear spin from $|\beta\rangle$ to $|\alpha\rangle$. The nuclear spin relaxation will constantly drive the system back to thermal equilibrium, but if the microwave irradiation transfers spin polarisation faster than it can decay, then the nuclear polarisation will build up over time.

For the SE picture to be valid an important characteristic of the system is that the line width of the radical EPR line is narrower than the nuclear Larmor frequency,

$$\Delta\omega_{\mathrm{S}} < \omega_{\mathrm{I}}. \tag{2.32}$$

If this is not the case then application of microwaves will effectively satisfy both cases of equation 2.31 thus cancelling out the build up of one nuclear spin state. This is observed most clearly during the build-up of proton polarisation while using narrow-line radicals such as Trityl OX63, such systems display *well defined* solid effect characteristics such as microwave sweep profiles with well separated DNP resonances.

2.5.2 The Cross Effect

Another mechanism by which electronic spin polarisation can be transferred onto nuclei is the Cross Effect (CE). This effect is modelled around one nucleus and two weakly coupled electron spins. In free-radical molecules that are inhomogeneously broadened the Larmor frequencies of electron spins are distributed in spin packets across the EPR spectrum. When the distribution of frequencies is larger than the nuclear Larmor frequency then there will be combinations of spin packets that are separated by nuclear Larmor frequency, satisfying the equation

$$|\omega_{S_1} - \omega_{S_2}| = \omega_I. \tag{2.33}$$

The cross effect model is constructed of two dipolar-coupled electron spins that satisfy this equation. The energy level diagram that contains these spins and the nuclear spin will have eight distinct energy states. However, as equation 2.33 is satisfied, the energy states $|\beta\alpha\beta\rangle$ and $|\alpha\beta\alpha\rangle$ are degenerate. This condition means that the forbidden zero and double quantum transitions between the nucleus and one of the electrons will coincide with the single quantum transition of the second electron [32]. By applying microwaves at the Larmor frequency of one of the electrons two processes occur: First, there will be a partial equalisation of the populations of energy levels associated with the single quantum transition of that electron; Second, following equation 2.33 the irradiation frequency will also drive a DQ or ZQ transition which will flip the second electron and the nuclear spin. Figure 2.11 shows the distribution of energy states and how the microwave irradiation transfers nuclear spin into the desired state. Analogously to the solid effect, the faster electronic relaxation then allows the spin polarisation to be built up on the nucleus. A mathematical description of the Cross Effect is unnecessary here, however a good introduction can be found here[33].

[34]
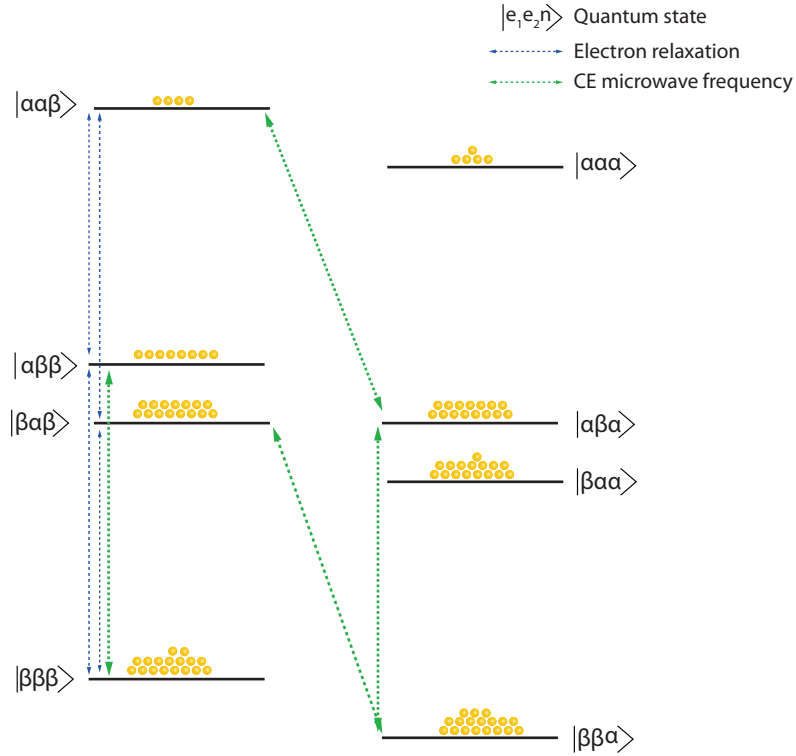
Figure 2.11: The three spin Cross Effect model. This system displays 8 energy levels. By driving the system at one of the electron resonance frequencies DQ or ZQ transitions can be driven, flipping the second electron and nucleus.

2.5.3 Thermal Mixing

Spin Temperature

In thermal equilibrium, the polarisation of spins is described as a function of temperature in the Boltzmann distribution. When the ensemble of spins is taken away from this equilibrium it can still be described by this function, however the temperature is no longer a thermal measure of the lattice. Rather it is an effective *spin temperature* (T_S) [35]. From this concept of spin temperature come a coefficient value that describes the population system in relation to the Boltzmann equation. This *inverse spin temperature* is defined by the equation

$$\beta = \frac{1}{k_B T_S}.$$

(2.34)

Inserting this into equation 2.6 gives

$$P = \frac{N_+ - N_-}{N_+ + N_-} = \tanh\left(-\beta\gamma\hbar B_0\right).$$ (2.35)

This concept of spin temperature allows the consideration of the spin temperature as a function of spin population, examples of these different states are included in figure 2.12.
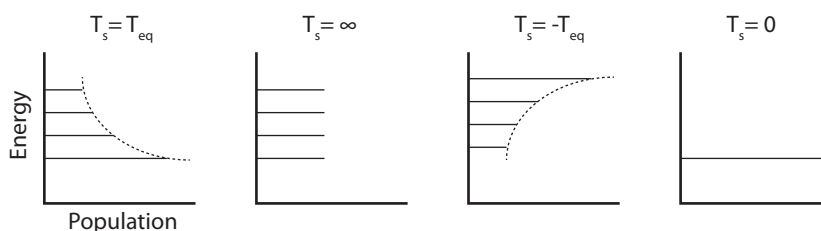
Figure 2.12: Pictorial representation of spin temperature for different population distributions. LEFT: In this graph the spin temperature is maintained at the equilibrium temperature of the surrounding lattice, the population of each energy state is what would normally be expected at thermal equilibrium. LEFT CENTRE: As the spin temperature approaches infinity, all of the spin levels are equally populated. RIGHT CENTRE: For a negative spin temperature, the spin populations are inverted, analogous to the application of a π pulse. RIGHT: At a spin temperature of zero, the spin ensemble is fully polarised, with all of the spins occupying the lowest energy spin state. Adapted from [35].

Thermal mixing DNP

The Thermal Mixing approach to DNP starts by assuming the electron Hamiltonian is constructed of two separate energy 'baths'. They are: the electron Zeeman bath (EZB) which contains all the energy associated with each electron's interaction with the external field; and the electron dipolar bath (EDB) which contains all of the energy terms that arise from dipolar coupling between electrons in the sample.

The scale of the energy associated with each of these reservoirs is different, with
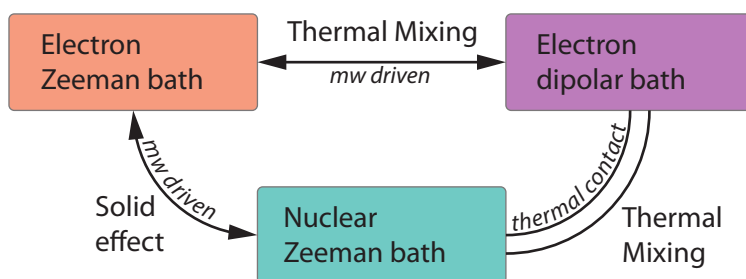
Figure 2.13: The basis of Thermal Mixing DNP lies in the interaction of three thermal baths. In the rotating frame, the application of off-resonant microwaves allows thermal contact between the electron Zeeman and electron dipolar baths. During this contact, thermal energy flows out of of the dipolar bath effectively cooling it. The nuclear Zeeman bath is in thermal contact with the dipolar bath hence it is also cooled during the application of the microwave field.

electron Zeeman energies on the order of 10^{10} Hz and dipolar energies on the order of 10^8 Hz. This means that these baths cannot interact through the exchange of energy quanta [36].

By the application of an off-resonance microwave field, in the rotating frame, an interaction between the EZB and EDB can be established. This allows a flow of energy from one bath to the other. By pumping thermal energy from EDB into the EZB, the EDB can be effectively cooled. The flow of thermal energy raises the temperature of the EZB, however the fast electron relaxation processes drive this temperature back down towards its equilibrium value. From these processes, a new dynamic equilibrium is formed with a EZB temperature that is significantly cooler than that of the surrounding lattice.

Including nuclei into this model allows the description of the TM-DNP mechanism. The nuclei can also be characterised by a Zeeman bath (NZB). This bath is in constant thermal contact with the EDB, hence when the EZB cools, it draws thermal energy out of the NZB cooling it also. The reduction in temperature of the NZB is manifest in an enhanced polarisation of the nuclear spins.

Thermal mixing is a thermodynamic model that uses this concept of spin temperature to explain the interaction and polarisation transfer between many electrons and many nuclear spins [37]. In this model, samples containing homogenously broadened electron spins are split into three separate thermal baths: the electron Zeeman bath, the nuclear Zeeman bath and the electron dipolar bath. The Zeeman baths contain all of the energy associated with the isotropic interactions between the spins and the external field. All of the other interaction energies, including the hyperfine term, are bundled together in the 'non-Zeeman' dipolar bath. The application of slightly off-resonant microwave irradiation saturates the electron spins such that the effective spin temperature of the electron Zeeman bath raises from T_{eq} towards $T = \infty$. To conserve the energy in the system, the energy required to raise the electronic Zeeman energy is drawn from the electronic dipolar bath, lowering its spin temperature. As the electronic dipolar bath is in thermal contact with the nuclear Zeeman bath it, in turn, cools the nuclear spins and increasing the nuclear spin polarisation. While TM has its origins in thermodynamics, Hovav et. al. were successful in using a purely density matrix approach to test the validity of the model without *a priori* knowledge of effective spin temperatures [32].

2.5.4   Microwave power dependence

Both CE and TM show a significant dependence on the applied microwave power [34]. The transfer of polarisation from electron to nucleus requires fast electron T_1 to ensure that individual transfer events happen rapidly, however fast electronic relaxation limits the achievable electronic saturation. To take advantage of fast electronic relaxation, large microwave powers and efficient microwave coupling are required.

3

Instrumentation for Nuclear Magnetic Resonance

It is generally felt by those with experience of superconducting systems that the improvement obtained [at higher field strengths] is disappointing. As it is acknowledged that the electronics needed at very high and ultrahigh frequencies are "difficult", the accusing finger has tended to point in the engineers' direction.

– Hoult & Richards *The signal to noise of the NMR experiment*

3.1 Introduction

As with most spectroscopic disciplines, the efficacy of NMR is entirely dependent on the reliability and precision of the hardware used to make the measurement. The equipment used by NMR spectroscopists has evolved greatly since the first experiments were performed by Bloch, Hansen, and Packard in 1946 [38]. The development of high-precision superconducting magnets and increasingly advanced signal-acquisition electronics has turned a complex experimental set-up into a routine analytical tool.

A complete description of the hardware that constitutes a NMR system is beyond the scope of this document. A highly enlightening introduction to such systems can be found in Fukushima's classic text *Experimental Pulsed NMR: A nuts and bolts approach* [39].

This chapter looks to introduce some of the practical aspects of NMR that are relevant to the project. It starts by looking at the NMR magnet and discusses some methods that are used to ensure the magnetic field felt by the nuclear spins is as homogeneous as possible. Following this, the NMR probe is introduced with discussion of NMR coils and resonant circuits. Finally some of the components that constitute the NMR console, the control units of the spectrometer, are presented.

3.2 The NMR Magnet

As the name suggests, magnets play a crucial role in NMR experiments. One of the main reasons that the technique has become such an important spectroscopic tool is development of stable superconducting magnets with field strengths of up to 27 T (providing a proton Larmor frequency of 1.2 GHz). Following the concepts presented in the previous chapter, the increase in field strength proportionally increases both the resolution and spin polarisation of a NMR experiment. Yet, however sophisticated these magnets become they remain subtly imperfect. Engineering limitations mean that the field produced by the large superconducting magnet can never be absolutely homogeneous across the whole sample. Methods have been devised that seek to negate the imperfections of the magnetic field, such methods are collectively known as *shimming* the magnet.

3.2.1 Shimming the magnet

In the early days of NMR, the distortions of the large field were remedied by placing iron wedges, or *shims*, in positions around the magnet. Such metal shims would distort the field in a moderately predictable way. By placing them in locations

around the magnet such that their field distortions were approximately opposed to those of the magnet, the distortions would cancel out and the static field would become more homogeneous. This technique has long been replaced by the inclusion of additional coils within the magnet that can make their own fields to correct for any discrepancies of the main field.

With similar logic to that of the Fourier transform, any vector field can be created through an infinite sum of spherically harmonic fields of increasing frequency. This means that any field deviations can be mathematically described by a sequence of the form

$$B_0^{real} = B_0^{(0)} + B_0^{(1)}(x, y, z) + B_0^{(2)}(x^2, y^2, z^2, ...) + ... + B_0^{(n)}(z^n, ...). \quad (3.1)$$

This zeroth order term ($B_0^{(0)}$) is not a function of position and gives the ideal, homogeneous field that, ideally, NMR would be performed at. The higher order terms show contributions to the field that do have a positional dependence and which need to corrected using the shim coils. Practically, it would be impossible to perfectly deconvolute all such frequencies and correct for them all. It is, however, possible to correct for the first few orders of such a series through a set of shim coils that can individually create fields for each harmonic. Such shim systems can have components along z axis with orders from z^0 up to z^5 and 'off axis' components such as x and x^2, y and y^2, xy, $(x-y)^2$ and further combinations of x, y and z. There are two sets of shim coils used in modern NMR systems.

Cryoshims

Cryoshims are superconducting coils that are placed in the liquid helium Dewar along with the main coil. They are energised in the same way as the main coil and are set up during the magnet installation. The cryoshims should get the field at the sample to around 5 ppm [40], but they cannot be changed by the operators of the

NMR system during use.

Active shims

In the bore of the magnet, another set of shim coils allow a more precise control over the field. These coils are electromagnets and as such do not need to be placed within the liquid helium Dewar of the magnet. The field produced by these coils can be precisely controlled by varying the current that flows through the coil windings. These shims are designed to fine tune the magnetic field so that it reaches a homogeneity on the order of less than 1 Hz for ^{1}H signals at most experimental field strengths.

There are a number of ways of determining the currents necessary to correct the field. In imaging systems, or NMR probes that contain gradients, it is possible to map the field. The spatial variation of field strengths can then be collated into a 3D *shim map*. Once this information has been found it is possible to calculate the components of a field that would nullify the variation. When shim maps cannot be determined, through lack of gradients or lack of signal, an iterative method is required. This approach tests the NMR signal for of a certain set of shim current values and then changes them. By determining whether or not the change has improved the situation and then repeating the process again, the ideal shim currents can be found iteratively. For relatively coarse shims, this process could be performed by the user. However for determination of an optimum set of many shims it is not practical. NMR systems come with algorithms that can iteratively test shim values much more rigorously than can be achieved manually.

One such algorithm that is used extensively in Bruker systems is the *simplex algorithm*. The simplex algorithm is a topological search program that defines a multidimensional shape (the simplex) which travels across the topology until it lands on the optimum value. The surface is defined by a *quality parameter* which is a measured at the vertices of the shape. There are always $n + 1$ vertices for the simplex shape where n is the dimensionality of the topology. Therefore there are $n + 1$
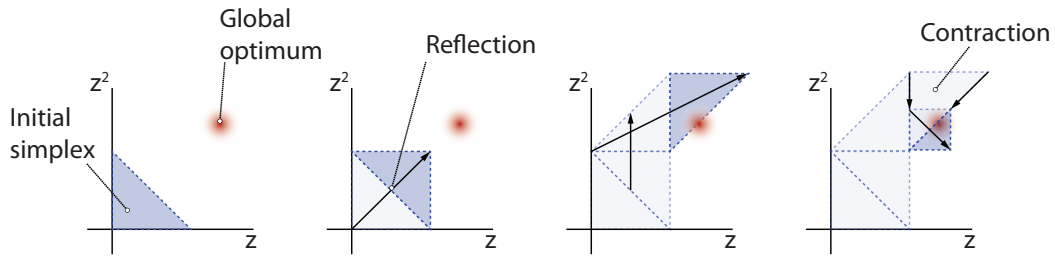
Figure 3.1: Example of the progression of the simplex algorithm: LEFT: The initial simplex shape is set up by testing the quality parameter at points along the shim dimensions. Some global optimum will be present on the topological shim-space. CENTRE LEFT & RIGHT: The simplex shape can move across the shim-space through reflecting the worst point through the shape. RIGHT: When the optimum is inside the simplex shape, it can contract and start moving again closer to the optimum.

quality parameters that indicated the accuracy of the shim currents. For example, if there are two parameters that need to be optimised [1] then the simplex would take the form of a triangle with three vertices. The algorithm then decides how the shape should move across the surface to progress closer to the optimum value. A comprehensive account of the individual steps involved in the progression of the simplex algorithm can be found in [41].

3.3 The NMR probe

Once the nuclear spin ensemble are placed in the static magnetic field, the different spins states become non-degenerate and the ensemble develops a macroscopic spin polarisation. However, NMR data cannot be acquired without a means of perturbing the spin system and observing the resultant dynamics. To achieve this, NMR probes have been developed that can produce oscillating magnetic fields orthogonal to the static field. These additional fields need to be extremely precise in strength, duration and frequency in order to affect the nuclear spins in a reliable and repeatable manner. The probe also serves to acquire the signal arising from the spin ensemble. After the perturbation an oscillating e.m.f is induced in the coil

---

[1] For shimming this could be, for instance, z and z^2 shims

by the time dependent modulation of the sample magnetisation.

Modern NMR systems operate in the radio frequency (RF) regime. High resolution NMR magnets have magnetic fields between 1 T and 20 T, resulting in proton procession frequencies between 42 MHz and 800 MHz.

3.3.1 NMR Coils

The purpose of the NMR coil is to produce an oscillating magnetic field that is orthogonal to the applied static field. The magnetic field is described by the Biot-Savart law [42]. This states that the current I in a small length of the wire dl contributes a fraction dB to the magnetic field

$$\overrightarrow{dB} = \frac{\mu_0 I}{4\pi} \frac{\overrightarrow{dl} \times \vec{r}}{r^3},$$
(3.2)

at a point in space located by the vector $\vec{r}$. Here μ_0 is the permeability of free space[2]. The total field produced by the wire can be found by integrating equation 3.2 across the whole length of wire

$$B(r) = \int \frac{\mu_0 I}{4\pi} \frac{\overrightarrow{dl} \times \vec{r}}{r^3}.$$
(3.3)

For a straight wire, the field produced by the flow of current rotates around the central axis of the wire. It satisfies the 'right hand grip rule' and is a simple case of the Biot-Savart Law.

Equations 3.2 and 3.3 show that the geometry of the coil is crucial for determining the produced field. There are a number of standard geometries for the coils used in NMR and MRI equipment. These include solenoids and birdcage coils. However the probes used in this project all make use of saddle coils.
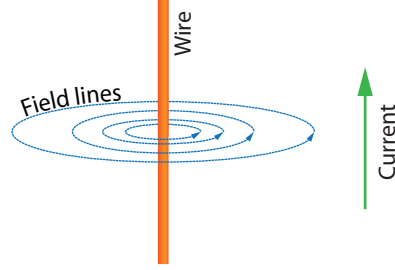
Figure 3.2: The field produced by a straight wire rotates around following the 'right hand grip rule'. This is a simple example of the Biot-Savart law.

Saddle coils

Saddle coils are abundantly used in NMR probe design. They produce relatively homogeneous B_1 fields with a minimum of manufacturing difficulties. The field is produced by four wires, the current flows up through two of the wires and down through the other two. In a saddle coil, the fields produced by the opposing wires interfere to produce a linear field across the sample. By orienting the coil such that the wires are parallel to the static magnetic field, the field produced by the coil will be orthogonal to the static field. The geometry of a saddle coil is shown in figure 3.3, in this situation the homogeneity of the induced magnetic field is dependent on the angle between the wires producing the opposing fields,

3.3.2 Coil sensitivity

For the experiment to work, the NMR coil must be sensitive enough to detect the tiny magnetic fields arising from the spin ensemble in the sample. There are a number of parameters which determine the coil sensitivity. The sensitivity of the coil can be found by considering the signal to noise produced following a 90° pulse. An equation for this signal-to-noise level (Ψ_{rms}) of the observed time-domain signal is by Hoult and Richards in [43]

$$\Psi_{\mathrm{rms}} \approx \eta \, M_0 \left(\frac{\mu_0 \, Q \, \omega_0 \, V_e}{4 \, F \, k_B \, T_c \, \Delta f} \right)^{1/2}. \tag{3.4}$$

---

[2]$\mu_0 = 1.2566 \times 10^{-6} \, \mathrm{m \, kg \, s^{-2} \, A^{-2}}$

Saddle Coil:

⊙ Current flowing out of page   ⋯ Clockwise magnetic field
⊗ Current flowing in to page   ⋯ Anti-clockwise magnetic field
● Sample   ⋯ B_1 field

$\theta = 120°$
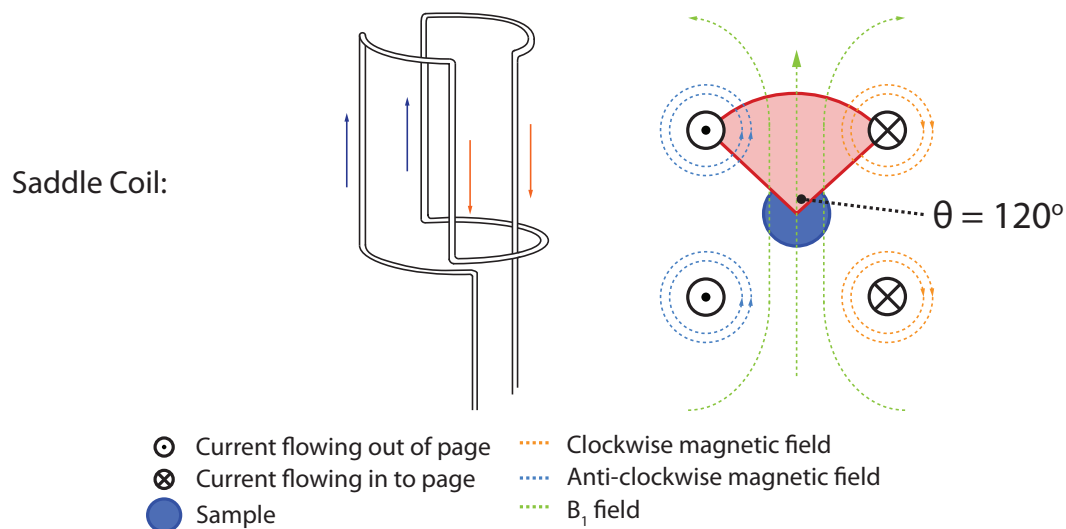
Figure 3.3: LEFT: Geometry of a single-turn saddle coil. The winding of wire allows for two neighbouring wires to flow the current up and two others to flow current down. RIGHT: An illustration of the observed field produced by each strut of the coil and how the up and down current flows produces a magnetic field with a net direction orthogonal to the central axis of the sample tube.

Here η, Q, V_c and T_c are the filling factor, quality factor, volume and temperature of the coil respectively. M_0 and ω_0 are the magnetisation and resonant frequency of the nuclear spins. F is the noise level of the pre-amplifier and Δf is the bandwidth of the receiver.

The obvious purpose of DNP in this case is to increase M_0, however it is important to understand that the increase in NMR signal granted by DNP will not realised unless the other parameters of equation 3.4 are considered.

Filling factor and coil volume

The filling factor of an NMR coil is most basically a ratio between the total volume inside the coil and the fraction of that space that contains the sample of interest. More explicitly it is the ratio between the magnetic energy in the sample and the total magnetic energy produced by the coil [44]. Equation 3.4 indicates that while

the sensitivity of the coil scales linearly with the filling factor, it only scales with the square root of the coil volume. This indicates that it is more important to ensure that the sample of interest fills the coil volume rather than increasing the size of the coil. This is one of the main concepts driving the design of NMR systems using micro-coils, as coils get smaller they closer fit the sample.

Coil temperature and pre-amplifier noise

The sensitivity of the coil provides a measure of the smallest possible signals that can be adequately observed. It is important, therefore, to understand the sources of noise in the coil. The electrons inside the metal of the coil are agitated by thermal contact with the lattice. This inherent random motion of the electron within the coil material gives rise to *Johnson noise*[45]. This is true of all the spectrometer electronics regardless of the current or voltage applied across the conductor. To control the noise within these first two stages of signal acquisition, significant effort has been put into the development of cryogenically cooled NMR probes. These cryoprobes house RF coil, the resonant circuitry and also a signal pre-amplifier. All of these components are cooled with either a flow of liquid helium or nitrogen [46]. Commercial cryoprobes are advertised that routinely increase coil sensitivity by a factor of 5.

Quality factor

A perfect lossless resonator would oscillate indefinitely at its characteristic frequency. Once the energy had been placed into such a resonator there are no mechanisms through which the energy can dissipate. This situation is not practically possible, or indeed desirable. Real world resonators, such as NMR coils, will always lose energy through a variety of means. This loss of energy results in a decay, or *ring-down*, of the oscillation when it is not being driven. For the same reasons outline for FIDs in the previous section, this energy loss results in a broadening of the frequency resonance of the coil. The quality factor (or Q-factor) is a measure of the power losses of the coil and can be described mathematically as

$$Q = \frac{\omega_r}{\Delta\omega}, \tag{3.5}$$

where ω_r is the resonant frequency of the coil and $\Delta\omega$ is the FWHM of the coil resonance.

3.3.3 Resonant Circuits

When passing an oscillating signal through a circuit, it will encounter a complex and frequency-dependent version of resistance called impedance. This impedance is a function of all the individual components that make up the circuit.

The impedance of a circuit which contains an NMR coil can be tailored to the needs of the experiment by incorporating the coil into a *resonant circuit*. The impedances of all of the components that make up the circuit will combine to give the circuit its characteristic resonant frequency. Using simple, passive, electronic components it is possible to control the impedance of a circuit such that it preferentially conveys signals that are made up of a specific narrow range of frequencies e.g. while observing a certain spin species during an NMR experiment.
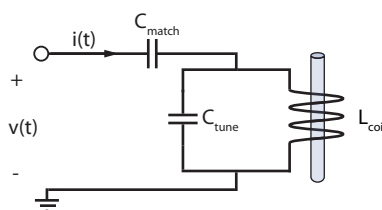
Figure 3.4: Circuit diagram of a LC resonator circuit. The resonant frequency of the circuit is a function of square root of both the total inductance and the total capacitance of the coil. To tune the circuit a combination of capacitors and inductors are used. In practice all elements of the circuit will have some sort of capacitance and inductance.

The simplest type of resonant circuit is shown in figure 3.4. This LC-circuit contains an inductor, with inductance L_{coil}, and a capacitor, with capacitance C_{tune}. The time dependent characteristics of these passive electronic components are often

combined to perform frequency specific signal processing tasks such as filtering signals. When they are placed in parallel along a signal path they act as a tuning circuit which develops a resonant frequency calculated with the equation

$$\omega = \frac{1}{\sqrt{L_{coil}C_{tune}}}.$$ (3.6)

For saddle coils used in NMR probes the inductances tend to be of order of 10^{-9} H. This means that to achieve resonant frequencies in the tens to hundreds of MHz capacitors must be used that have a capacitance in the order of 10^{-12} F.

Coils may be locally or remotely tuned. Locally tuned circuits contain the full circuit from figure 3.4. This is the most straightforward way of designing a robust resonant circuit. There are situations that do no allow for the circuitry to be included with the NMR probe. In such cases it is possible to remote tune the coil through the use of transmission lines. If set up correctly, this can be nearly as effective as local tuning [47] but requires much more rigorous design with considerations of transmission line theory and effective grounding. All of the coils used in this project were locally tuned.

Once the requisite frequency has been produced, the circuit then needs to be matched to the impedance of the rest of the electronics in the spectrometer. Any impedance mismatches observed by the flow of current will act as a potential barrier and will reflect some of the power back to the source. To minimise this reflectance, all sections of the NMR path should have the similar impedance values at the requisite frequencies. By convention, the electronics of the NMR spectrometer[3] have an impedance of 50 Ω. So for all of the observed signal to be efficiently transferred by the receiver, the resonant circuit also needs to have a characteristic impedance of 50 Ω at the desired frequency. The matching of a resonant circuit is easily controlled by the inclusion of a second capacitor in series with the LC-circuit.

---

[3] and most other electronics that look at oscillating signals
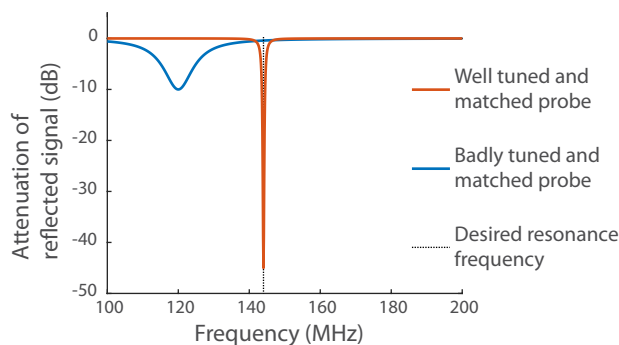
Figure 3.5: Illustration of good and bad tuning response from LC circuit. The resonance of the circuit will take the form of a Lorentzian curve with the resonant frequency at its centre. The width of the resonance gives a measure of the decay of any oscillating signals that are put into the circuit, this is known as its characteristic ringdown time.

Figure 3.5 shows an example of both a well tuned and badly tuned resonator. In this example the desired frequency is 144 MHz. The blue trace is both badly tuned and matched. Here, the attenuation of the reflected power ($P_{\text{reflected}}/P_{\text{transmitted}}$) is only 10 dB[4]. This is compared to a resonator that is well tuned and matched in orange. In this case the reflected signal is significantly smaller than the initial signal with an attenuation of over 40 dB. For high-resolution NMR probes it is normal of this attenuation to be below at least 30 dB.

3.3.4 Coil Cross talk

If multiple coils are placed close together then there is a possibility that the magnetic fields produced by one of the coils will couple into the second coil, inducing unwanted currents. This can be especially a problem for NMR systems where the pre-amplifier and amplifier stages are designed to detect the small NMR signals. With even weak coupling between coils, the induced current could be orders of magnitude bigger than the tiny e.m.f arising from the precessing sample magnetisation.

---

[4]If this signal was a 10 W NMR pulse then around 1 W of the power would be reflected by the probe.

There are a few ways of reducing coil cross talk in practical systems. If the coils are tuned to different frequencies, as they tend to be in multi-nuclear liquid state probes, then the impedance of the coils at off resonance frequencies will be high enough to restrict induced currents. For coils that are tuned to the same frequency (as will be discussed in chapter 7) the coils need to be separated in space and RF shielding is required to minimise mutual coupling between them.

RF shielding is usually made of conductive materials. When a magnetic field encounters the surface of the shielding it induces an electric current in the conductor. If the RF shield is sufficiently grounded then no static charge can build up on the shield. In this way, the RF shield acts as a Faraday cage between the coils, massively reducing the cross talk between the coils [48].

3.4   Microwave Frequency Hardware

As was introduced in the previous chapter, DNP requires the manipulation of electronic spins via microwave frequency irradiation. The quasi-optical microwave system used in this project was not developed during the course of the project. An introduction to the quasi-optics used can be found in [49, 50, 51] and, specific details of the DNP spectrometer in Nottingham can be found in [52].

At 3.35 T, W-band in EPR, solid-state microwave sources can provide stable and highly controllable microwaves. Sources, such as the one used in this project are based around a Yttrium-Iron garnet (YIG). In this device, electrons inside a single YIG crystal resonate in the presence of an externally applied static magnetic field. The resultant electromagnetic output of the crystal is at microwave frequencies of up to 15 GHz. As the frequency of oscillation is dependent on the strength of the externally applied field, by using an electromagnet to create the static field, simply changing the DC voltage changes the output microwave frequency. A lock-in-amplifier can then be used to maintain a consistent frequency output from the

source.

3.4.1   Microwave wave-guides

EPR and DNP systems employ wave-guides to transmit the microwaves from the source to the sample. There are two distinct ways of accomplishing this transmission. Firstly, hollow wave-guides can be used to confine microwave fields such that standing waves of the electric or magnetic fields are formed along the transmission path. Such standing waves can be formed by passing the microwaves through an internally corrugated pipe. These corrugations reduce the insertion loss of the wave-guide. When the geometry of the wave-guide is correct and the desired modes are observed, there is near lossless transmission of microwave power [53].

Microwaves can also be transmitted through space in the form of a Gaussian beam. In this form, the microwaves can be treated *quasi-optically* with components equivalent to lenses, mirrors and polarisers used in conventional optics. At higher microwave frequencies, delivering microwaves quasi-optically is more efficient than conventional wave-guides [54]. Even at lower microwave frequencies, transmitting microwaves through space is useful in systems in which the microwave source cannot be mechanically coupled to the microwave destination via a wave-guide. The development of quasi-optic microwaves is linked to increasingly efficient 'mode converters' which can translate between the waves observed in wave-guides with the Gaussian beam and *vice versa*, these devices are known as feed horns. A comprehensive introduction to feed horns, such as the ones used in this project, is provided by Cruickshank and co-workers [50].

3.5   The NMR console

The console is the unit that controls the operation of all the other hardware involved in the experimental process. The console has two main responsibilities, to transmit (Tx) and then acquire (Rx) signals. Firstly, it generates arbitrary waveforms with an

accurate carrier frequency, then it amplifies them to the required power level and then sends them to the resonant probe. After this, electronic gating changes the signal path toward a receiver unit involving pre-amplifier, amplifier and analogue-to-digital converter (ADC). The digitised signal can then be recorded to the computer memory. Many spectrometer consoles have two sets of transmit/receive pathways. This allows two nuclear spin species to be observed independently, or for a single nucleus to be observed while it is being decoupled from another spin (usually ^{1}H).
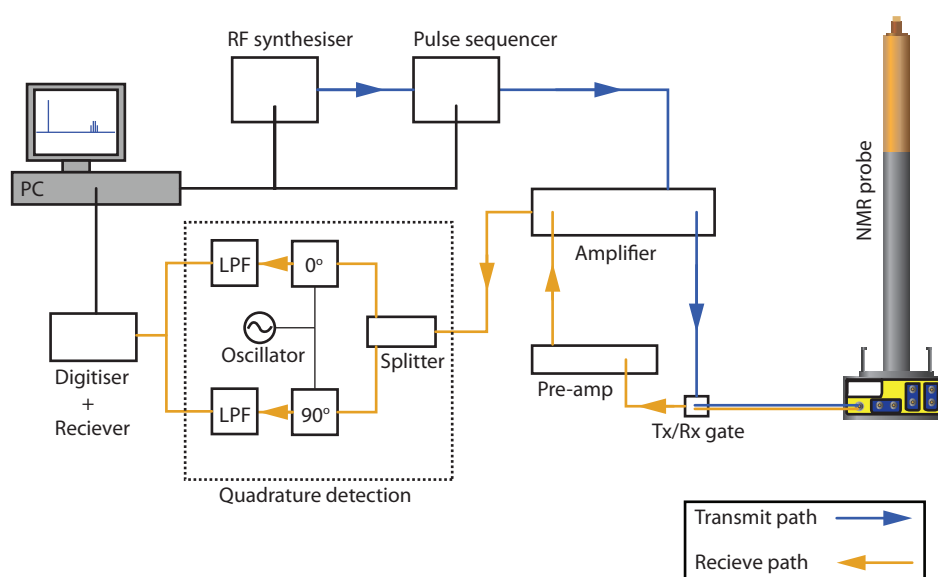
Figure 3.6: A basic flow diagram of the NMR console. An RF synthesiser creates oscillations at the required frequencies. These oscillations are then gated into pulses before amplification and transmission into the NMR probe. The e.m.f induced on NMR coil by the precessing magnetisation is then sent to the pre-amplifier stage prior to further amplification by the high power amplifier. The resultant signal is split into two parts for quadrature processing low-pass filtering before it is digitised in the ADC and the information sent to the NMR workstation

Carrier frequency

The precession frequencies of nuclear spins are in the MHz regime for most experimental field strengths. The chemical shift caused by a spin's magnetic environment only changes these frequencies on the order of parts per million (ppm) of the base

frequency. It is therefore unnecessary to analyse these high frequencies directly. It is much more efficient to look at a small range of frequencies around a pre-set *carrier frequency*. To down-convert the frequencies to a more manageable level, the acquired signals are multiplied by a cosine function which oscillates at the carrier frequency ω_C [55].

$$\cos(\omega_{rx}t) \cdot \cos(\omega_C t) = \frac{1}{2}\left[\cos(\omega_{rx} + \omega_C t) + \cos(\omega_{rx} - \omega_C t)\right] \qquad (3.7)$$

The resultant signal contains two sets of frequencies that are separated by $2\omega_C$. It is then just a case of filtering out the higher frequency components.

Quadrature Detection

If the receiver is calibrated such that it has the same phase as the transmitter, then the observed cosine wave produced by equation 3.7 is equivalent to the x-component of the magnetisation. By the same logic it is also possible to extract another set of points that are 90° out of phase with the first simply by multiplying the incoming signal with a negative sine oscillation rather than a cosine. This means that if the first set of points are the x-component of the magnetisation, then by shifting the receiver phase it is also possible to obtain the y-component. Mathematically this takes the form

$$\cos(\omega_{rx}t) \cdot -\sin(\omega_C t) = \frac{1}{2}\left[-\sin(\omega_{rx} + \omega_C t) + \sin(\omega_{rx} - \omega_C t)\right]. \qquad (3.8)$$

By acquiring both the x and y-components of the FID it is possible to arbitrarily phase the resultant spectrum.

Analog-to-digital converter

The detected voltage is subsequently converted to digital information for storage and analysis on the spectrometer computer. This is performed by the analog-to-digital converter (ADC). There are two important parameters that the spectrometer uses for data collection. The *dwell time* is the time between digitised points, in
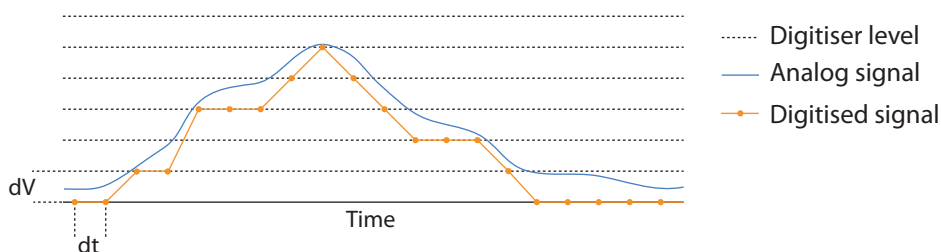
Figure 3.7: Function of analog-to-digital converter. The observed analogue signal has a continuous range of possible amplitudes. The digitised signal is then a record of the total number of digitiser levels that fill up to, but do not exceed, the analogue voltage level. This measurement is made at set increments separated by the dwell time dt

figure 3.7 the dwell time is shown as dt. The inverse of the dwell time corresponds to the spectral width of the spectrum that can be recorded. The digitiser resolution is also important to determine the accuracy of the conversion of e.m.f to digital information. A digitiser overflow can occur when the largest observed signal is above the top digital level. In this case, the top digital level is recorded and the rest of the signal is wasted. It is important for dissolution DNP experiments to have a correctly calibrated ADC resolution as overflows will reduce the observed, enhanced signal.

Decoupling schemes

Proton decoupling is a standard procedure for NMR spectroscopists. By manipulating the proton spins during detection of other nuclei, it is possible to average out the effect of the ^{1}H-X J-couplings and make multiplet peaks collapse into single resonances. Such single resonances are found with increased signal-to-noise as the integrals of all the multiplet peaks are summed together. For complex samples, the removal of numerous multiplet peaks also allows for better nuclear assignment.

The most basic way to do this is to apply c.w. irradiation to the protons perpendicular to the static magnetic field. The proton magnetisation precesses around this B field. Of course, the bandwidth of c.w. irradiation is very small and effec-

tive broad-band proton decoupling is not possible [56]. This can be emulated with pulsed decoupling of the form of a train of 180° pulses. This process can successfully decouple the protons in the system, however imperfections in the 180° pulses will build up over time, rendering the decoupling scheme ineffective

Composite-pulse decoupling (CPD) is standard for modern proton decoupling. Instead of applying 180° pulses, a set of pulses of varying nutation angles are applied that direct the magnetisation to the poles of the Bloch sphere, along the B_0 field. By applying pulses along both x and y it is possible to cancel out the majority of imperfections of the full 180° pulse [57]. The WALTZ CPD sequence involves making 'blocks' of pulses and then repeating them a number of times, for example a WALTZ-4 sequence is made of 4 blocks 'W', where W is defined as:

$$W = 90_x 180_y 270_x, \tag{3.9}$$

$$W^\dagger = 90_y 180_x 270_y. \tag{3.10}$$

This block is then repeated four times:

$$WWW^\dagger W^\dagger, \tag{3.11}$$

Sequences such as the WALTZ-4 can be extended to include more blocks, by increasing the total number of blocks of opposite phase, the inaccuracies of each pulse are minimised further. The effective bandwidth of the decoupling pulse is one of the driving factors for the development of new decoupling schemes. This bandwidth shows how much of the nuclear spectrum will be adequately decoupled. For the simple molecules used in this project, the requisite bandwidth was achieved through long, low powered pulses following the WALTZ scheme described above. However for more complicated molecules such as large proteins, more advanced decoupling mechanisms need to be employed.

4

Hardware approaches to Dynamic Nuclear Polarisation

It doesn't matter how beautiful your theory is, it doesn't matter how smart you are. If it doesn't agree with experiment, it's wrong.

– Richard P. Feynman

4.1 Introduction

All nuclear hyperpolarisation methods are hardware intensive. So much so that no current hardware set up solves all of the issues of producing highly polarised samples. Presented here is a general introduction to hardware solutions for DNP and, more specifically, dissolution-DNP experiments. The developments introduced here generally fit into three brackets:

- First, various polarisation schemes are introduced and discussed, these methods attempt to produce bigger polarisation levels in shorter times.

- The development of heating and sample shuttling strategies looks to deliver the hyperpolarised sample as quickly and as reliably as possible.

- The implementation of strategies to maximise the amount of data acquired from the hyperpolarised liquid.

4.2   Solid-state polarisation strategies

The first problem encountered in DNP systems is how to maximise the nuclear polarisation prior to dissolution. Most systems, such as the one used in this project, us a CW microwave source to satisfy one or more of the DNP mechanisms described in chapter 2. Most of these polarisation systems perform at temperatures of between 1 and 2 K at a field strength of 3.35 T [58, 59]. Optimised polarisers have reported polarisation levels of up to $P(^{13}C)$=50% in the direct polarisation of carbon [60], this is achieved with sample temperatures of 0.8 K. The efficiency of both solid effect and cross effect scale inversely with magnetic field strength (SE $\propto 1/B_0^2$ and CE $\propto 1/B_0$), however this has not stopped work into increasing the field strength used for polarisation. The lower efficiency means that nuclear polarisation build-up times increase, but the increased electronic polarisation allows the saturation polarisation level to be increased. Bornet and Jannin report a modular polarisation system that can be placed inside either a 3.35 T or 6.7 T wide-bore magnet [61]. Polarisation measurements taken at 1.2 K in both field strengths show that the higher field produces polarisation levels 3.6 times higher than at the lower field but with an 8.8 times longer build-up time. Similar results are presented at 2.5, 4.5 and 5 T [62]. In these tests a maximum polarisation of $P(^{13}C)$=75% was observed on a $[1-^{13}C]$ Pyruvic acid sample in the 5 T field and at 900 mK. This polarisation level was reached with a build up time of around 90 minutes, prohibitively long for reasonable experimental design, however they also report that after only 30 minutes, the polarisation level was 1.6 times that obtained at 3.5 T. The evolution of commercial DNP systems has also seen an increase in magnetic field strength. The first such system the *HyperSense* produced by Oxford instruments. It was based on the original polariser at 3.35 T designed by Ardenkjær-Larsen an co-workers [4]. The more modern *SPINlab* system made by GE Healthcare (Chicago,

IL, USA) uses a magnetic field of 5 T.

4.2.1 Controlling electronic relaxation

It is possible to speed up DNP build up be decreasing electron relaxation time. To achieve this, chelates, such as Gd^{3+} or Mn^{2+} can be used to dramatically increase paramagnetic relaxation of the electron spins [63, 64]. Lumata and co-workers reported that ^{13}C polarisation with Trityl OX63 can be increased by up to 3 times with millimolar concentrations of a Gadolinium dopant [65].

4.2.2 Cross polarisation

The methods outlined above have all assumed a direct electron-to-carbon polarisation process and use Trityl OX63. Inhomogeneously broadened radicals, such as the nitroxide radical TEMPO, are not efficient at polarising carbon spins. However they do produce high proton polarisations on the order of $P(^1H)$=90% with build up times of a minute or two. Combing this high level of proton polarisation with Hartmann-Hahn cross polarisation between ^1H and ^{13}C spins allows for carbon build up in a significantly reduced time [66, 67, 68]. This process has been used widely in solid state NMR spectroscopy, especially in MAS systems. It has subsequently been transferred into DNP by a number of groups, included the work carried out by Perez Linde here in Nottingham [69]. The CP method requires a doubly tuned coil. First the proton polarisation is quickly allowed to saturate, then a spin-locking pulse sequences that match the Hartmann-Hahn condition $\gamma_I B_{1I} = \gamma_S B_{1S}$ can transfer some of this polarisation to the low-gamma spins, such as carbon. Bornet et $al.$ showed that applying cross polarisation to their DNP system at 1.2 K doubles the carbon polarisation ($P(^{13}C)$=36% $\rightarrow P(^{13}C)$=71%) with a build up time four times shorter ($\tau_{DNP} = 1980 \rightarrow \tau_{CP-DNP} = 488$) [61]. The hardware application of CP is not always straightforward for dissolution systems as it requires doubly tuned coils that are capable of delivering reasonably high RF powers, on the order of 20 kHz and above.

4.2.3 Microwave frequency modulation

In DNP samples containing inhomogeneously broadened radicals the modulation of the microwave frequency can enhance the both the saturation nuclear polarisation and build-up times. This was initially shown by Hovav and co-workers [70] and developed further by Bornet *et al.* [71]. It works on the principle that radicals with large inhomogeneously broadened EPR line shapes are effectively constructed of a set of spin packets. The application of monochromatic microwave irradiation will attempt to saturate a single spin packet at the chosen frequency. Only the electrons that make up this spin packet will therefore contribute to the transfer of polarisations. Further electron spin packets will eventually contribute through electronic spectral diffusion processes. By modulating the frequency of the applied microwaves it is possible to increase the number of electron spin packets incorporated into the DNP process. Initial work has involved a sinusoidal modulation of frequency, this led to an increase in proton enhancement of three times [72]. Guy and co-workers are developing this technique further by using the intensity of the EPR line to control the frequency modulation rate.

4.2.4 Pulsed DNP

More sophisticated microwave systems have the ability to apply pulses to the sample. Such pulsed-DNP experiments aim to satisfy the Hartmann-Hahn condition for cross polarisation directly between the electrons and the nuclear spin of interest. Performing a polarisation transfer in this way is advantages as the process does not scale with the applied static magnetic field, hence there is no negative relationship as the field is increased [73].

At low fields, a different method of satisfying the Hartmann-Hahn condition was developed theoretically by Henstra and Wenckebach [74] and has since been implemented experimentally in the Griffin lab in MIT [75]. This NOVEL method (Nuclear Orientation Via Electron spin Locking) uses the static field to satisfy one

side of the CP condition such that the electronic spin locking pulse must match the intrinsic Larmor frequency of the nuclei ($\omega_{1S} = \omega_{0I}$). Experiments show that this technique can transfer significant polarisation to the nuclei in nanoseconds. In experiments at 0.35 T and at 270 K, proton solid-state enhancements of 165 were observed after a spin-lock mixing time of around 100 ns. At lower temperatures (around 80 K) this enhancement is increased to 430 in the same time scale.

4.2.5   Multi-sample probes

There have been a number of approaches that seek to increase the speed by which a dissolution DNP experiment can be repeated. Batel *et al.* presented a revolver style sample changer in which six samples can be stored prior to polarisation [76]. Pneumatic actuators housed outside the magnet can rotate the six sample cups, stored at low temperature, and load each into a microwave-resonant cavity for polarisation. These samples can then be removed from the cavity prior to dissolution. During the sample dissolution a dissolution stick is inserted into the magnet bore. This means that the cryostat needs to be warmed up to at least 4.2 K with helium gas to produce an overpressure. The authors state that the additional relaxation effects of the remaining samples at this higher temperature can lead to a 14% reduction in overall polarisation.

Another method utilising four independent 'sample sticks' which fit around a metal structure in a standard bore magnet [77]. Again, the structure can allow the rotation of the four samples, however in this set up each stick contains all the required apparatus to perform the dissolution experiment. Each dissolution can be performed independently and within only a few minutes.

4.3 Heating strategies

4.3.1 Temperature Jump DNP

Once the polarisation has been accrued on the nuclear spin, the sample is brought back up to ambient temperature for liquid state experiments. As has been introduced, dissolution-DNP uses heated solvent to interact with the cold sample. However, the rise in temperature can also be achieved by other means. Temperature jump DNP (TJ-DNP) was initially conceived in the lab of Griffin in MIT [78]. Rather than dissolving and shuttling the sample, TJ-DNP uses a heating source such as infrared laser irradiation to melt the sample *in situ*. This process has two distinct advantages over dissolution-DNP: Firstly, the sample is not dissolved during the process, therefore the concentration of the original sample is maintained. Secondly, once NMR acquisition has been performed the sample can be allowed to re-freeze and re-polarisation, allowing signal averaging to be performed. The TJ-system in MIT comprises of a 5 T (140 GHz EPR) magnet and a cryostat capable of temperatures of around 90 K. This system shows proton enhancements (corrected for temperature change) of between 120 and 400, these numbers related to and enhancement of between 400 and 1333 by the calculation used by Ardenkjær-Larsen. The CO_2 infrared laser allows sample melting to take place in less that 1 s. One disadvantage of the TJ-DNP set up is that it is not possible to alter or in any way effect the molecular composition of the sample once it is in the system. This is acceptable for structural studies, however it makes analysis of dynamics or chemical reactions difficult to implement.

4.3.2 Optimising the dissolution process

As the majority of dissolution systems are home-built there is a wide array of performance values in terms of sample shuttling speeds, volume of dissolved samples, dilution factors and so on. Bowen and Ardenkjær-Larsen have explored the efficiency of the dissolution process for a range of sample sizes, solvent temperatures

and driving pressures [79]. By modifying a HyperSense system they were able to consistently get a sample dilution factor of 1:10 for initial sample sizes of up to 10 mg. While this level of dilution is significantly better than most dissolution systems, it remains a slow process with the first NMR acquisition taking place 6 s after dissolution. As with other dissolution systems, the solvent is superheated under high pressure (up to 200°C at 8 bar). This need for superheated solvent reduces the system's ability to observe biological samples as the temperatures involved are likely to de-nature many molecules of interest, such as proteins and enzymes.

Another method for reducing the dilution factor has been developed by Harris and co-workers [80]. During the dissolution, two immiscible solvents are heated and applied to the hyperpolarised sample. By using heated water/toluene mixtures it was possible to fill the NMR tube up in two layers, with the hyperpolarised liquid settling next to the NMR coil. By replacing 3 ml of heated solvent water with 0.5 ml of water and 4 ml of toluene it was possible to achieve quantitative improvements in the NMR spectrum of around 2. While the authors admit that toluene isn't a desirable solvent for biologically relevant samples, they present the idea that solvent that preferentially dissolve individual constituents of the DNP sample i.e. the molecule of interest and radical, it should be possible to remove the radical from the resultant hyperpolarised fluid.

4.3.3 Magnetic tunnels

At low fields, paramagnetic relaxation caused by the free-radical electron spins becomes increasingly efficient. This has been a constant cause of concern for operators of dissolution systems as the flow path between the polarisation magnet and NMR acquisition magnet tends to cross the lab space. To a certain extent the stray field of the magnets help to keep the magnetic field of the flow path at least above the Earth's magnetic field but this is hardly an optimised set-up. Indeed, in situations where the two magnets have opposite polarity, as is reported by Jannin [61], the hyperpolarised fluid may pass through an area of zero field. To counter this,

magnetic tunnels have been devised to enclose the liquid sample in fields of up to 900 mT for the duration of its transit [81]. This is achieved by creating a Halbach array of permanent neodymium-boron magnets with the fluid pneumatically driven through a tube at the centre. This method has allowed proton dissolution signals to be enhanced by up to 25 times.

4.4 Acquisition strategies

4.4.1 Ultrafast 2D spectroscopy

Two dimensional NMR spectroscopy can be used to aid the assignment of complex spectra by providing additional structural information. Normal 2D spectroscopy required a series of excitations in which some evolution time is incremented over successive scans. This process is not possible with hyperpolarised dissolution samples before the additional signal has decayed. Frydmann and co-workers have developed a method for acquiring 2D NMR data in a single scan [82, 83]. To do so they apply a strong z-gradient in conjunction with chirped RF pulses. With this strategy, chemical shifts can be encoded in the spatially modulated magnetisation. This can then be read out to provide 2D information about nuclear correlations that is several orders of magnitude faster than conventional methods. This ultrafast method seems uniquely suited to the single shot nature of dissolution-DNP experiments. The development of HyperSPASM [84] has led to 2D signal enhancements of up to 670 compared to traditionally acquired thermal 2D spectra. However this technique remains limited to small molecules with a limited number of correlations.

4.4.2 Double nucleus polarisation

One way of extracting more information from a single dissolution experiment is to observe more than one nuclear spin species during the course of the experiment. This avenue has seen very little exploration, in fact at time-of-writing there is only a

single paper [85]. In this study, carbon and nitrogen are polarised simultaneously because of their inherently similar DNP sweep profiles. By polarising at the optimum ^{13}C microwave frequency the ^{15}N would then also be polarised with about 60% efficiency.

Samples of Nicotinamide were polarised in this way at cryogenic temperatures and then dissolved prior to liquid state analysis. The spectrometer used during these experiments was only equipped with two independent channels. So by dedicating one of those channels to proton decoupling, the acquisition of both carbon and nitrogen signals was assigned to the same channel. Between the spectrometer and the probe, the channel was duplexed such that it could switch reliably between the two required frequencies. This switching took around 3 s to complete, during which time the enhanced NMR signal was relaxing back to its thermal equilibrium. While the spectra produced did contain peaks for most of the spins present in the system, the delayed acquisition of nitrogen spins allowed a modest liquid state enhancement of 120.

5

Experimental Dynamic Nuclear Polarisation

Experiments were not attempted at that time, we did not believe in the usefulness of the concept anyway, and I finished my thesis in 1962 with a feeling like an artist balancing on a high rope without any interested spectators.

– Richard Ernst

5.1 Introduction

The previous chapter discussed the different approaches to hyperpolarisation. This chapter will describe the equipment that has been set up in Nottingham in order to exploit Dynamic Nuclear Polarisation and, more specifically, our attempts to produce enhanced liquid state samples through dissolution DNP. The system is based around the 'dual core', two superconducting NMR magnets stacked and encased in a single Dewar. By condensing the geometry of the normal dissolution DNP set-up, the time between sample heating and liquid state analysis can be vastly decreased [52].

5.2   The dual iso-centre DNP system

Efficient DNP takes place at cryogenic temperatures, not an ideal environment for studying biologically relevant samples. Hence, to successfully implement DNP enhanced NMR for such samples, an experimental set-up needs to be conceived that can create the necessary environment for each stage of the DNP process. An intermediate stage is also needed to effectively transition the sample between the cryogenic and liquid state positions.

Dissolution DNP uses a heated solvent to rapidly thaw small hyperpolarised samples ready for liquid-state NMR experiments. As discussed in the previous chapter, experimental set-ups based on dissolution-DNP have used two separate NMR magnets. The logical evolution of the dissolution DNP set-up is to combine both the polarising and analysis magnets into one stand alone system. In such a set-up the two sample environments are significantly closer together. Crucially, by producing a straight sample trajectory between stages, it is possible to move the sample mechanically, rather than pneumatically, while it remains in the solid state at cryogenic temperatures. Nuclear T_1 times are significantly longer for molecules in the solid-state, therefore more of polarisation will be retained during the initial stage of sample shuttling.

Figure 5.1 shows the lay out of the dual iso-centre magnetic dissolution spectrometer. The first part of this chapter will introduce the various components in this system. After this, a characterisation of the new dissolution apparatus is presented. Finally the results of the initial dissolution DNP experiments are presented and analysed.

Quasi-Optic bench

Microwave source

Rexolite window

Wave-guide

Stepper-motor controlled sample shuttle

Sliding seal

Air lock

Cryostat Helium inlet

Cryostat

Liquid Nitrogen jacket

Upper iso-centre (3.35 T)

Liquid Helium jacket

Dissolution dock

Lower iso-centre (9.4 T)

approx. 1 m

Liquid-state NMR probe
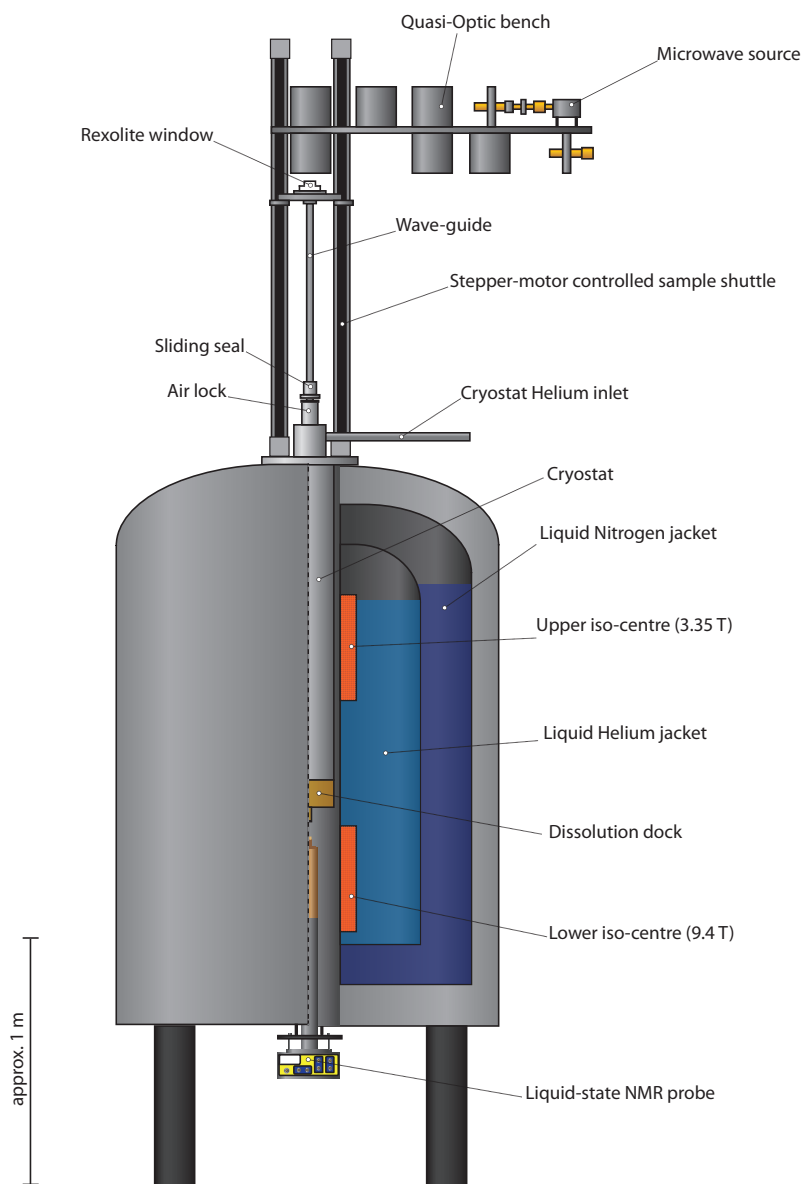
Figure 5.1: Layout of the Dual iso-centre magnet. The 3.35 T magnet is directly above the 9.4 T magnet. The microwaves are directed to the top of the wave guide through a quasi optic system. The rexolite window at the top of the wave guide lets the microwave beam pass into the wave-guide structure. The wave-guide is attached to an actuator which allows rapid vertical movement of the wave guide and sample. At the bottom of the VTI, the sample cup docks with the dissolution system ready for the temperature jump. The resultant hyperpolarised liquid is then injected into a waiting liquid state NMR probe.

5.3 Variable Temperature Insert

To reach near unity electronic polarisation in the upper iso-centre, the sample needs to be held at temperatures below 2 K. The variable temperature insert (VTI - IceOxford - Abingdon, UK) has been designed such that small samples can be brought to temperatures of around 1.6 K for the duration of the polarisation stage of the experiment. To achieve the required temperatures a continuous feed of liquid Helium is drawn from a cryogenic Dewar through a custom-made coaxial transfer-line. This transfer-line uses an evacuated vacuum jacket to reduce thermal input during transfer. The inner tube of the transfer line takes liquid from the bottom of the Helium Dewar to the VTI side arm. From here, the liquid is directed to a liquid Helium reservoir, the 4 K pot. This vessel is designed to store the liquid prior to it being sprayed into the sample space. The 4 K pot also has an outlet which allows warmed liquid and gas to be taken away via the outer tube of the transfer line to a small vacuum pump. Rather than pressurising the Dewar to drive liquid flow, the small vacuum pump creates a small under-pressure in the 4 K pot. This has the effect of sucking liquid Helium through into the VTI. Initial testing suggested that this method of Helium delivery produces a much more stable flow and hence a more stable temperature.

The VTI insulates the sample space with a large volume vacuum space, the Outer Vacuum Chamber (OVC). Prior to performing the experiment, the OVC is pumped with a vacuum turbo pump (Pfeiffer TC-400 - Asslar, Germany). A high-vacuum pressure gauge gives an accurate reading of pressure within the OVC. After pumping on the space for around 15 hours OVC pressures of around $7\text{x}10^{-7}$ mbar are achieved. The leak rate of the OVC is low enough that the pumps can be switched off for the duration of any experiment being performed. Inside the OVC, a thick copper shield (the 50 K shield) further isolates the sample space from external heat sources.

At the bottom of the VTI, a 20 mm thick stainless steel disk fastens to both the outer wall of the cryostat and the inner wall of the sample space. An Indium seal is used to maintain a high vacuum seal of the enclosed OVC. As the VTI cools, the stainless steel body contracts. However, the inner wall of the sample space will contract significantly more than the outer shell of the VTI. An o-ring seal at the top of the cryostat allows the outer wall to move up as the bore contracts.

A stainless steel flange welded to the top of the VTI allows it to sit at the top of the magnet bore, three locator holes allow the VTI to be centred by three stainless steel pins which are screwed into the top of the magnet around the bore. At the bottom of the cryostat, a Delrin spacer fits around the outside of the outer VTI wall. The spacer screws into the dock and then extends 5 cm up through the gap between the bore of the magnet and the outer case of the VTI. Between the locator flange and the Delrin spacer, the position of the cryostat can be maintained.

Two pumping ports at the top of the VTI allow pumping from both the top and bottom of the sample space. These ports allow a KF-25 fitting to be coupled to the high throughput pumping line. Two large in-line pumps provide vacuum to the sample space. The main pump (Pfeiffer DUO 65 M - Asslar, Germany) is used for the entire experiment whereas the second in-line pump (Leybold RUVAC - Cologne, Germany) is only used for further cooling at low temperatures. The lower pumping line is slightly restricted by the 6 mm tube which connects the pumping port at the top of the VTI with the lower sample space outlet. This results in the cold spot of the VTI being approximately 40 mm above the outlet from the 1 K pot. The position of the outer flange allows this cold spot to coincide with the homogeneous region of the upper iso-centre.

Joule-Kelvin Expansion

Liquid Helium sits at around 4.2 K in the Dewar. To get samples down to this temperature is a straightforward process that simply involves placing the sample in a bath of liquid. To achieve temperatures below this value, more complex processes
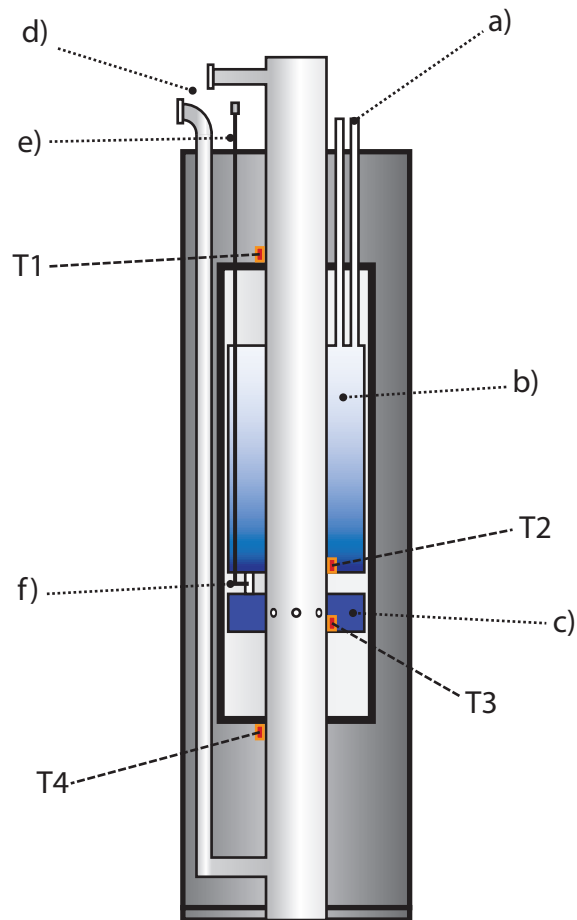
Figure 5.2: Diagram of the Variable Temperature Insert (VTI). a) Liquid helium is delivered through the VTI side-arm. This side-arm has two concentric metal pipes so that it can send in cold liquid from the Dewar through one and warmer helium gas can be removed through the outer pipe. b) The 4 K pot - initial cooling of the system takes this reservoir down to around 4 K, after this point is reached liquid helium will build up here. c) 1 K pot - small area located at the sample space, the coldest liquid helium fills this area before being injected directly onto the sample. d) The central column is open to allow the movement of the sample attached to the wave-guide. The top and bottom of this area are attached to the pumping line to allow low pressure to be applied to the sample. e) Manual control for the needle valve f) which is used to control the flow of liquid helium between the 4 K pot and the 1 K pot.
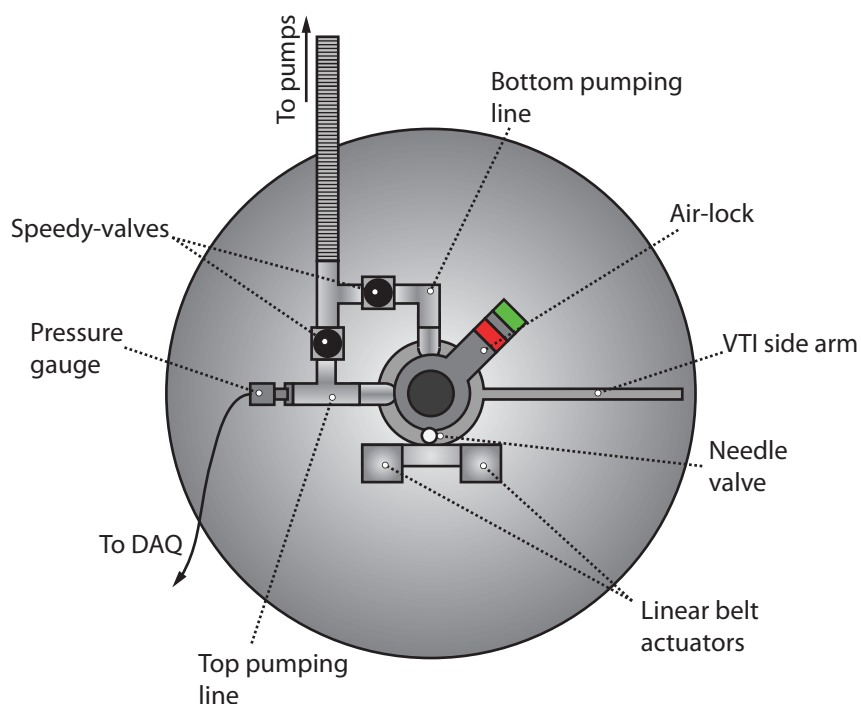
Figure 5.3: Top-down view of VTI pumping lines in the magnet. Both top and bottom pumping ports are connected to the same main pumping line. Two speedy valves allow control over the application of the vacuum pumps to sample space. The pressure gauge allows constant computer monitoring of the pressure in the sample space.

need to be followed. The Joule-Kelvin[1] expansion of gas involves an iso-enthalpic increase in gas volume. At its most basic level, it can be considered as the spreading of thermal kinetic energy of the gas over a larger volume, as the volume increases the average temperature of the gas decreases. This adiabatic throttling of the fluid is only possible when it experiences a sudden and dramatic pressure drop. It can be achieved by forcing the liquid through a narrow valve into an area of reduced pressure. A good introduction to this process is presented here [86] (accessed December 2016). To take advantage of this effect, the fluid needs to be expanded quickly with little external thermal contact.

In the dual core system, a narrow capillary directs liquid from the 4 K pot towards the sample space. The flow through this capillary is controlled by a needle valve

---

[1] Also known as the Joule-Thompson effect

73
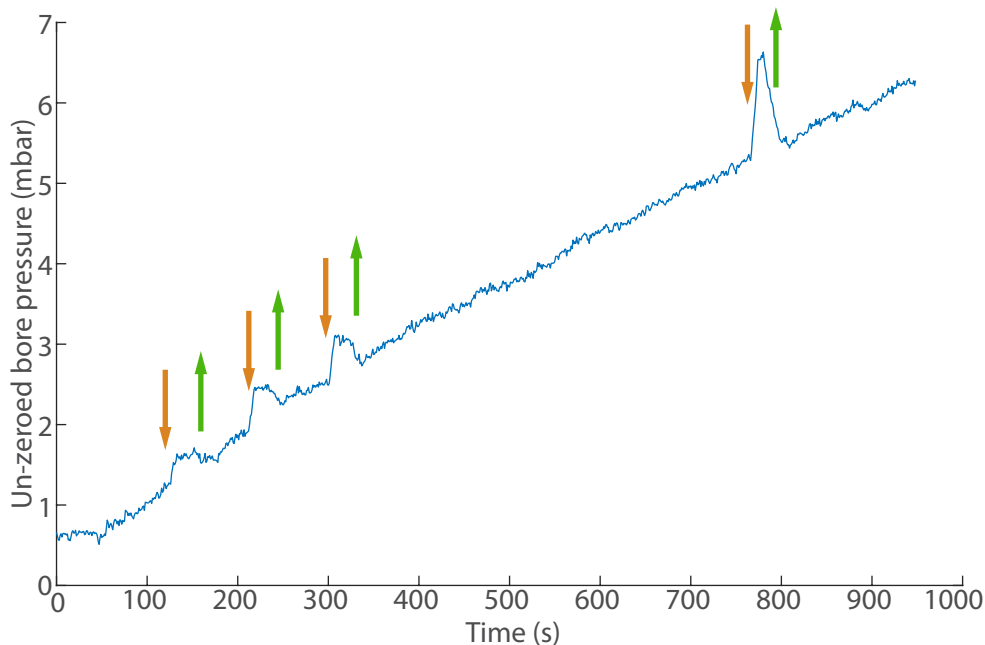
Figure 5.4: Bore pressure over time without pumping. The four bumps indicate times when the wave-guide moves in and then out of the VTI. The orange arrows indicated downward motion into the cryostat, and the green arrows indicate the waveguide rising back to its initial position. After wave-guide motion, the bore pressure returns exactly to where it would have been, this indicates that movement through the sliding seal does not impact on the vacuum of the VTI and that no air should get through into the cold sample space. The leak rate into the sample space is 22.5 mbar hr^{-1}.

which can be controlled from the top of the magnet. At the end of the capillary are a small number of holes through which the liquid can enter the sample space. These holes cause the throttling of fluid flow which is required by the Joule-Kelvin effect. The sample space is held at a low vacuum (on the order of 10^{-4} mbar) by the larger rotary pump outside the lab.

Figure 5.3 shows a top-down view of the VTI inside the magnet. The two pumping ports are both connected to the same pumping line through a set of stainless steel KF-25 T and L pieces. Two KF-25 valves (Edwards Vacuum - Speedivalves - Burgess Hill, UK) allow control of each pumping port independently. The top pumping port is also connected to a pressure gauge which transduces the internal
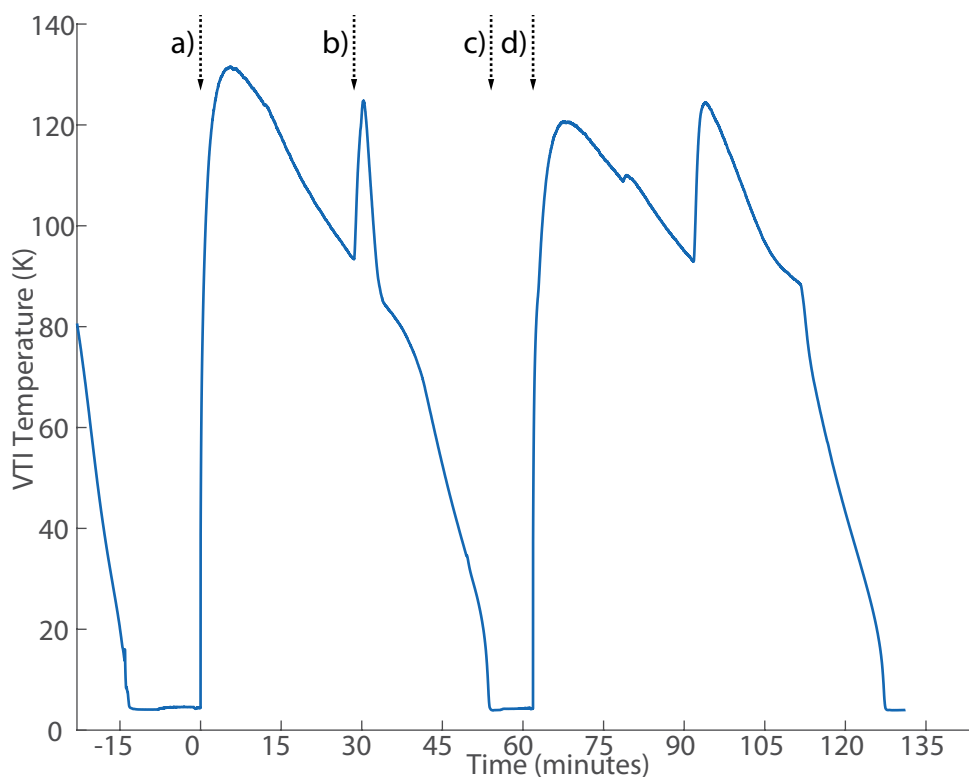
Figure 5.5: Sample temperature before, during and after dissolution. Following a dissolution the system can be returned to its base temperature within one hour. The spikes at around 30 minutes and around 100 minutes are due to the insertion of the next sample to be polarised. This figure does not include the time necessary to build up nuclear polarisation through DNP. Time stamps: a) Dissolution 1 at 0 mins. b) New sample inserted at 27 mins. c) Sample reaches base temperature at 54 mins. d) Second dissolution performed at 63 mins.

pressure of the sample space into a voltage measured by a data acquisition card (NI-DAQ - National Instruments - Austin, TX, USA)

VTI Temperature analysis

There are four carbon ceramic temperature sensors (CCS) embedded at different positions in the VTI to observe temperatures during the cooling procedure, as shown in figure 5.2. These CCSs produce a temperature dependent voltage when powered by a 10 μA constant current source (discussed section 5.6). This voltage is fed through a voltage/temperature calibration curve with a 10 polynomial fit. This

curve was provided with the temperature sensors.

- T1 - top of 50 K shield,

- T2 - 4 K pot,

- T3 - 1 K pot,

- T4 - bottom of 50 K shield,

- T5 - Extra sensor for sample space temperature analysis.

The temperature sensor T3 gives a reading that is close to where the sample sits during the DNP experiment. However it does not give the actual sample temperature. By using an additional temperature sensor (T5) mounted to the end of the wave-guide instead of the sample cup, it is possible to examine the sample temperature and compare it to what is observed at T3. During NMR experiments, T5 is replaced by a normal resistor of a similar value to the CCS outside the magnet. This maintains electric continuity of the temperature detection circuit.

Figure 5.6 indicates that with one vacuum pump drawing liquid Helium in to the sample space, the sample temperature matches the reading from T3. When the second pump is applied and the Joule-Kelvin effect increased, the sample should experience temperatures which are around 0.2 K lower than those observed at T3.

Liquid helium consumption

To cool the sample, the VTI uses a continuous flow of liquid helium from a cryogenic Dewar. It is therefore important to understand the rate at which helium is consumed during the experiment. The flow of helium is controlled via a needle valve on the transfer line. During the initial cooling this valve is opened to one turn, this allows a greater flow of cold gas into the system to enable faster cooling. Upon the commencement of liquid flow this valve is then reduced. By measuring
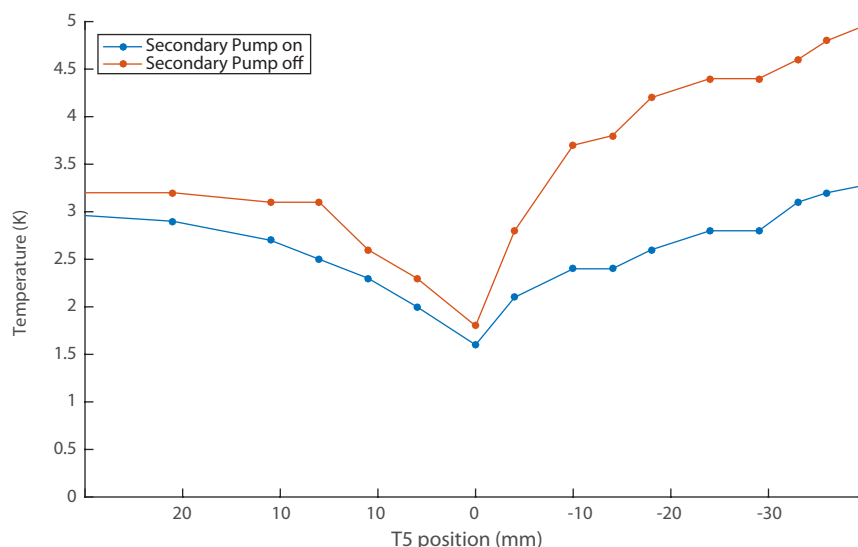
Figure 5.6: Bore temperature as a function of T5 position relative to homogeneous region of upper iso-centre. During the course of this experiment, T3 consistently stated a temperature of 1.8 K. With only one pump on, the sample should experience a temperature which is equivalent to that displayed on T3. With the second pump on, the sample should experience a temperature around 0.2 K lower. All experimental temperatures quoted later in this document are the values observed at T3 without any further correction.

the liquid volume before and after an experiment day it is possible to get a gauge of the overall helium usage. Over a twelve hour day, which starts with the VTI at ambient temperature, the VTI will reliably use between 25 and 30 litres of liquid helium, meaning that the helium usage is around 2.2 lhr^{-1}. Tests were performed in which the VTI was left at around 100 K overnight through a small flow of cold helium gas from the Dewar. This permitted three full days of experiments to be performed with a standard 100 L Dewar.

Sliding Seal

The wave-guide that holds the sample in position during polarisation needs to move through the cryostat during the dissolution experiment. During this motion it is important to maintain the cryogenic atmosphere within the sample space. At such cryogenic temperatures any invasive gases will immediately freeze, poten-
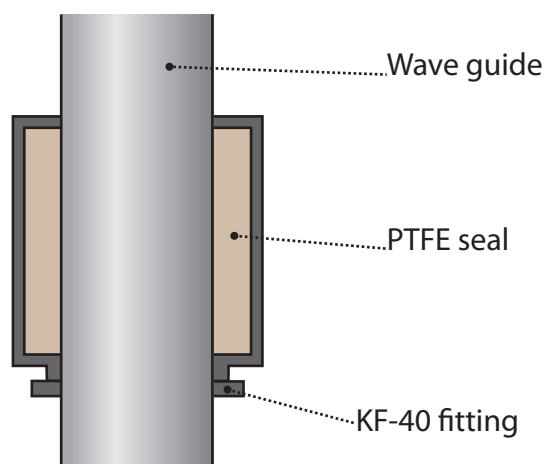
Figure 5.7: Diagram of the sliding seal. A PTFE cylinder forms an air-tight seal with the wave guide. The PTFE is enclosed in an aluminium housing which also has a KF-40 fitting so that an o-ring seal can be formed with the airlock.

tially causing damage to the VTI. To circumvent this problem, a sliding seal is fitted on to the wave-guide through which it can move without compromising the cold inner atmosphere. At the bottom of the seal a KF-40 flange attaches to the top of the cryostat. Inside the seal a tightly fitting PTFE collar forms a vacuum-tight seal with the body of the wave-guide.

Figure 5.4 shows the evolution of the sample space pressure as a function of time with the vacuum pumps switched off. The pressure reading produced by the gauge is calibrated for a true zero, however the scale is consistent. During this test the wave-guide was moved from the 'load-1' position down to 'polarise' and back again. As the wave-guide moves into the bore of the VTI, it displaces some of the volume, increasing the pressure reading of the pressure gauge. When the wave-guide is moved back to its initial position, the volume of the sample space returns to its original value. As the pressure of the sample space returns to where it would have been without wave-guide movement it is expected that the sliding seal does not break its seal upon the change of position of the wave-guide.

Airlock

The sliding seal fits to the top of an airlock that is used to place the wave-guide in a Helium environment prior to insertion into the cold VTI. The airlock is made up of a brass tube and a mini-gate valve (VAT group AG - Haag, Switzerland). The brass tube contains a PTFE locator that centres the wave-guide before it enters the VTI. A thin brass tube, soldered to the main body of the airlock fixes a 6 mm Swagelok valve (Swagelok - Solon, OH, USA) allowing manual control of Helium into the airlock atmosphere. The top of the brass airlock body, a KF-40 flange allows a vacuum seal to be formed with the sliding seal. The same flange at the bottom allows a vacuum sea to be formed with the VAT valve. The bottom of the VAT valve then attaches to the top of the cryostat.

5.4   Microwave system

The wave-guide is moved at various times during the experiment. Therefore it is not possible to physically integrate a low-loss transmission structure to the sample. To transmit the microwaves to the sample a through-air quasi-optic system was developed [52]. This system has not been changed during the course of this project. The microwave source (Virginia diodes - Charlottesville, VA, USA) feeds into a TE_{10}-mode rectangular wave-guide. This source outputs at a power of around 180 mW at a frequency of 11.75 GHz. The frequency of irradiation can be varied over a range of $\pm 0.1 GHz$. The beam is passed through a variable voltage attenuator (ELVA-1 - VCVA-10 - Furulund, Sweden) that allows precise control of the microwave power sent to the sample. Then the microwaves pass through three frequency doublers (ELVA-1 - Furulund, Sweden) to achieve the required 94.0$\pm$0.8 GHz. A TE_{10}-to-Gaussian horn then converts the microwave beam into a quasi-optical form. The Gaussian beam is polarised with a wire grid polarised, this polarisation is rotated with a Faraday rotator and the beam is then reflected 90° down to the top of the wave-guide.
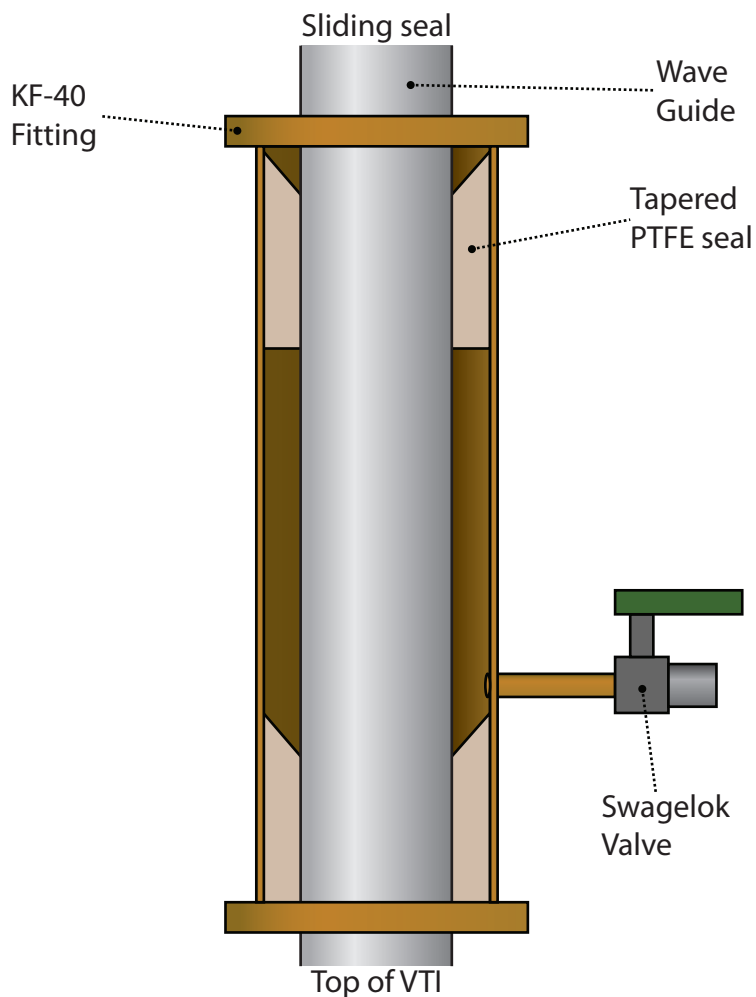
Figure 5.8: The airlock mounts directly onto the top of the VTI allows the waveguide to be removed and reinserted without break the cryogenic helium atmosphere in the VTI sample space. The KF-40 fitting at the top creates an air-tight seal with the sliding seal. Inside the airlock there are two tapered PTFE cylinders which form seals with the waveguide to isolate the inner space. The tapers ensure that the waveguide is smoothly centred into the correct alignment before moving in to the VTI. The Swagelok valve allows the input of helium gas into the airlock prior to loading, this makes sure that only helium can enter the cryostat when it is opened.
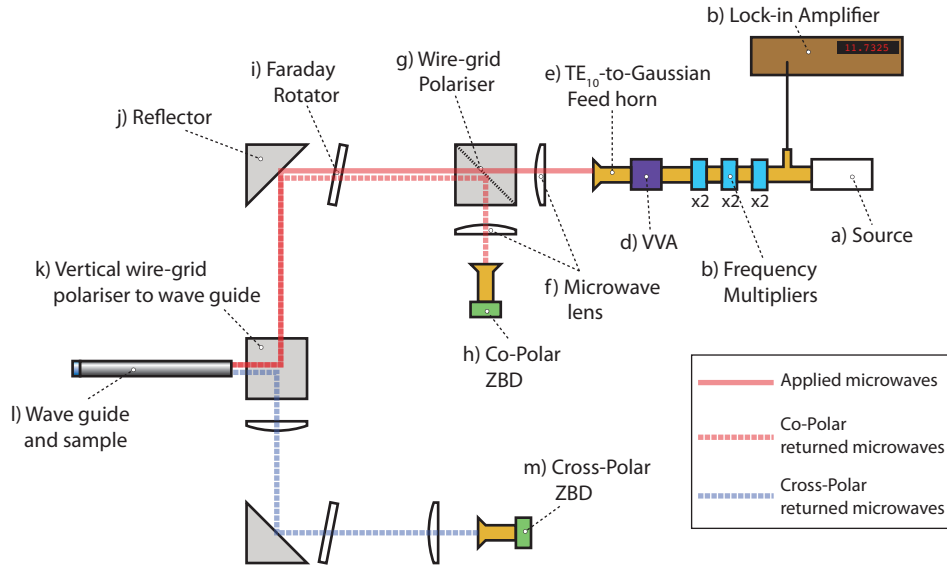
Figure 5.9: Layout of the quasi-optic microwave table. Microwaves are emitted from the source a) into a TE_{10} wave guide at around 11.73 GHz. A splitter takes a small amount of this signal and sends it to a a lock-in amplifier b) for frequency counting. The rest of the signal passes through three frequency doublers c) to reach the desired frequency of around 93.8 GHz. The signal then passes through a Variable Voltage Attenuator (VVA) d) for control of the output power. This signal is then passed through a TE_{10}-to-Gaussian horn e) to feed it into the quasi-optic table. The Gaussian beam is focused with a microwave lens f) before it passes through a wire grid polariser g). The polarisation is then rotated $45°$ by the Faraday rotator i) and then the microwave beam is reflected down into the wave guide. For microwave characterisation, the beam is reflected back up the wave guide for detection. The returned microwaves that are of the same polarisation as the initially applied beam (co-polar) are sent back through the initial quasi-optic path. However, as the microwave beam passes through the Faraday rotator for a second time it will be polarised at $90°$ to the original beam, meaning that it is reflected by the wire grid polariser and sent directly to the co-polar zero bias detector (ZBD) h). Microwaves that are returned from the wave guide that are polarised orthogonally to the initial beam (cross-polar) are sent down a different quasi-optic path to the cross polar ZBD.

81

Microwave Alignment

To align the output from the quasi optics to and the wave-guide, the quasi-optic table is free to move in the x and y horizontal plane. Two micrometer screw gauges allow precise and reproducible locating of the table to an accuracy of 0.1 mm. By placing a flat reflector at the bottom of the wave-guide it is possible to measure the returned microwave power. The zero bias detectors (ZBD - ELVA-1 - Furulund, Sweden) output a voltage which is proportional to the microwave power which reaches the detector plate. By varying the x and y positions of the quasi-optic table and observing the ZBD voltage it is straightforward to find the optimum position. Figure 5.10 shows the observed ZBD voltage as a function of x and y position. This microwave alignment needs to be carried out every time that the wave-guide is removed and reattached to the linear actuator shelf as subtle differences in wave-guide position produce significant drops in applied microwave power.

Initially, the Rexolite window of the wave-guide protruded up into the microwave outlet of the quasi-optic table. This restricted the range of movement available of the table in the x-y plane. The ZBD was used to determine the power loss of the microwaves as the wave-guide was lowered from its initial position. Figure 5.11 shows that the observed power does not diminish significantly if the wave-guide is lowered by up to 4 mm. Setting the polarisation position here allowed the maximum microwave power position to be found.

The microwave power can also be observed as a function of attenuation voltage. This is an important characteristic to know when determine the power required for different DNP experiments. Figure 5.12 shows the observed microwave power for 0 up to 1000 mV attenuation voltages for both cross- and co-polar microwaves. A wire grid polariser separates the cross- and co-polar components that return from the wave-guide. The aluminium reflector at the bottom of the wave-guide changes the 'handedness' of the microwaves upon reflection, hence power is detected at the cross-polar ZBD. The fact that there is zero microwave power detected at the co-
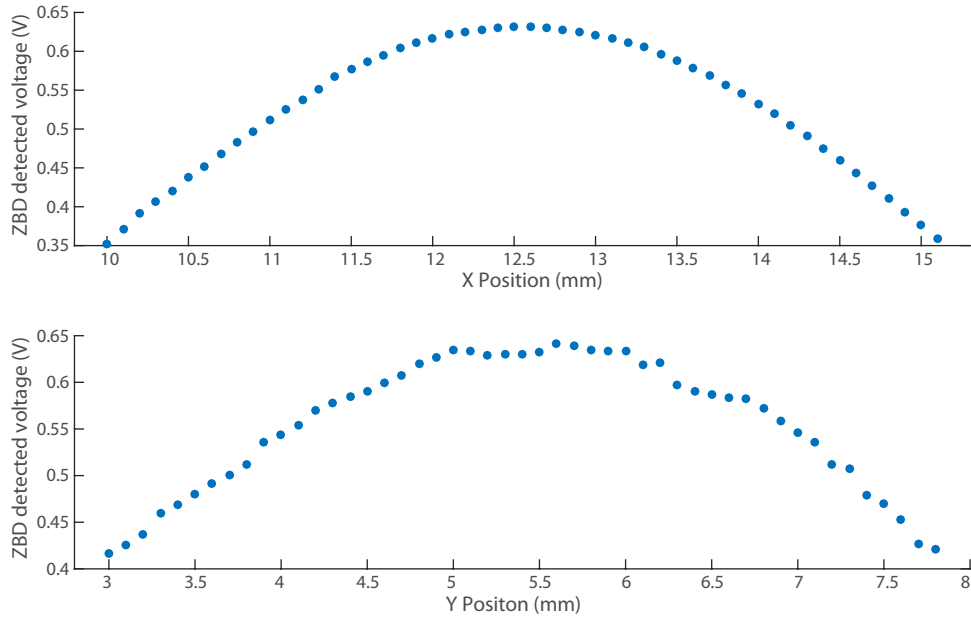
Figure 5.10: Alignment of the quasi-optic Gaussian microwave beam. The beam enters the top of the cryostat through the Rexolite window. A flat reflective plate is fitted to the bottom of the cryostat so that the beam is returned. This beam then travels through the quasi-optic bench to the Zero Bias Detector. The quasi-optic bench is free to move in the x and y plane - perpendicular to the direction of the corrugated wave-guide. The ZBDs output a microwave-field-dependent voltage during irradiation. This voltage is then recorded via the NI DAQ card. The conversion of voltage into absolute power is difficult with older ZBDs as degradation of the device takes the voltage output away from the calibration curves supplied.

polar ZBD indicates that the microwave beam is being polarised successfully by the quasi-optics.

The calculated attenuation from source to detector via the sample was 9 dB. This is significantly larger than previously quoted value of 7.4 dB[52]. One potential source of this discrepancy is that the microwave source has degraded over time. To test this a microwave power monitor (Thomas Keating engineering) was used to directly detect the microwave power output by the quasi-optic table. The wave-guide was lowered and the detector fixed to the top of the Rexolite window, mounted at the Brewster's angle. Microwave power levels were observed for a range of appli-
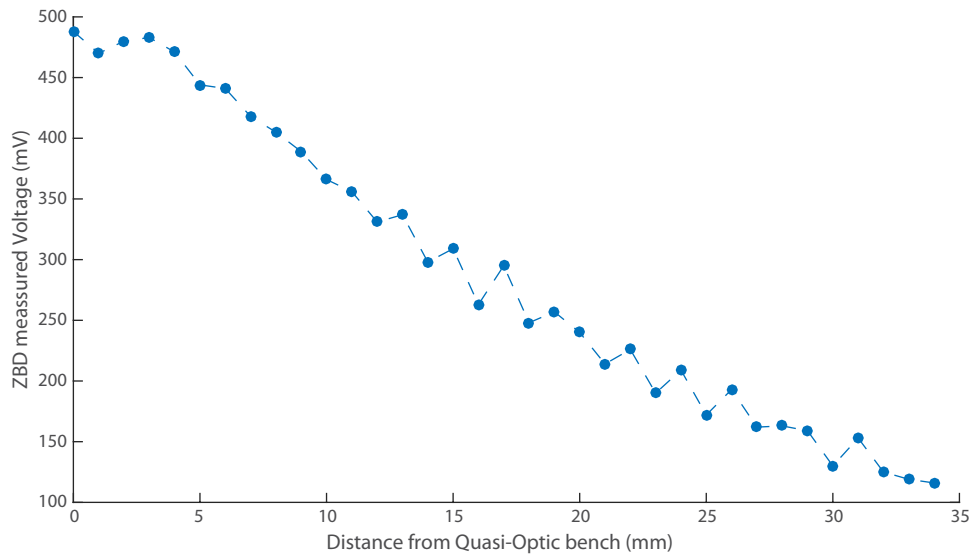
Figure 5.11: Transmitted microwave power reduction as a function of distance from outlet from QOB. Voltages were measured as the wave-guide was moved down from the outlet of the QOB (Quasi-optic bench).

cable frequencies. Figure 5.13 shows how the output power varies with frequency. This indicates that there is a significant drop in power output at lower frequencies. At the frequencies used during the majority of this project (between 93.85 GHz and 93.86 GHz), microwave power is around 70% of the peak value at 94.2 GHz.

The Wave-guide

The sample is held at the bottom of a 1.96 m long stainless steel corrugated wave-guide. A Rexolite window is fitted to the top of the wave-guide structure to ensure a good vacuum seal. Rexolite is near-invisible to microwaves (dissapation factor is 0.00066 @ 10 GHz - www.rexolite.com/specifications - accessed December 2016) so the window does not reduce the input microwave power. Inside the wave-guide, the corrugated structure converts the incoming Gaussian beam into a HE_{11} field which propagates down towards the sample. At the end of the wave-guide, a brass taper focusses the field down onto the sample.
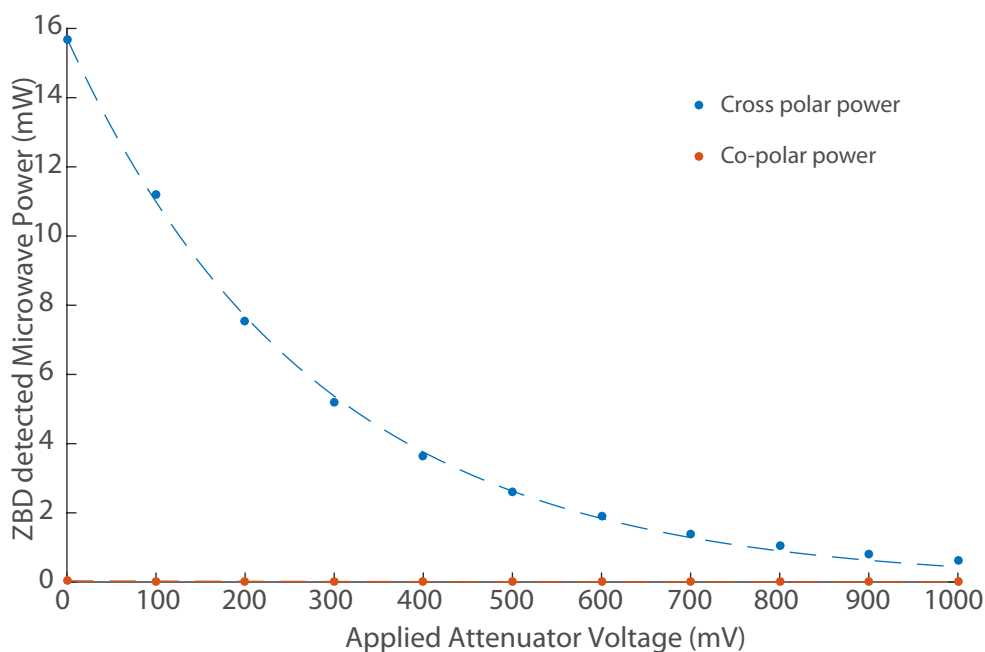
Figure 5.12: Observed microwave power at different attenuation voltages. Microwave power was calculated for different attenuations at the optimum alignment of the QOB and wave-guide. The power observed by the ZBD gives a measure of the power remaining following the path from the source to the sample and then back up to the detector, therefore it represents nearly twice the attenuation of the beam that interacts with the sample during DNP experiments.

5.4.1 Microwave Sweeps

Different nuclei will react differently to the applied microwave field. To characterise each sample and find the optimum microwave frequency required for polarisation, DNP profiles can be produced. These curves show the increase in nuclear polarisation with respect to the microwave field frequency. DNP profiles also give information about the polarisation processes which are happening within the sample as the optimum frequencies often coincide with the resonance conditions of the different DNP effects.
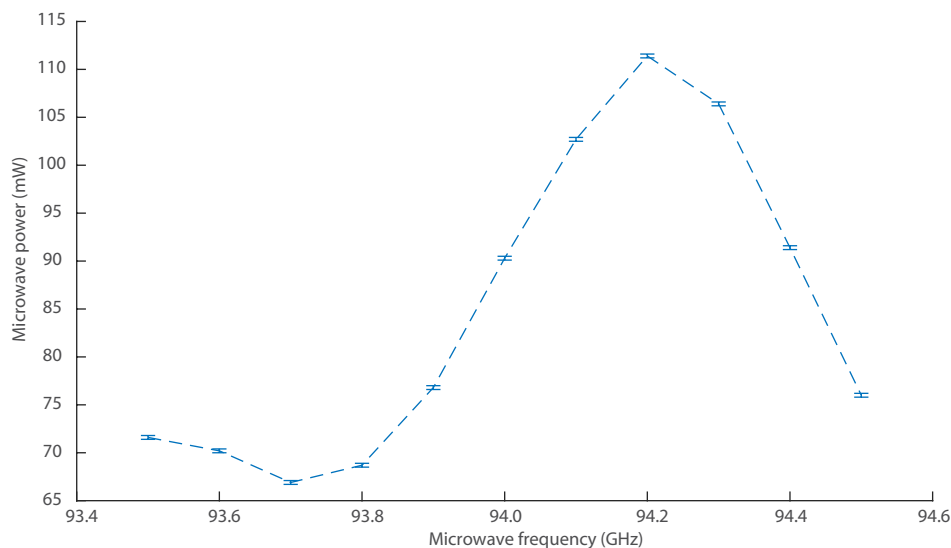
Figure 5.13: Observed microwave power as a function of frequency. This power was measured at the outlet of the quasi-optic bench immediately prior to the beam entering the wave guide. The power was tested with a Thomas Keating microwave power monitor mounted at the Brewster's angle. At time of production, the microwave source would have developed a consistent power output across the available frequency range. Over time, however the source has degraded such that there is a significant dependence on microwave frequency. This data indicates that the source is not functional in an optimal fashion and will, in part, account for the relatively low observed nuclear polarisation.

5.5 Sample Dissolution System

In order to observe the hyperpolarised sample in liquid state, a robust and reproducible heating mechanism is required to bring the frozen sample back up to ambient temperature. As discussed in section 4.3 there are a different ways to approach sample heating. Here, a heated solvent is applied to the frozen sample. The system presented below allows cryogenic temperature samples to be dissolved and injected into a NMR probe in less than half a second without using superheated solvent at high pressures.
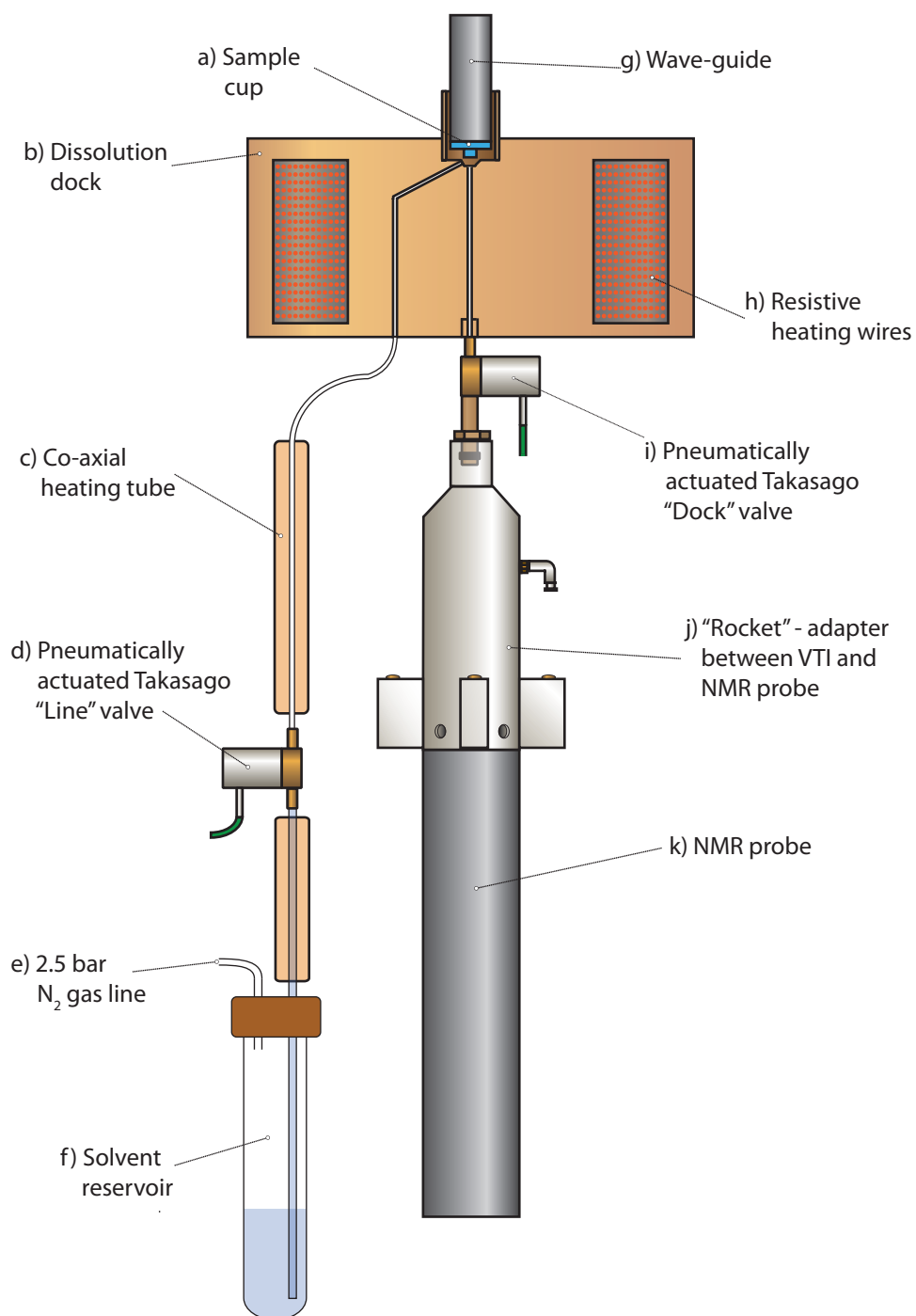
Figure 5.14: The dissolution set-up. Solvent is loaded from the non-magnetic, pneumatically-operated, 'line' valve down into the solvent reservoir. This reservoir is pressurised with 2.5 bar nitrogen gas. During the dissolution process, the wave-guide moves down into the dissolution dock, where a small mixing area allows the flow of heated solvent to interact with the cold sample. A second valve controls the flow of this liquid into the probe via the 'rocket' probe adapter.

5.5.1 The Dissolution Dock

The dissolution dock was redesigned to produce a more reliable dissolution process. The dock itself is made of a cylinder of PEEK of radius 150 mm and height 100 mm which mounts directly onto the bottom of the VTI. On the top face of the dock a 20 mm opening allows the wave-guide to move around 5 mm into the dock. A 5 mm chamfered hole in the centre of the opening provides a location for the sample cup (attached to the end of the wave-guide) to form a tight PEEK on PEEK seal. On the bottom of the dock a 4 mm o.d. Nylon tube, with a PTFE Swagelok fitting allow delivery of solvent from the water heating tubing into the sample space. Also on the bottom face, an 8 mm threaded outlet hole allows the connection of the dock valve (Takasago- Nagoya, Aichi, Japan). In the body of the dock many turns of resistive heating wires allows the maintenance of dock temperatures of more than $0°$ C below the cold VTI.

In the first part of the dissolution procedure the frozen sample is rapidly moved 80 cm down from the 3.35 T iso-centre to the dissolution dock. With the current actuator parameters this movement takes 600 ms. Subsequently, the wave-guide is moved slowly down until it makes a firm connection with the dissolution dock. The motion is torque limited so the actuator stops automatically once the connection has been established. Once the wave-guide is docked, it forms a small mixing region with one inlet and one outlet.

5.5.2 Solvent delivery system

The solvent used for sample dissolution needs to be maintained at a temperature of just under 100 °C until the wave-guide has successfully docked. To accomplish this, co-axial tubing was used. The solvent is placed inside the inner tube with the outer tube acting as a thermal jacket. The outer tube is connected to a heated oil bath (Thermo Haake F8 - Karlsruhe, Germany) which maintains the oil at the required temperature. The oil is then pumped around the solvent tube and back to

the heater. Figure 5.14 shows the configuration of the dissolution system. The flow of liquid is controlled by two pneumatically controlled valves (Takasago Electrics inc. - Nagoya, Aichi, Japan). These valves are non-magnetic so can be placed inside the magnet. They are air operated by a 4 bar gas supply which is, in turn, controlled by a series of electronic valves. This allows remote control of the solvent flow via computer. The solvent tube (Nylon - 4 mm o.d. / 3 mm i.d.) is coupled to the inlet of the dissolution dock with a 4 mm PTFE Swagelok fitting. A second Takasago valve ('Dock valve') is placed at the outlet of the dissolution dock. After this valve, a small PEEK 1proboscis' allows an o-ring sealed connection between the dock and the NMR probe.

The solvent reservoir is large enough to store around 25 ml of solvent and is sealed via a o-ring fitting at the top. The solvent tube protrudes down into the reservoir. The reservoir is also connected to the nitrogen gas supply so that it can be pressurised to pneumatically drive the solvent to the dock.

5.5.3 Interfacing Probes with the Dissolution DNP system

The ability to deliver hyperpolarised samples to commercial liquid-state probes opens up greatly enhanced functionality for the experimental set up. Most general-use Bruker probes share a geometry, only the internal design differs. Hence, a single adapter is needed for the majority of probes to work 'out of the box'. Figure 5.15 shows the adapter, known as the 'Rocket', which was designed for this purpose. The adapter is a continuation of the fluid flow path from the bottom of the dissolution dock. The top of the adapter forms an o-ring sealed connection to the proboscis of the dock. This then flows into a small 2 mm i.d capillary. Inserted into the capillary is a short piece of glass tube which feeds into a waiting NMR tube. This glass tube has been modified such that the end of the tube bends 45° and tapers. This bend forces the flow of liquid to jet onto the side of NMR tube and flow down the side, reducing turbulence and bubble formation.

The NMR tube itself forms an o-ring sealed connection with the probe adapter. The internal volume of the NMR tube is isolated from the surrounding environment. A small opening on the side of the adapter contains a push fit gas connector that is attached to a vacuum pump. The NMR tube needs to be shorter than normal such that the length is no more than 100 mm. The tube can then be screwed into the rocket via the vacuum-tight seal. A Delrin tube locator is used to position the tube in the correct position so that it comfortably fills the NMR coil region of the probe[2].
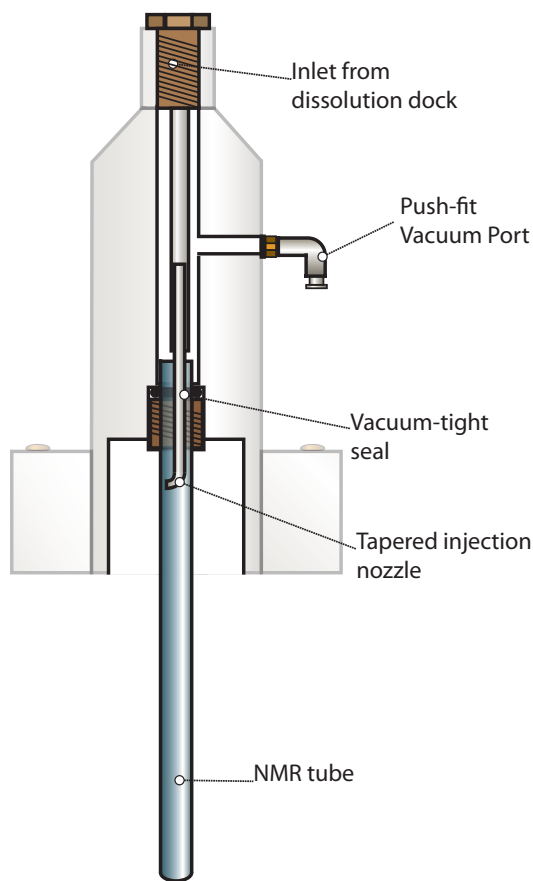
Figure 5.15: The Rocket: Probe adapter for dissolution system. The NMR tube forms a o-ring vacuum seal with the upper section of the adapter. The liquid is forced through a tapered glass nozzle on to the side of the NMR tube.

---

[2]The dimensions of this locator are based on the position found with the spinor and transparent coil locator used in conventional NMR

5.5.4   Dissolution sample cup

The dissolution sample cup has been designed to aid both the dissolution process and the propagation of microwaves. Samples of up to 50 μL can be placed in the Rexolite cup. The wave-guide tapers the microwaves down to 5 mm at the outlet. The outer diameter of the sample cup is 18 mm so that it matches the flange of the wave-guide. The Rexolite cup is surrounded by a 6 mm i.d. copper pipe. This increases the propagation of the microwaves after the outlet of the wave-guide.

The sample cup is held upside down on the end of the wave-guide. The inner diameter of the Rexolite cup is small enough for the surface tension of the liquid to form a concave meniscus and hold it in place.

5.5.5   Solid state probes for quantification of DNP

To quantify the build up of nuclear polarisation in the solid-state, resonant probes must be built for each nuclear spin species. There are two rigid co-axial transmission lines attached to the outside of the wave-guide that allow electronic access to the sample space. Static solid-state coils with local tuning and matching networks can then be placed directly on to the end of the wave-guide. The probes consist of a saddle coil (single or double turn winding) attached over a Perspex spool-shaped coil holder. The capacitors that form the tuning and matching network are then placed in the space left by the microwave taper. It is preferable to locally tune and match the solid state coil as the transmission lines run the length of the wave-guide (1.96 m). Remote tuning over such a distance would greatly impair the performance of the probe. The capacitance values required to tune a given nucleus are not always obvious, as capacitors are not generally designed to go below 2 K. At low temperatures, mechanical changes to the capacitor structure, as well as non-linear variation in the dielectric material between the capacitor plates, means that trial and error must be used to find the correct values that give an appropriate resonant frequency below such temperatures.
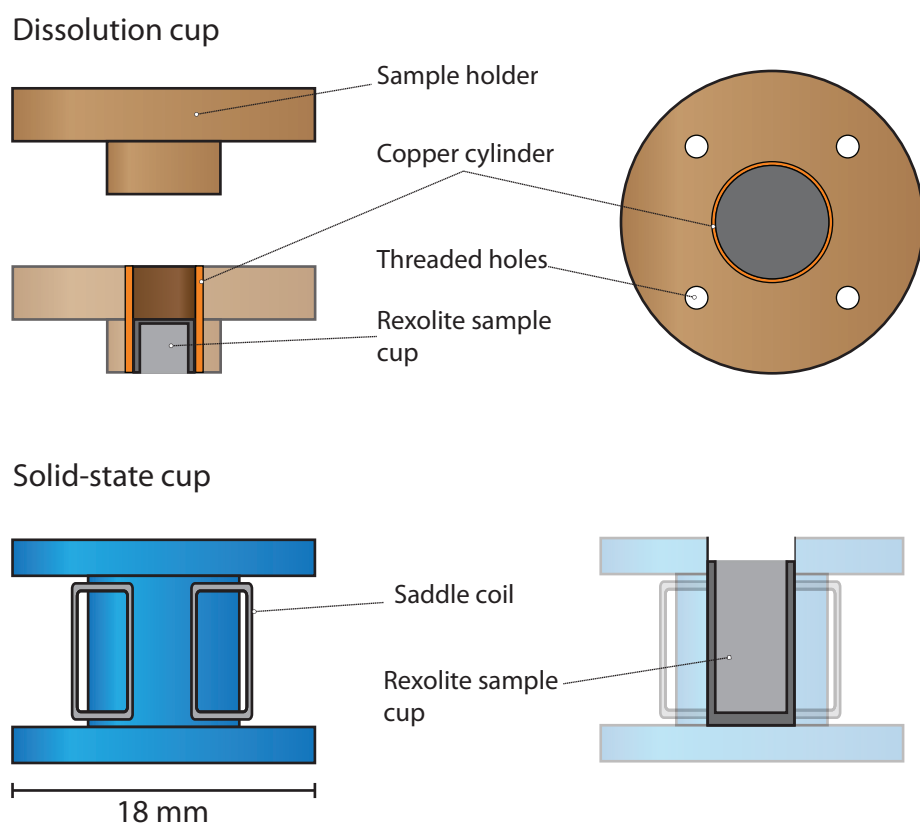
Figure 5.16: Diagram of the sample cups used in this project. TOP: The dissolution cup used for performing dissolution experiments. Approximate sample volume of 30 μL BOTTOM: The sample cup used for solid-state analysis of DNP polarisation build-up. Approximate sample volume of 50 μL
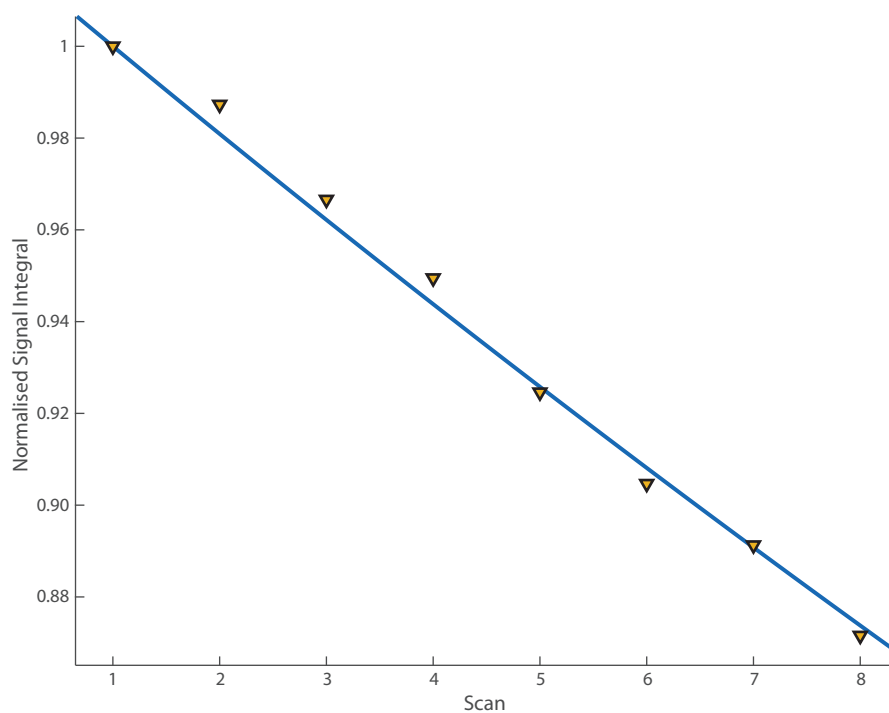
Figure 5.17: Solid State pulse determination by analysis of signal intensity. Data were acquired from 2 M [1−^{13}C] Sodium Acetate in 50:50 (by mass) water/glycerol solution and approximately 15 mM Trityl radical. Sample was held at around 1.9 K for duration of the experiment. This figure shows the spectral integral as a function of number of scans. The flip angle can then be determined by fitting this data with equation 5.1. This fit shows that the pulses produced a nutation angle of 11°.

Pulse calibration

Pulse calibration is needed to set up an NMR experiment. However as the T_1 relaxation times are incredibly long at low temperatures, configuring a 90° pulse by increasing the pulse width over a series of experiments would take a prohibitively long time. Instead, the long T_1 time can be used as an advantage to determine the flip angle of an arbitrary pulse.

By acquiring a set of solid-state spectra over a few seconds it can be assumed that there is negligible T_1 relaxation in between the individual scans. As the observed signal is proportional to the remaining magnetisation after the previous scan(s) then is is straightforward to fit the integrals of the individual spectra as a function

of number of previous scans.

$$I(n) = I_0 \cos(\theta)^{n-1} \tag{5.1}$$

Where the integral I after n scans is proportional to the signal observed after the first scan I_0. By normalising the integrals to the first scan $I_0 = 1$. Figure 5.17 shows this fit for a eight scans. The pulse power was 20 W for 10 μs. The fit indicated that the flip angle was 11°.

5.6 Controlling the system

The dissolution experiment requires the multiple components of the instrument to perform in a synchronous and repeatable manner. Therefore a central control unit for all aspects of the instrument is required. The control system in place on the dual core system is based around two computers. One controls the spectrometer through TopSPIN 3.2 (Bruker GmbH - Karlsruhe, Germany), the other controls the dissolution system and microwaves through two data acquisition cards and two LabVIEW control virtual instruments (VIs). From the control DAQ (National Instruments USB-6218 - Austin, TX, USA) the control VI takes in analog signals from the five carbon ceramic temperature sensors (CCS); an electronic pressure gauge and two flow sensors. It also receives digital inputs from four position sensors attached to the support actuator rails that move the wave-guide. Digital outputs from the NI-DAQ can then operate five electronic valves and a TTL switched power supply for the small vacuum pump.

All of the I/O of the control DAQ are routed through a custom made routing box consisting of twelve 9-pin RS232 connectors. The NI-DAQ USB-6218 is housed within this routing box. A 10 μA constant-current source delivers power to the CCS connectors and is attached to the routing box via BNC. A 22 mV reference signal is also output from the current supply to the routing box for calibration of
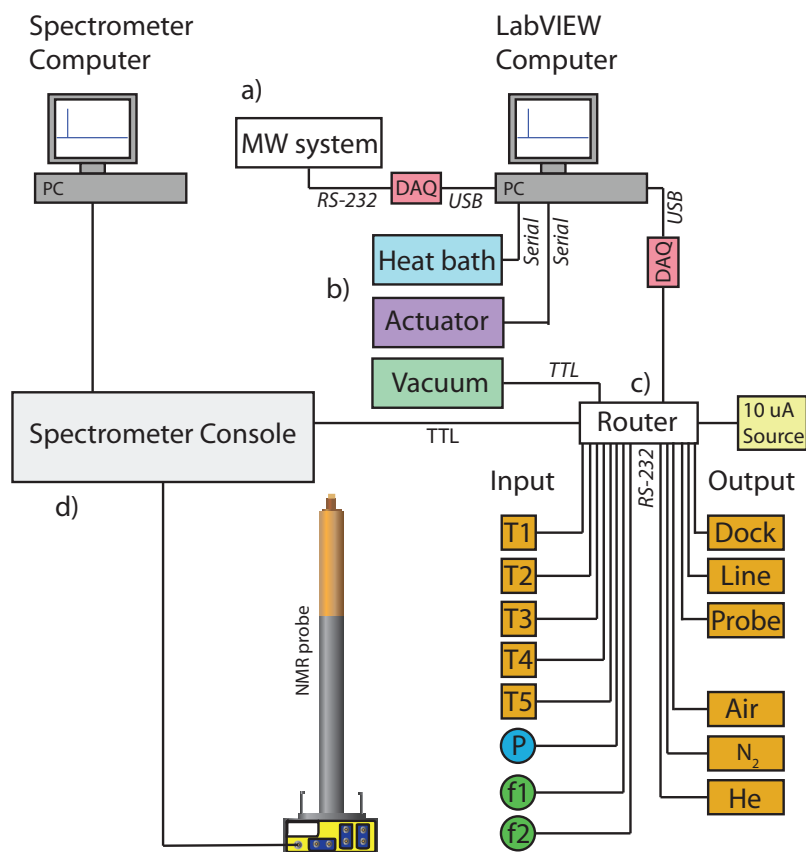
Figure 5.18: Routing diagram of the system control apparatus. The control system comprises of two computers, the first one interfaces with the spectrometer console and allows detection of NMR signals. The second computer uses LabVIEW programs to read in data from the sensors and to control the valves and actuator. a) The microwave source and the variable voltage attenuator are controlled via a data acquisition card (DAQ-National Instruments). b) The Heat bath and the actuator system connect directly to the labVIEW computer, communication between these devices is via serial com ports. c) The majority of the I/O goes through an electronics routing box. This box takes the inputs from five temperature sensors (T1:5) a pressure sensor (P) and two flow sensors (f1:2) and routes it to the necessary analogue inputs on a second DAQ card (National Instruments). The temperature sensors also take power from a 10 μA constant-current source. The flow sensors and pressure gauge also receive 24 V power from the routing box. Digital outputs from the DAQ card control electronic valves attached to pressurised gas lines. d) The spectrometer console is attached to the spectrometer computer to enable NMR detection from the probe. It also has a two-way TTL connection to the LabVIEW computer via the router and DAQ card. This allows synchronisation between the dissolution system and NMR detection.

the detected CCS voltage. The control DAQ is then connected to (and powered by) the computer through USB.The second DAQ is used to control the microwave source and variable voltage attenuator.

The oil bath is attached to the control computer through a serial com port. The control VI has access to control and monitor the oil bath temperature. The linear belt actuators (FESTO - Esslingen am Neckar, Germany) are also controlled through a serial com port. The FESTO control unit allows a 'position set table' to uploaded directly to the actuator system. The transitions between these positions can then be triggered by the LabVIEW control VI. The four position sensors are placed at important positions along the actuator path, they detect the actuator shelf which supports the top of the wave-guide.

Triggering the NMR console

To take full advantage of the rapid dissolution procedure, it is important to trigger the NMR acquisition at a precise time after the delivery of the hyperpolarised liquid. To accomplish this, a positive-edge digital signal (from a NI-DAQ card) is sent to the spectrometer immediately prior to the opening of the dissolution valves. There is a small computing dead time following the TTL signal. This was measured by extracting a small amount of NMR pulse power from the spectrometer console with a -40 dB directional coupler. This pulse power and the TTL signal were observed on a digital oscilloscope for various pre-scan delays. The computing dead-time was consistently 13.7×10^{-6} s regardless of the following delay time. This time is much shorter than the delay times that are used in the experiment and therefore can be neglected in most circumstances.

5.6.1 Characterising the Dissolution Procedure

There are a number of important characteristics of the dissolution procedure that need to be determined for an analysis of the effectiveness of the new dissolution set
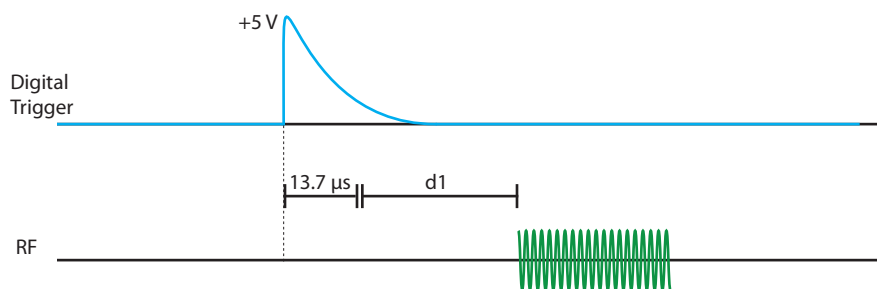
Figure 5.19: RF timing after digital trigger from LabVIEW control program. Between the triggering of NMR acquisition and the commencement of the RF program there is an additional dead time of 13.7 μS. This is consistent regardless of the experimental parameters and is a result of the internal functioning of the spectrometer.

up. For mass-limited samples it is important to get as much of the polarised sample into the NMR tube as possible. It is also preferential to use the least amount of solvent possible so that the dilution factor of the initial sample remains small. For biologically relevant samples, it is crucial that the temperatures that the sample experiences during dissolution are considered. Finally, as the liquid is flowing at a high rate, turbulences in the flow and out-gassing from the sample will create bubbles in the NMR tube. Attempts have been made to mitigate the effects of bubble formation however a settling time is required immediately following sample dissolution. This section provides a comprehensive analysis of the new dissolution apparatus and discusses its effectiveness.

Sample Concentration

A limitation of dissolution DNP is that the polarised sample is diluted by the heated solvent. While this reduction in signal is more than overcome by the enhanced nuclear signal, it is still important to get as much of the initial sample into the NMR probe for liquid state testing. This is especially important in cases in which only small amounts of the molecule of interest are available. There are two important factors that determine the concentration of the nuclei of interest in the final dissolution sample:

1. The amount of frozen sample successfully melted,

2. The final volume of liquid in the probe.

There are four important variables that can be altered in this system: The temperature of the solvent; the amount of time the dock and line valves are open; the driving pressure; and the amount of frozen sample to be melted.

As the predominant solvents used in the project were water and D_2O, the solvent temperature was set permanently just under 100° C. This was achieved by setting the oil bath to circulate oil at exactly that temperatures. There is a small amount of thermal loss through the coaxial heating tubing. Thermal imaging of the coaxial tube showed that during this procedure the solvent should not experience temperatures under 90° C along the heated flow path. Heating the solvent up to close to its boiling point was crucial to thaw the frozen samples as quickly as possible.

Initial testing of the dissolution system used blue food colouring as the 'molecule of interest'. This was used as it allowed analysis of sample concentrations following dissolution. A UV/VIS spectrophotometer was used to characterise the absorption of dissolution samples compared to a reference sample of know concentration.

Valve timings

The amount of liquid that can flow through the system can be controlled by the precise opening and closing of the dock and line valves. The simplest way of operating these valves is for them to open and close simultaneously, then the amount of liquid that travels through the tubing is controlled by the driving pressure and the duration that the valves are open. The sample volume was measured for a range of valve timings with the backing pressure set at 2.5 bar.
Figure 5.20 shows that the desired sample volume can be tailored to the experimental requirements.
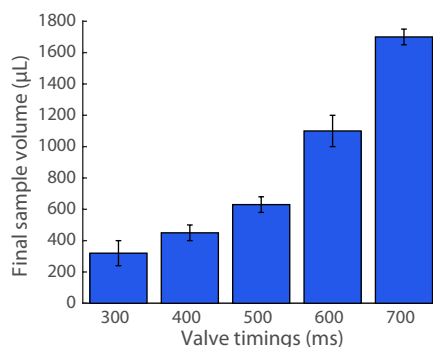
Figure 5.20: Dissolution volume as a function of valve timings. By changing the valve timings, the total amount of liquid deposited into the NMR tube can be changed.

Initial sample volume

The sample that sits in the Rexolite sample cup is small compared to the amount of heated solvent used to bring about the temperature jump. It is important to optimise the amount of sample placed in the sample cup to maximise the concentration of hyperpolarised sample that reaches the NMR probe. As the microwaves propagate through the sample, they will decay with a characteristic skin depth in the dielectric sample. For this reason, the top of the sample will see a greater microwave power than the bottom. While the permeability of microwaves through DNP samples is of particular practical significance a literature search has yet to reveal any studies into such mechanisms.

To test how final concentration varies with initial sample volume dissolutions were performed for a small range of sample volumes. The food colouring sample was taken down to around 80 K with liquid nitrogen. Dissolutions were performed with water heated to just under 100° C. The dissolution valves were open for 550 ms with a driving pressure of 2.5 bar. Figure 5.21 shows the fraction and volume of food colouring that reaches the NMR tube for a range of initial sample sizes. The error bars indicated the standard error based on five dissolution trials. Smaller samples allow for more complete washout of the sample cup. This is logical as there is less frozen sample to heat up. 30 μL provided on average the most amount

of food colouring in the NMR tube, however there was considerably more varia-tion between trials. Therefore 20 μL was used in further testing of the dissolution system. Data for 25 μL were not acquired during this set of experiments. Within error, the total volume observed reaching the NMR tube for these experiments was not dependent on sample cup volume. With the Takasago valves open for 550 ms around 710 ± 40 μL were present in the tube.
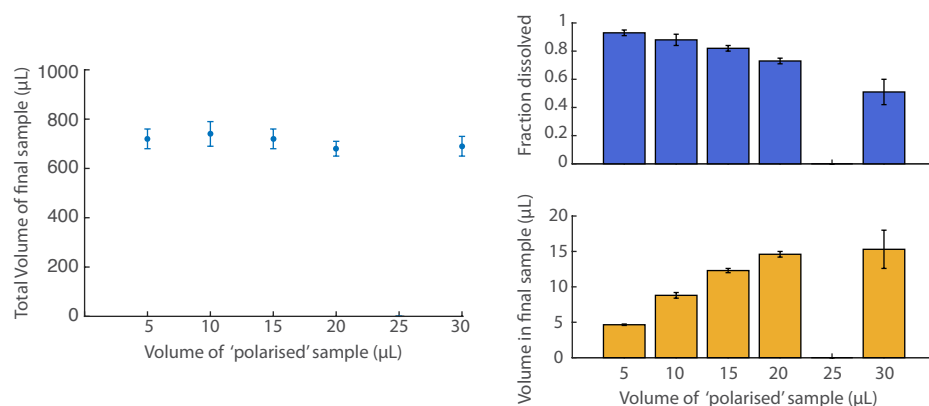
Figure 5.21: Percentage and volume of blue food colouring in the final sample. LEFT: The total observed volume in the NMR tube following the dissolution process with is not dependent on the volume of polarised sample in the sample cup. RIGHT TOP: As the volume of polarised sample in the sample cup is increased, the amount of that sample which is successfully dissolved reduces. RIGHT BOTTOM: The total volume of polarised sample that reaches the NMR tube as a function of the initial amount of sample placed into the sample cup.

Sample Temperature

For biologically relevant samples, it is important to ensure that the dissolution sam-ples are not excessively hot when they arrive in the NMR probe. To test the incom-ing temperature, the chemical shift of the water peak is considered. The hydrogen nucleus of water has a chemical shift which is temperature dependent. This means that the temperature of resultant liquid is documented during the normal course of the experiment. The chemical shift can then be compared to a calibration curve of known temperatures. The calibration curve was made with 99% D_2O containing

1% DSS standard (Sigma-Aldrich - St. Louis, MO, USA). Temperature was controlled with the Avance III variable temperature unit (Bruker GmbH - Karlsruhe, Germany). Figure 5.22:LEFT shows the water chemical shift for the range 290 K to 332 K.
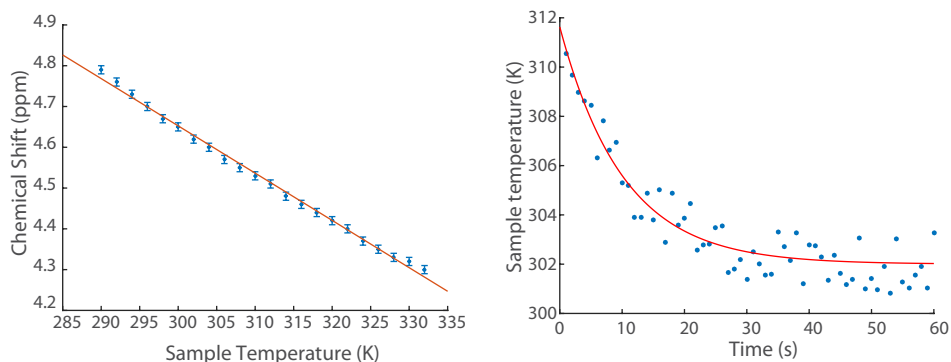
Figure 5.22: LEFT: Calibration curve of Water peak chemical shift as a function of sample temperature. The linear fit allows determination of the temperature of the sample immediately following the dissolution procedure. RIGHT:Sample temperature following dissolution. The water peak chemical shift was observed as a function of time following dissolution. This shift was then mapped into temperature using the previously obtained calibration curve.

The water hydrogen signal was observed during a dissolution from 2 K and the chemical shift compared to the calibration curve. This provided temperature information for the sample following the dissolution. Figure 5.22:RIGHT shows that the fluid arrives at the NMR tube at around 312 K and cools over the first 40 s down to ambient temperature. This ambient temperature in the magnet bore will be warmer than the surrounding lab as the bore of lower iso-centre is heated by the co-axial heating tubes.

5.6.2 Bubble formation

Initial dissolution tests showed significant bubble formation during the dissolution procedure. Bubbles are a major problem for NMR experiments as interfaces between gas and air produce susceptibility mismatches which distort the field, reducing field homogeneity. Larger bubbles also remove hyperpolarised liquid from the

sensitive region of the RF coil, reducing the number of observed spins and reducing signal-to-noise. A comprehensive analysis of injection dynamics for dissolution-DNP is presented by Granwehr and co-corkers [87].

During the dissolution procedure, the heated solvent experiences a large pressure drop, from 2.5 bar immediately proceeding dissolution to less than atmospheric pressure in the NMR tube. Gases dissolved in the liquid at higher pressures can be forced out of the liquid as it degasses. This can be remedied by adequately degassing the solvent prior to the experiment. All dissolutions use solvent that has been through at least three freeze-pump-thaw degassing cycles. The method used here to produce such liquids involves applying a vacuum to de-mineralised ice as it melts. Degassing the sample in this way cannot remove all of the gas dissolved in the solvent. Once degassed, the solvent produces a significantly smaller amount of bubbles, however small micro-bubbles still form during the liquid flow. By observing the line width of a water peak as a function of time, the affect of the susceptibility miss-matches can be quantified. Figure 5.23 shows the evolution of the water peak line width for the time post-dissolution. Time zero indicates the time at which the dissolution valves are opened, this means that the first 300 ms involve the filling of liquid within the NMR sample tube. The following 300 ms show a rapid decrease of water line width. This decrease is associated to the dispersion of micro-bubbles.
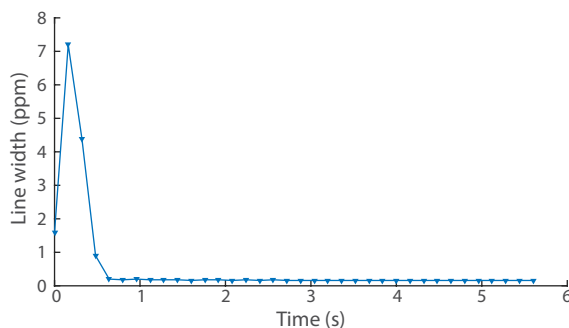
Figure 5.23: *Water peak line width during the dissolution procedure. The line broadening associated with the dispersion of micro-bubbles in the fluid has subsided after about 600 ms. Spectra were acquired every 150 ms following dissolution.*

Imaging micro-bubbles following dissolution

To further characterise the sample filling process, a time resolved set of 1D images were acquired during the dissolution procedure. Figure 5.25 shows the time course of images acquired in the Broadband-inverse probe (Bruker) and is made of 512 1D gradient echoes. The basic structure of a gradient echo sequence is shown in figure 5.24. An initial pulse rotates z-magnetisation into the x-y plane then a dephasing gradient is then applied. The x-y magnetisation is then rephased by an opposite gradient applied for twice the duration of the first. This encodes spatial information in the spread of frequencies observed in image. A comprehensive introduction to gradient echo MRI can be found in [88]. In this experiment a small ^{1}H pulse (1 W - 2 μs) was followed by a 5 ms positive gradient at 4% power from a Bruker GREAT-10 gradient amplifier. This provides a total field gradient of $114\mathrm{mT/m}$. Each echo was acquired with 768 complex points with a total acquisition time of 12 ms. The overall repetition time of the sequence was 40 ms.

Initially, the water is sitting outside the magnet - it is held at pressure behind the line valve. While the fluid will be sitting in the stray field of the magnet, the level of magnetisation will be insignificant polarisation prior to the triggering of the dissolution. During and after the NMR tube as been filled, the magnetisation of the liquid builds up to the new equilibrium with a T_1 of around 2.5 s. The NMR tube fills in around 300 ms, this is observed as the initial period of zero signal. The diagonal lines on the figure are the micro-bubbles moving up through the sample and dispersing. The majority of the micro-bubbles dissipate over the first 5 seconds following dissolution. As this time is significantly longer than the settling of the line width show in figure 5.23 it is concluded that these micro-bubbles do not have a large effect on NMR acquisition. Only the highly turbulent initial filling and settling of larger bubbles needs to be considered for setting a settling delay.

The dissolution set-up presented here provides a consistent and reliable basis for performing dissolution DNP experiments. The combined sample delivery time of
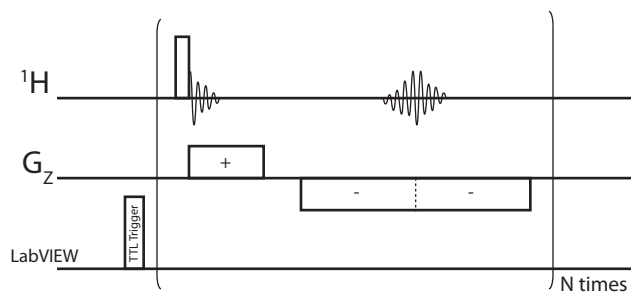
Figure 5.24: Pulse program of triggered 1D gradient echoes. Once the dissolution sample has been delivered to the NMR tube the LabVIEW control program sends a trigger to the spectrometer to begin acquisition. During the gradient echo sequence the proton spins are transferred into the x-y plane with a $\pi/2$ pulse. Following this a positive z-gradient is applied to the processing spins, encoding spatial information, the evolution of the spins under this first gradient, shown in the figure as an FID, is not recorded. After a small evolution time a negative gradient of the same strength is applied to the sample for twice the duration of the first. The peak intensity of the spin echo is observed at the mid-point of the negative gradient.

300 ms and and settling time of another 300 ms is still fast enough to observe spins with T_1 relaxation times under 200 ms.

5.7   Performing Dissolution DNP

All of the hardware described so far in this chapter works together to act as a dissolution DNP spectrometer. However, all of the components must be used appropriately for the experiment to work and hyperpolarised liquid to be produced. Determining the most reliable and efficient manner with which to operate the system has taken extensive testing and many failed attempts. This section will provide a practical overview of the running of the system, it can be considered to be a 'Standard Operating Procedure'.

5.7.1   Cooling the VTI

Before the system can be cooled, it is important to ensure that there is no liquid anywhere in the VTI or the transfer line. Initially both are flushed with dry helium
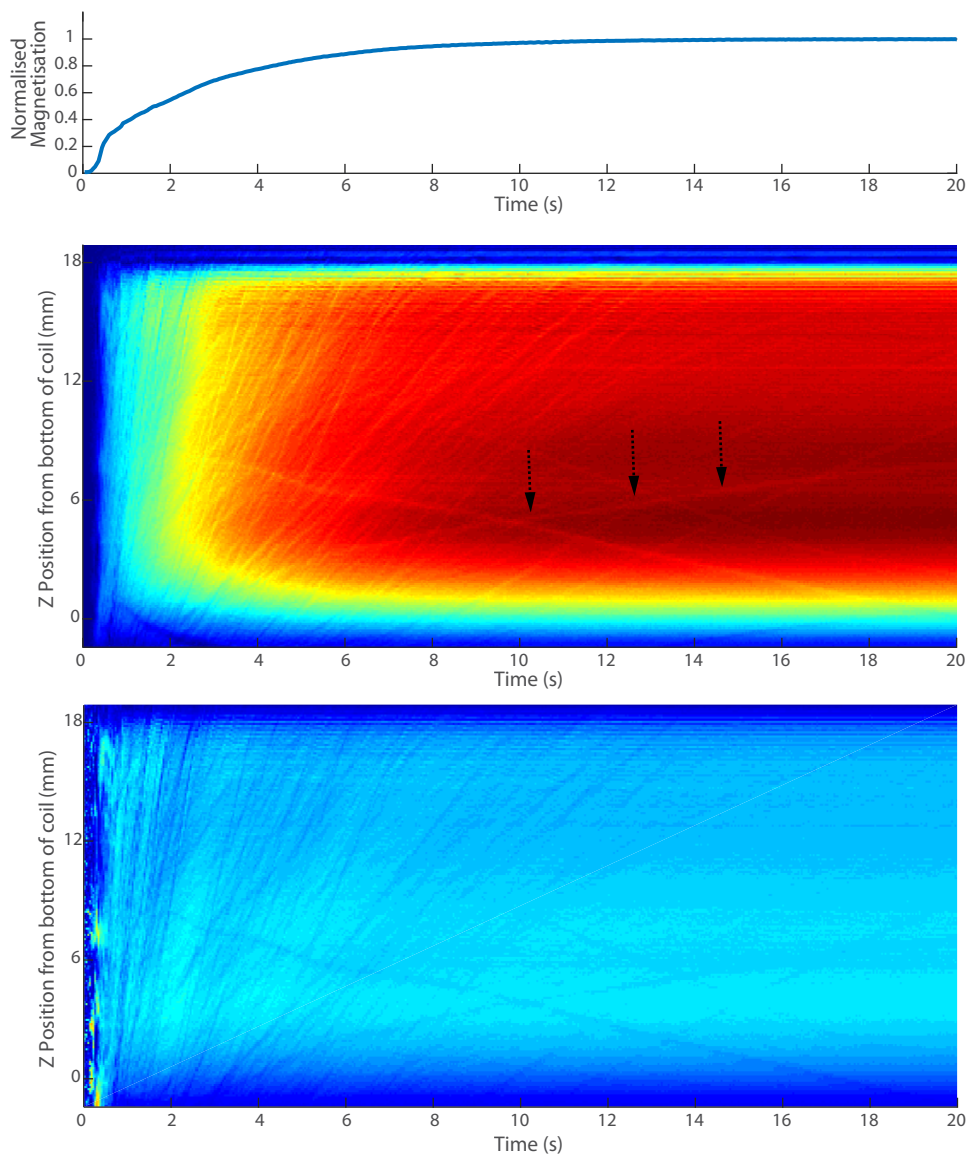
Figure 5.25: TOP: Averaged intensity of each slice as function of time. Build up follows re-equilibration of magnetisation in the magnetic field following normal T_1 relaxation with a relaxation time of 2.65 ± 0.04 s. MIDDLE: Time series of 1D projections along the length of the NMR tube. Micro-bubbles can be observed travelling up the length of the NMR tube. The trajectory of one bubble is marked by the arrows. BOTTOM: Time series of 1D projects which have been normalised for the T1 build up of nuclear polarisation.

gas for at least half an hour before insertion of the transfer line into the helium Dewar.

The small vacuum pump is sufficient to draw the cold gas and liquid from the Dewar and into the VTI, therefore the Dewar is left connected to the Helium recovery line with the valve open.

The early stages of cooling involve cold Helium gas filling the VTI, the fastest stable method at this stage is to only pump slightly on the VTI bore and maintain a cold Helium gas pressure of around 600 mbar. Temperatures around 15 K can be achieved within one hour of cooling. The system will not cool further until the pressure has been reduced to at or below 200 mbar, this will reduce the temperature to around 7 K. At this point some liquid Helium should be able to reach the 4 K pot without evaporating so the full pumping power of the main vacuum pump can be used on the VTI bore and the cryostat needle valve reduced to near closure, this limits the flow of Helium into the bore and begins the Joule-Kelvin expansion of the liquid. The temperature in the sample space will reach 2 K or slightly lower almost instantaneously. Once the system has settled and the temperature is consistent the second bore pump can be activated to reach a base temperature of around 1.7 K.

5.7.2   Sample Insertion

The sample is mounted on to the wave-guide when the VTI has cooled to around 100 K. Insertion of the wave-guide, and with it a significant mass of room temperature metal, warm the VTI, however insertion at around 100 K does not negatively affect the performance of the VTI as it cools down to the base temperature.

Before the sample is lowered into the VTI it is flash frozen with liquid nitrogen. This rapid freezing stops any out-gassing of the sample when it first experiences the cryogenic, low pressure, environment.

5.7.3 Sample polarisation and dissolution

As soon as the sample is below 2 K, the microwave system can be enabled and polarisation started. It is then just a case of waiting until the desired polarisation has been accrued. As will be discussed in following sections, the saturation of carbon DNP occurs after around 2.5 hours. In spin labelled molecules, the decreased inter-spin distance is reduced, increasing the rate of spin diffusion. This means that for labelled chemicals the time required to get maximal polarisation is reduced to around 1 hour, this allows more trials to be performed on the same experiment day.

Before sample dissolution, the solvent is inserted into the heated line for 105 seconds before the dissolution procedure is triggered. Prior to moving the sample attached to the wave-guide, warm helium gas is delivered into the VTI bore through the valve on the airlock up to a pressure of 1200 mbar. This serves two purposes: Firstly it keeps the bore at an overpressure to the surrounding lab to avoid any in-leakage of air; also removing the bore vacuum also reduces the amount of liquid that will enter the VTI bore if there is imperfect docking of the wave-guide with the dock. For experiments in the Bruker BBI or TBO probes, the rocket and NMR tube are evacuated 15 seconds prior to the opening of the Takasago valves.

5.8 Analysis of sodium acetate through Dissolution DNP

Initial testing of the dissolution system was performed with samples of $[1\text{-}^{13}\text{C}]$ sodium acetate. Figure 5.26 shows the chemical structure of the molecule. There are two carbons on the molecule: carbon 1 is a carbonyl and carbon 2 is in a methyl group.

O

C^1

H_3C^2 O$^\ominus$ Na$^\oplus$
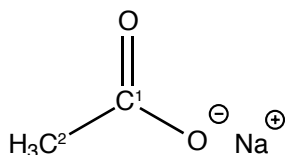
Figure 5.26: Chemical structure of sodium acetate

5.8.1   Solid-state analysis

Initially, solid-state polarisation tests were performed at cryogenic temperatures in the 3.35 T upper iso-centre. A 200 μL sample was made that contained 1 M [1-^{13}C] sodium acetate with 15 mM Trityl (OX63) in approx. 50/50 (by mass) water glycerol mixture. A 50 μL aliquot of this sample was placed in a static solid-state NMR coil tuned to 35.86 MHz, as described in section 5.5.5. The sample was cooled to approximately 1.75 K. Once the temperature was stabilised a microwave sweep experiment was performed for frequencies from 93.65 GHz to 94.15 GHz with frequency steps of 0.01 GHz. At the beginning of each acquisition, the ^{13}C magnetisation of the sample was saturated with a train of 800 small flip angle pulses prior to 120 s of DNP build up. After this time a 90° pulse was used to acquire the solid-state FID. The 2048 complex points of the FID were then zero-filled up to 8192 and apodised with a 2000 Hz exponential decay window function prior to Fourier transformation. On completion of the microwave sweep, the sample was left at around 1.75 K for five hours. The T_1 of the sodium acetate carbonyl carbon below 2 K should be on the order of two and half hours [89], so it would not be possible to wait for the full relaxation time required to develop full thermal polarisation. Five hours was chosen as a compromise such that the experiment could be performed on the same day as the DNP experiments.

Figure 5.27:TOP shows the enhancement of sodium acetate as a function of microwave frequency. To find this value the sodium acetate peak was integrated over a constant range for each microwave frequency. The central frequency (93.9 GHz)
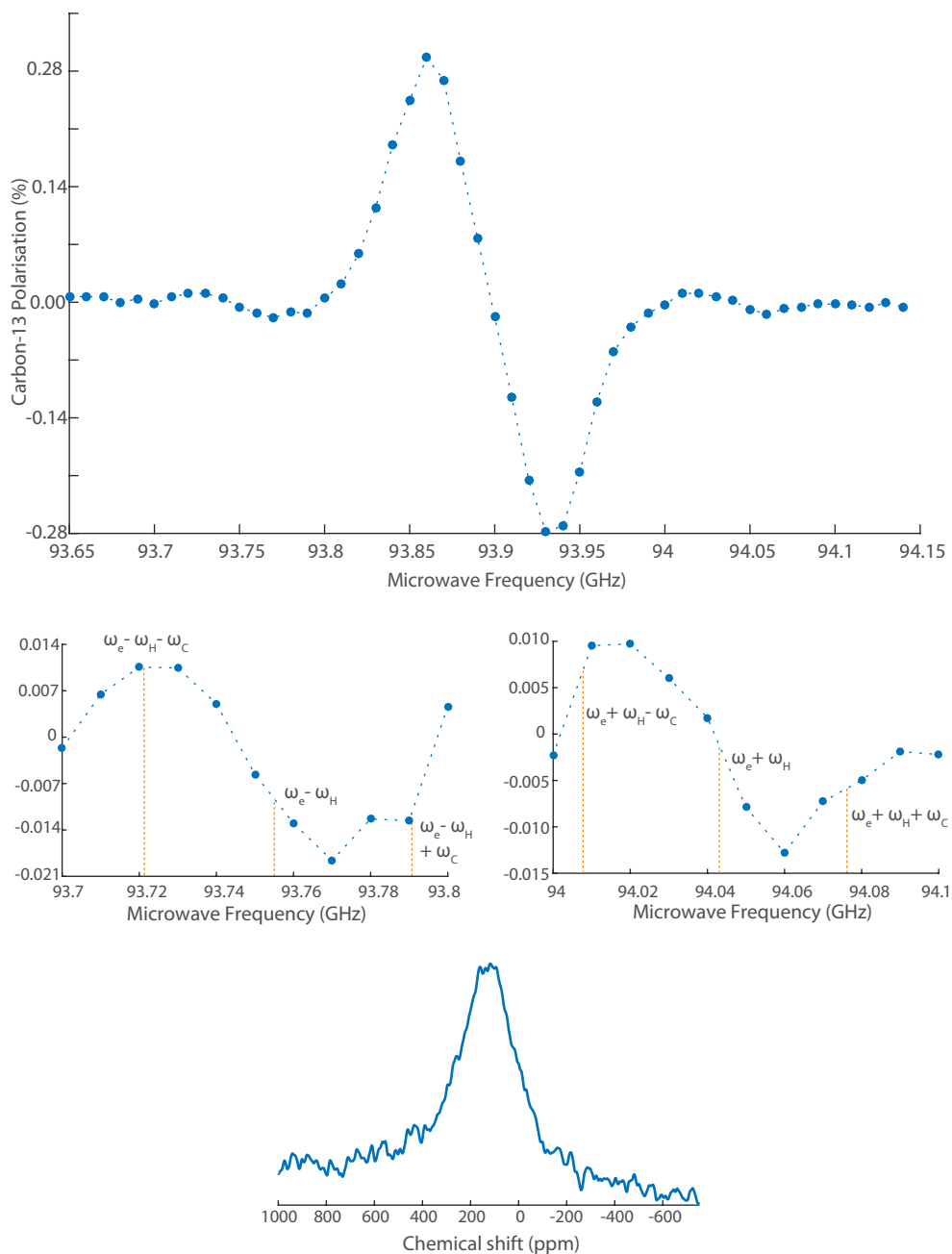
Figure 5.27: TOP: DNP sweep of [1-^{13}C] sodium acetate. The intensity of the signal after 120 s of DNP is plotted against the microwave irradiation frequency. MIDDLE: Enlarged in views of the higher order polarisation effects with indications of the points of frequency combinations. BOTTOM: Thermal sodium acetate spectrum at 1.75 K. Offset of the spectrum is due to carbon present in the surrounding structure of the probe.

Parameter	Value
Saturation Pulses	
Number of pulses	800
Power	6 W
Duration	2 μS
DNP build up	120 s
FID acquisition	
Power	20 W
Duration	18 μS
Number of points	2048
Acquisition duration	14 ms
Spectral Width	1992 ppm

Table 5.1: Sodium acetate microwave sweep parameters

is the electron resonant frequency in the upper iso-centre. The peak and trough frequencies are 93.86 GHz and 93.93 GHz respectively. The separation of the peak and trough is 70.4 MHz, this value agrees approximately with the Solid Effect condition for polarisation:

$$\omega_{\text{mw}} = \omega_{\text{e}} \pm \omega_{\text{C}}. \tag{5.2}$$

There are additional regions of enhancement outside the normal enhancement curve. A small amount of enhancement is observed around 93.72 GHz and 94.06 GHz. These regions of enhanced carbon polarisation cannot be explained by the simple SE/CE model and as such a 'higher order' explanation is required. Using the radical Trityl, protons demonstrate distinct Solid Effect polarisation. At 3.35 T, the lobes of the proton polarisation enhancement will be situated around ± 142 MHz from the electron resonance. In the system examined here that would relate to frequencies of 93.757 GHz and 94.043 GHz. At these frequencies, the sodium acetate hydrogen atoms would dynamically accrue polarisation taking them away from the their thermal equilibrium. This could encourage cross relaxation between the nuclear spins. However, the picture of cross relaxing proton and carbon spins would not account for the microwave frequency dependence of this additional po-

larisation effect. By zooming in to these regions on the sweep curve, secondary positive and negative lobes can be seen.

$$\omega_{\mathrm{mw}} = \omega_{\mathrm{e}} \pm \omega_{\mathrm{H}} \pm \omega_{\mathrm{C}} \tag{5.3}$$
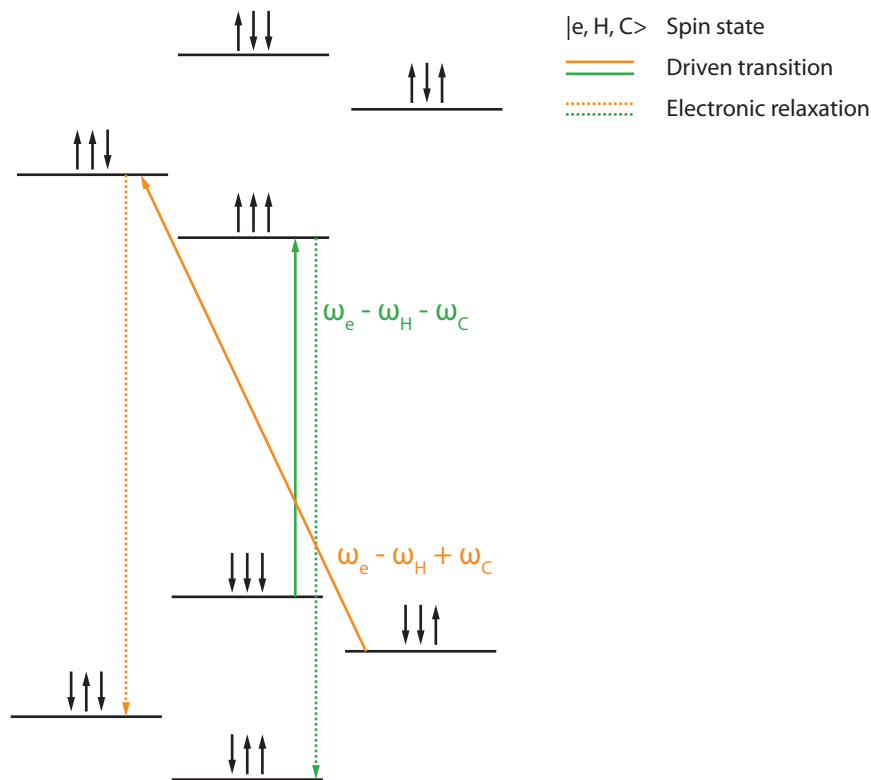
Figure 5.28: Polarisation effect involving two nuclear spins and an electron. The additional lobes of polarisation observed in the DNP sweep profile could be explained through a higher order polarisation transfer process. In this case, a solid effect type process polarises the surrounding protons, then cross relaxation between the protons and the carbons enhances the carbon spin polarisation.

A three spin system involving an electron, a hydrogen and a carbon could be used to explain the shape of the additional polarisation curves. In such a system there would be eight non-degenerate energy states. Figure 5.28 demonstrates the arrangement of energy levels in this model. In this system, microwave frequencies that satisfy equation 5.3 drive transitions that directly polarise the carbon spins. The locations of the positive and negative enhancements on both sides of the sweep

curve support such a model. These are shown in the smaller panels of figure 5.27. The peaks and troughs are subtly shifted from their calculated positions, however this triple spin effect provides a reasonable explanation of the observed results. Similar results were obtained by Shimon and co-workers in [90]. They used similar experimental parameters to observe higher order heteronuclear DNP in ^{13}C-glycerol. They account the additional effects to a heteronuclear Cross effect mechanism with a resonance condition

$$|\omega_\mathrm{a} - \omega_\mathrm{b}| = |\omega_\mathrm{H} \pm \omega_\mathrm{C}|, \tag{5.4}$$

where $\omega_\mathrm{a,b}$ are the Larmor frequencies of two electrons a and b.

5.8.2 Polarisation build up analysis

Experiments were also performed to observe the build up of ^{13}C polarisation as a function of time. As the name suggests DNP is a dynamic process, the build up of nuclear polarisation is constantly being sapped by the intrinsic relaxation mechanisms. There is a characteristic build up time, τ_DNP, which is defined as the time constant for the exponential build up of nuclear polarisation. Determining this time in the solid state is required to optimise the dissolution experiment for maximal enhancement.

To test the build up, another sample of 1 M [1-^{13}C] sodium acetate was taken cooled to approximately 1.75 K. The microwaves were set to a constant frequency at the peak of the sweep (93.86 GHz). The most precise way to measure the polarisation build up it saturate the initial magnetisation before waiting for a polarisation time and then acquiring a spectrum. This process is then repeated for the durations. However, as the build up times for DNP samples is on the order of hours, this method quickly become infeasibly long with only a small number of acquisition points. Instead smaller flip angle pulses were used so that they had a negligible effect on the dynamics of the system. This allowed a detailed analysis of the build

up as a function of time. Figure 5.29 shows the DNP build up for four different microwave attenuations. By fitting these curves with the equation

$$S(t) = S_{max} \cdot (1 - \exp(\frac{-t}{\tau_{DNP}})), \tag{5.5}$$

it is possible to extract the build up parameter. Here S_{max} is the maximal signal that can be generated at long polarisation times. One feature of note in figure 5.29 is shape of the DNP build-up at 12 dB microwave attenuation. This was the first build-up curve acquired on the experiment day. While the sample space relatively quickly reaches a temperature of around 1.9 K, it takes around an hour for the rest of the VTI to cool enough to allow temperatures close to 1.7 K. This first trial shows the DNP dependence on sample temperature.

Figure 5.29 also shows the relaxation of the hyperpolarised solid state spectrum as a function of time. This involved polarising a sodium acetate sample for around two hours whilst monitoring DNP build up as above. After the polarisation, the microwaves were turned off but the experiment continued. Throughout the experiment the sample remained at a base temperature of around 1.7 K. This decay was then fitted with an exponential decay function to extract the low temperature T_1 time. This time was 131 minutes, longer than previously thought.

5.8.3 Sodium acetate dissolution tests

Experiments in the solid state show that DNP successfully transfers polarisation from the Trityl free-radical onto the ^{13}C carbonyl spins on sodium acetate. This means that dissolution experiments can be performed to take advantage of both the DNP enhancement and the effects of the rapid temperature jump.

Dissolution tests were performed again with a 1 M [1-^{13}C] in 50:50 (by mass) water glycerol mixture. The radical was 15 mM Trityl. Figure 5.32 shows the DNP en-
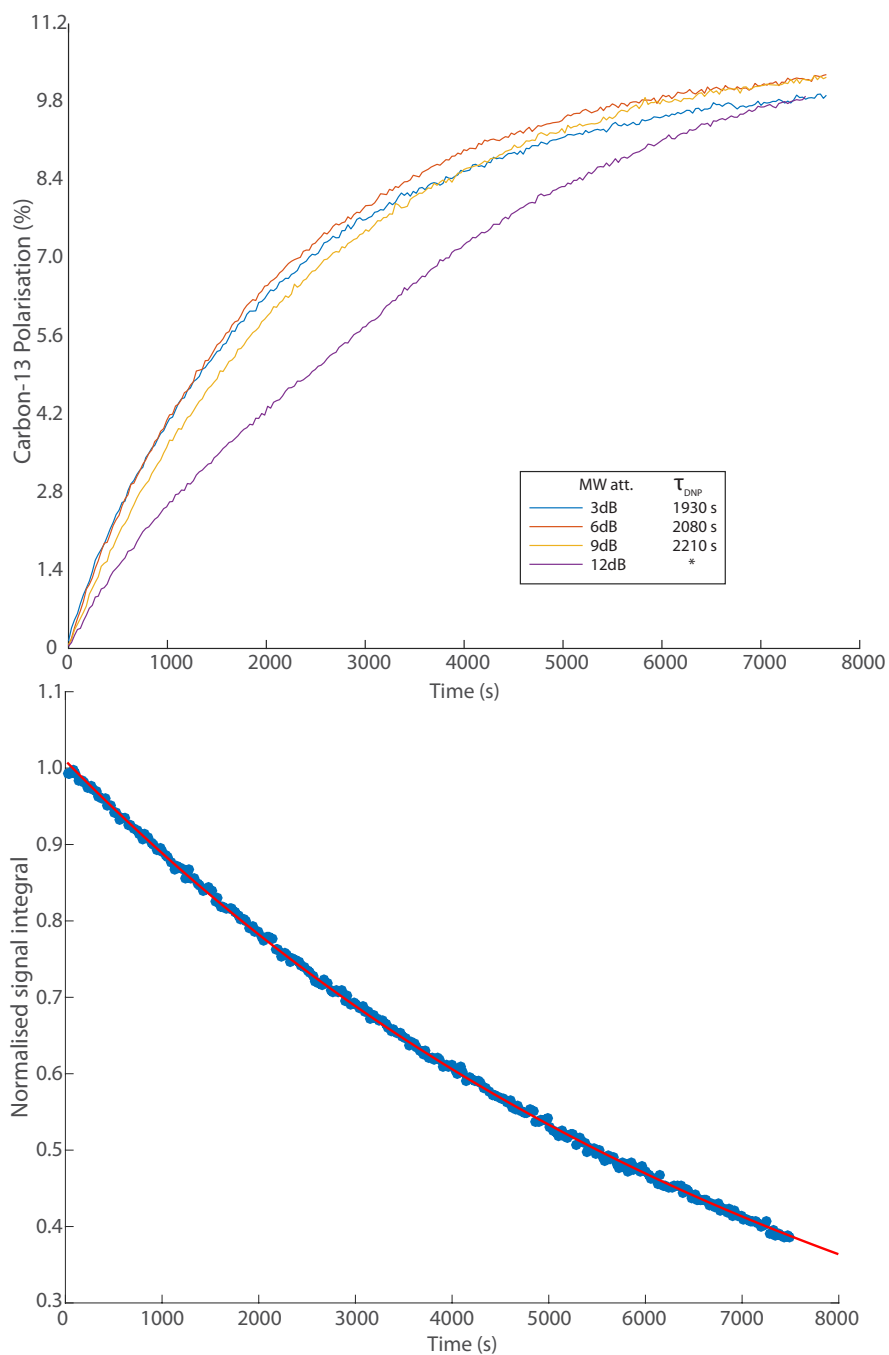
Figure 5.29: TOP: Build-up of ^{13}C carbon DNP signals on [1-^{13}C] sodium acetate at different microwave attenuations. The build up times for the different microwave powers. BOTTOM: Decrease of hyperpolarised signal after switching off the microwaves due to relaxation. This data was fitted with a mono-exponential decay to extract a T_1 relaxation time of 131 minutes.

hanced spectrum of following sample dissolution. Here the sample was polarised for one hour at a temperature of around 1.9 K. A pulse with approximately an $\approx 80°$ rotation angle applied to the sample after a settling time of 300 ms, this was followed with a train of small pulses ($\approx 5°$). All FIDs were composed of 16k complex points over an acquisition time of 255 ms. For the pulse train an inter-scan delay of 250 ms separated the pulses. The FIDs were then zero-filled up to 32k points and apodised with 5 Hz exponential decay window.

Figure 5.32 shows the first scan of the dissolution. The carbonyl is visible at around 182 ppm with a signal to noise ratio of 1312. Also visible are the two sets of multiplets from the natural abundance glycerol carbons. The inset shows these peaks magnified 20 times. The natural abundance methyl carbon of the sodium acetate is not observed. Figure 5.33 shows the evolution of the carbonyl peak following the big pulse. The data has been fitted with a double exponential to extract T_1 information as well as other dynamics. This fit takes the following form:

$$f(t) = (2.15 \pm 0.10) \times \exp\left(-\frac{t}{46 \pm 1s}\right) - (1.17 \pm 0.10) \times \exp\left(-\frac{t}{32 \pm 1s}\right).$$
$$(5.6)$$

The first exponential gives an indication of the nuclear relaxation processes. A decay constant of around 46 s is consistent with the T_1 relaxation times observed in sodium acetate carbonyl carbons. However, the necessity of the second exponential function indicates that there are further dynamics happening within the sample. These dynamics are most probably motion within the sample. As the NMR tube fills higher than the coil, the mixing of liquid that has not been observed with previous scans could provide additional NMR signal. This effect, to varying extents, is observed in all time resolved decays following dissolution. The residuals plot of figure 5.33 shows that this double exponential model only deviates from the data by up to 2%.
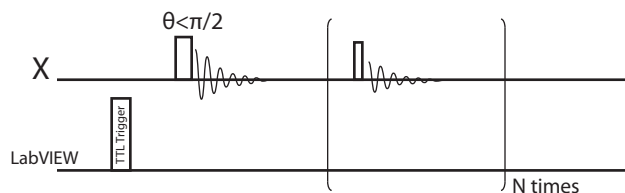
Figure 5.30: Pulse program used for dissolution trials. During the dissolution the LabVIEW control computer sends a TTL trigger to the spectrometer console to begin the pulse program. This is followed by a 'big' pulse which is on the order of, but less than, 90°. This is used take a complete spectrum with signal-to-noise large enough to assign all peaks on the spectrum. The big pulse is then followed by a train of small pulses of less than 5°. This provides additional information about the decay of the signal following dissolution, information such as the nuclear relaxation time constant T_1.
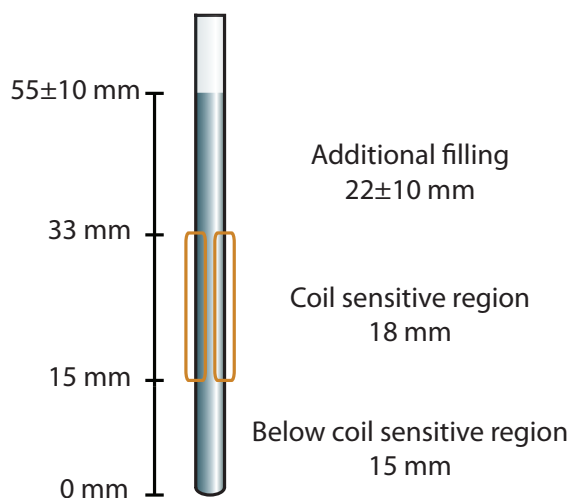
Figure 5.31: Length of the NMR which is filled following dissolution. Over 20 dissolution trials, the level of filling was monitored. There are three distinct regions in the NMR probe, the area below the coil, the coil's sensitive region and the area above the coil. The dissolution consistently fills above the coil however the level that it reaches is still quite variable. This variation will play a part in the inconsistencies around sample concentration, observed NMR signal and signal line width. Fluid motion within the sample tube could also be one explanation for the double exponential decay of the enhanced NMR signal following dissolution.
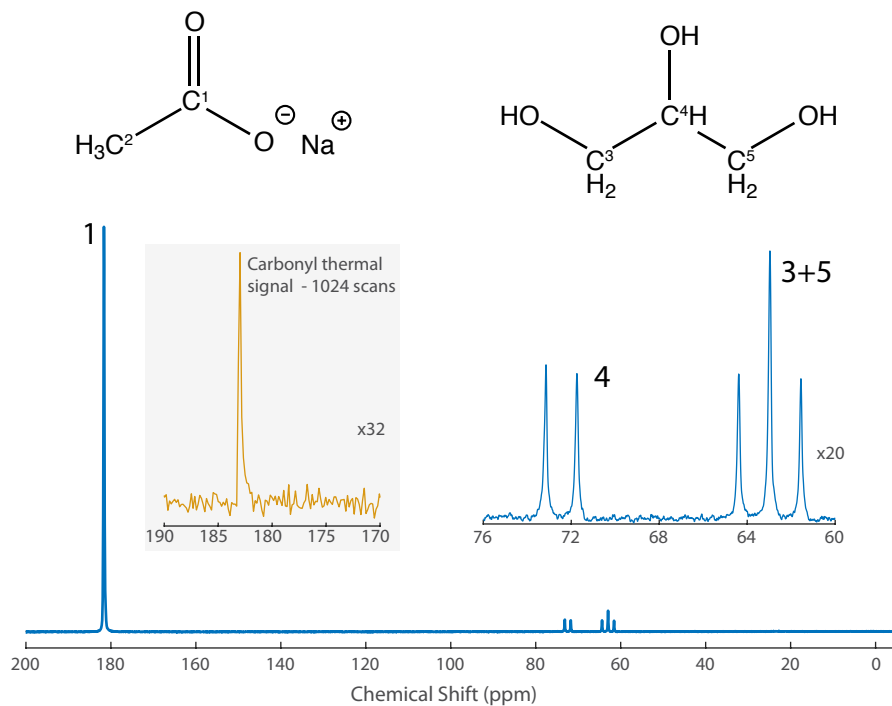
Figure 5.32: Hyperpolarised ^{13}C spectrum of [1—^{13}C] sodium acetate. The labelled peak is observed on the sodium acetate, however the methyl is not. In the chemical shift range of 60 to 76 ppm the doublet and triplet peaks of the natural abundance glycerol are observed.

Peak	Chemical Shift (ppm)	Enhancement	Line width (Hz)
Sodium acetate			
1	182.3	6100	25.4
Glycerol			
1	174.1	4570	13.5
2	50.1	3910	14.1

Table 5.2: Results of sodium acetate dissolution
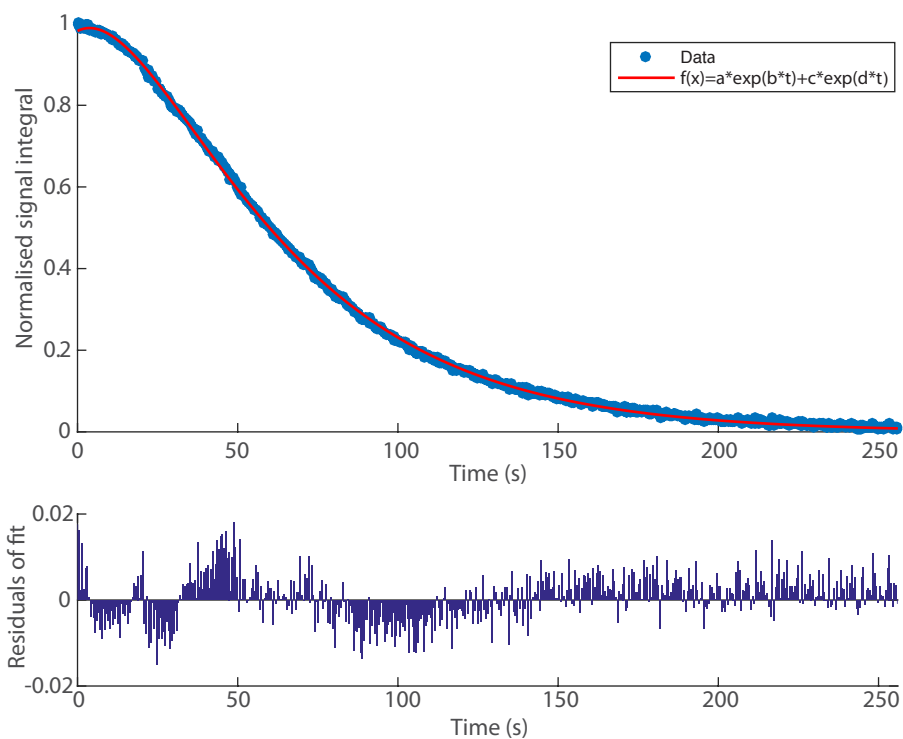
Figure 5.33: TOP: Time course of sodium acetate carbonyl integral following DNP enhanced dissolution. The decay of the signal should be a mono-exponential fit that follows the T_1 relaxation of the nuclear polarisation and the effect of the pulses, however there is an additional exponential with a slower relaxation constant, as shown in equation 5.6. The cause of this extra function is not clear, however it is possible that liquid motion in the sample is causing additional hyperpolarised material to move in and out of the coil's sensitive region. BOTTOM: The residuals of the oscillate in time, indicating that there are additional higher-order processes occurring within the sample during NMR acquisition.

5.9 Analysing Urea through Dissolution DNP

Urea was used to test the dissolution set-up in conjunction with ^{15}N NMR spectroscopy.
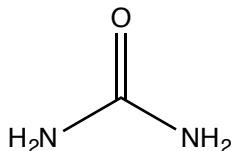
Figure 5.34: Chemical structure of Urea

5.9.1 Dissolution solvent

Initial testing of the dissolution system with Urea involved D_2O as the heated solvent, this was used to ensure the longest possible T1 relaxation of the urea during the dissolution tests. However, this introduced the issue that the deuterium atoms exchange readily with amine protons of the Urea molecule. A dynamic equilibrium will form with all possible combinations of hydrogen and Deuterium attached to the amine nitrogen. The relative amounts of each conformation will be determined by the relative amounts of hydrogen and Deuterium in the sample. The rate of this exchange is temperature and pH dependent [91], with saturation of exchange happening within tens or hundreds of milliseconds. Figure 5.35 shows the ^{15}N spectra obtained from Urea dissolved in D_2O. The top spectrum shows a complex multiplet structure. And the bottom spectrum shows the equivalent data from a sample that contains no deuterium.

The ^{1}J heteronuclear coupling between the ^{15}N and the Deuterium is around 13 Hz compared to purely protonated case where the coupling is about 90 Hz.

To determine the ability of the system to polarise and observe ^{15}N signals, the experiments performed in section 5.8 were repeated with ^{15}N labelled Urea. A second solid state coil was made that was tuned to around 14.5 MHz. A 200 μL sample
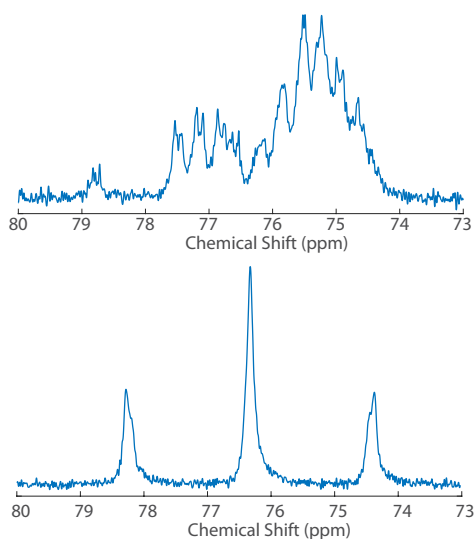
Figure 5.35: TOP: Urea in H_2O+D_2O. The proton-deuteron exchange creates a number of different configurations with 0, 1, 2, 3 or 4 protons. Each configuration will produce an individual pattern of multiplet peaks in the NMR spectrum. BOTTOM: Urea in pure H_2O. In this case there is only one configuration of urea with 4 protons, producing a much simplified spectrum based on j-coupling with these attached protons.

was made containing 2 M ^{15}N Urea in a 50:50 (by mass) water glycerol mixture with 15 mM Trityl. As before, a 50 μL aliquot was placed inside the ^{15}N solid state coil. A microwave sweep was performed between 93.7 GHz and 94.1 GHz with microwave steps of 5 MHz. Figure 5.36 shows the nuclear enhancement as a function of microwave frequency. These experiments were performed at slightly higher temperature of around 1.9 K

The Urea sweep curve presented in figure 5.36 shares characteristics with the equivalent carbon curve show previously. The main peak and trough of the sweep are in at very similar frequencies to those observed in the sodium acetate sample. The polarisation similarities of carbon and nitrogen have been discussed previously by Day and co-workers [85]. The overlapping of the sweep curve allows the polarisation of both spin species simultaneously. The concept of double nucleus DNP is explored further in the next chapter. The higher order effects observed on the DNP

sweep of sodium acetate also appear here, however they are not as prominent.
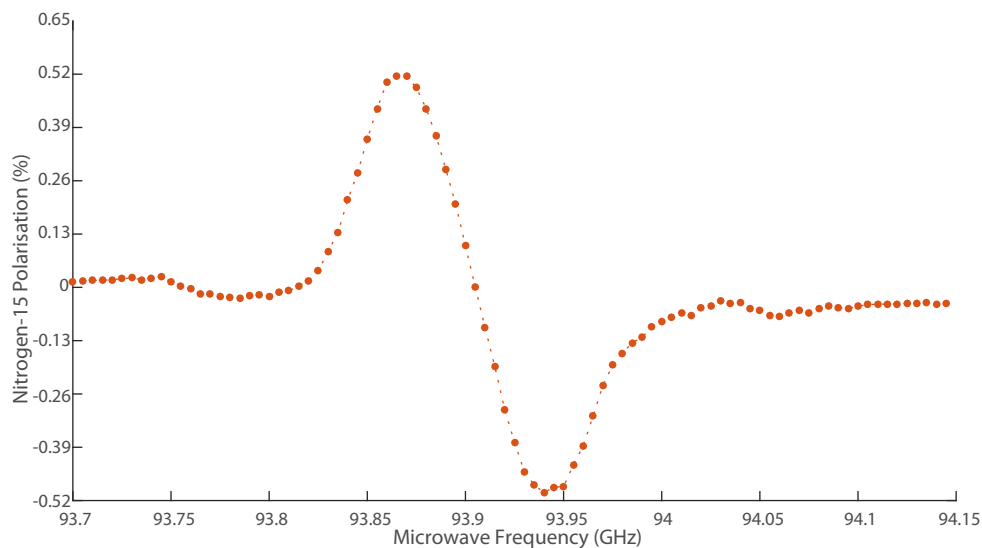
Figure 5.36: DNP profile of Urea in 1:1 water glycerol and 15 mM Trityl. Polarisation was killed via a train of 800 ≈ 3° pulses before 120 s of DNP build up at around 1.9 K. Following this an ≈ 80° pulse was used to obtain a solid state FID. This FID was then Fourier transformed and integrated. This integral was compared to a thermally polarised spectrum from the same temperature and then converted to percentage.

Figure 5.37:TOP shows DNP build-up as a function of time for three microwave attenuations. The previous test of carbon DNP build up demonstrated similar values for the saturation level of the polarisation at long times, this is not the case for nitrogen. Here, there is a significant increase in polarisation at the lower microwave power. One possible explanation is microwave heating within the sample. Microwave heating is widely reported in DNP literature [92, 93, 4, 94]. While it is clear that energy is deposited on the sample via the microwave irradiation, it is not so obvious as to what causes thermal coupling between the irradiation and the lattice. The rotational modes that normally mediate dielectric heating should be "frozen out" at cryogenic temperatures.

The lower graph in figure 5.37 shows the decay of hyperpolarised nitrogen sig-

nal. This was acquired in the same was as the equivalent carbon signal. The T_1 relaxation time of urea in the solid state, under these experimental conditions is 59 minutes.

5.9.2 Urea dissolution tests

Further aliquots of the sample tested for solid state analysis were used to test the acquisition of Urea signals from dissolution DNP experiments. Here, $20\mu L$ of urea sample was placed in the dissolution cup. Figure 5.38 shows results from one such dissolution. In this case the heated solvent was D_2O, hence there are a number of peaks for both deuterated and partially deuterated urea. This data acquisition was not triggered by the LabVIEW control program, rather acquisition was started shortly before dissolution. This was due to a temporary communication error between the LabVIEW VI and the spectrometer console. Panel a) of the figure shows the time course of spectra during the experiment. No nitrogen reference was used in this experiment so the chemical shift on panel b) is calibrated to the higher concentration urea data in figure 5.35.

The initial aliquot that was loaded into the sample cup was prepared with H_2O. The first liquid-state spectrum observed following the dissolution shows the multiplet pattern of deuterated urea. This means that the deurteration process is complete before NMR acquisition begins.

The nitrogen spins of the deuterated and partially deuterated urea molecules display different relaxation times. By fitting mono-exponential decays to each, the T_1s were found to be 144 ± 0.5 s for the deuterated spins and 128 ± 2 s for the partially deuterated spins. These fits, along with the measured integrals are shown in panel d).

Figure 5.39 shows another set of dissolutions. This time using demineralised water as heated solvent. As expected, this data does not demonstrate the additional mul-
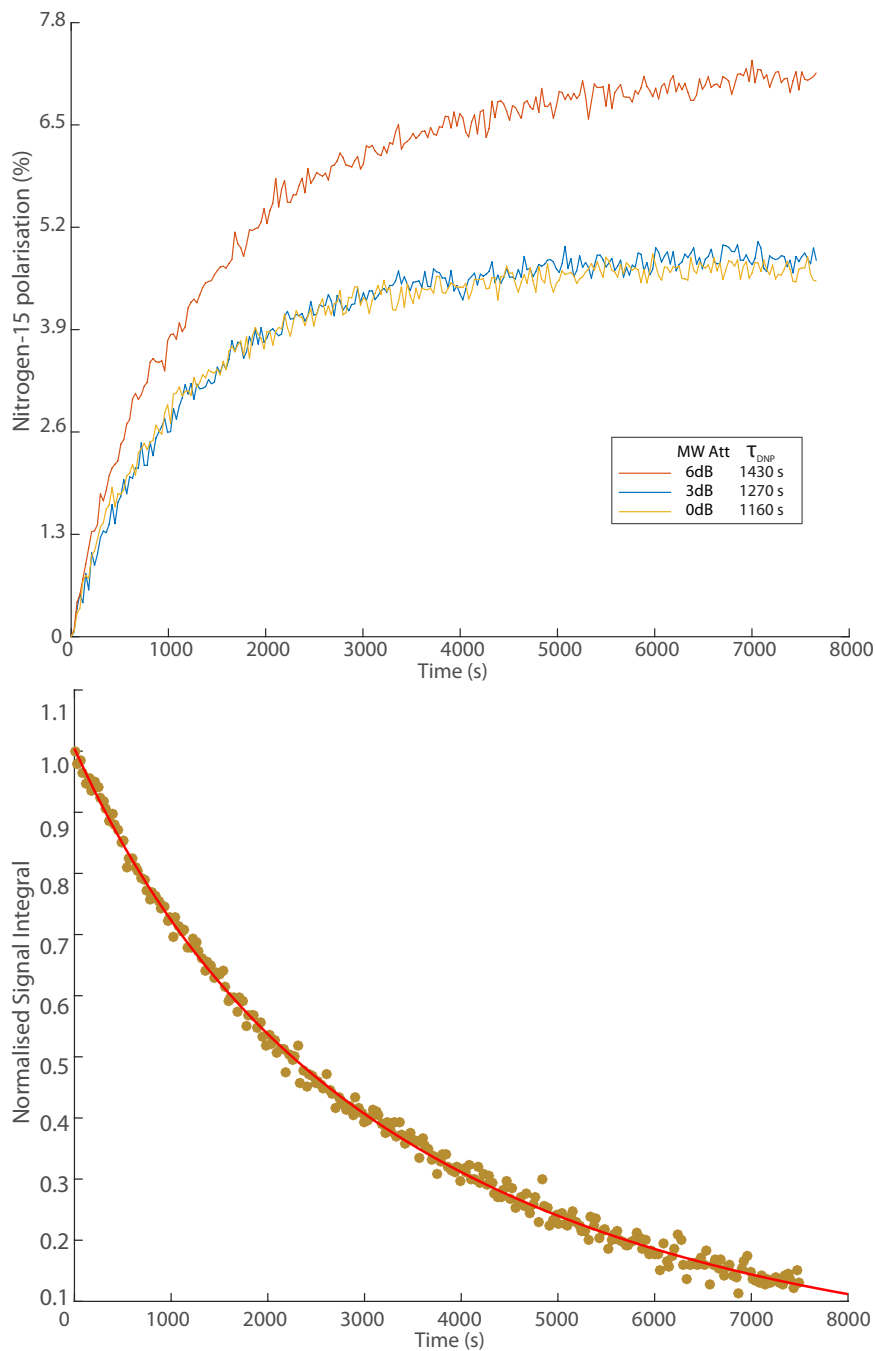
Figure 5.37: Build up and decay of hyperpolarised Urea. TOP: DNP build up dynamics for a range of microwave powers. Spectral integrals for each acquisition were compared with a thermally acquired equivalent to find the enhancement factor, this was then converted into a percentage polarisation. A substantial increase in nuclear polarisation is observed for lower microwave powers. BOTTOM: The decay of hyperpolarised urea shows the T_1 relaxation of the molecule.
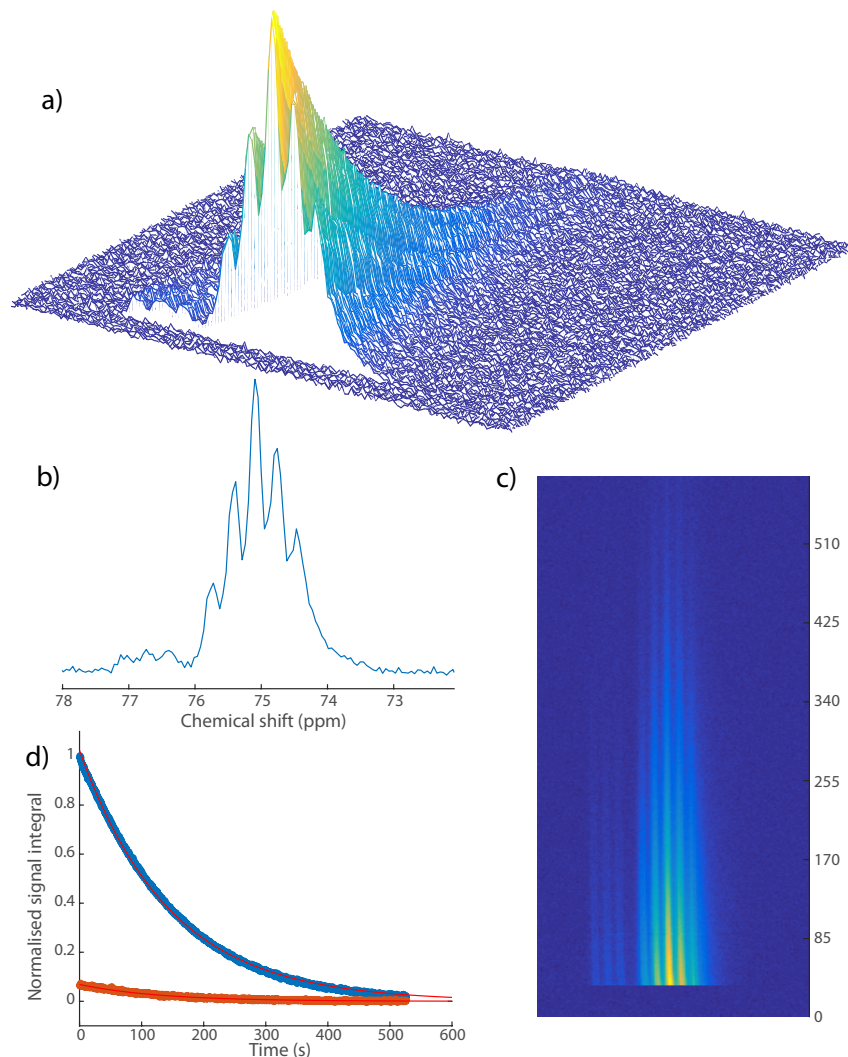
Figure 5.38: *Analysis of urea with dissolution DNP using D_2O as solvent. a) Time series of spectra following sample dissolution. b) First spectrum taken from a) D_2O was used as the heated solvent, this causes splitting of the resonance lines into a number of multiplets. c) Observed signal decay of the multiplet peaks. d) The small peaks observed between 76 and 77.5 ppm show a small amount of partially deuterated urea, this demonstrates a slightly shorter T_1 time from the main set of peaks. Here the integrals of each set of multiplets are shows as function of time from NMR tube filling.*

tiplets observed previously. In water, the urea sample shows a significantly shorter T_1 relaxation time of 38 ± 1 s. This sample was only polarised for around 30 minutes. Spectra were collected with a train of small flip angle pulses ($\approx 4°$). FIDs were composed of 6k complex points that were zero-filled up to 16k points and apodised with a 3 Hz exponential decay function prior to Fourier transform.
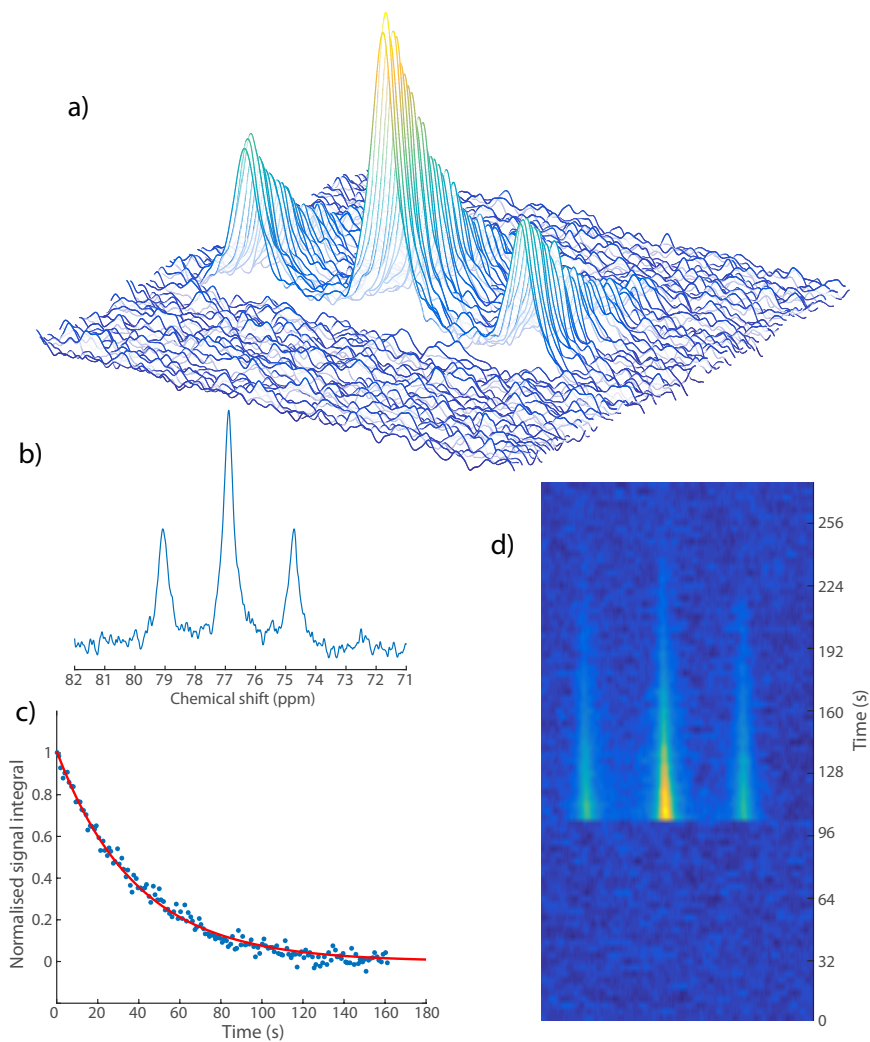
Figure 5.39: *Analysis of urea with dissolution DNP using H_2O as solvent. a) The time course of spectra following dissolution. The ^{15}N spins remain as a protonated triplet with H_2O as the solvent. b) First acquired spectrum. c) Decay of signal integral gives a T_1 relaxation time of 38 ± 1 s, which is significantly shorter than the deuterated case presented above.*

5.10 Conclusion

The Dissolution-DNP spectrometer has been modified to increase both the speed of dissolution and the reliability of the process. The ability to deliver hyperpolarised liquid to the NMR probe in around 300 ms makes it possibly the fastest dissolution system in the world. However, a number of compromises have been made in order to allow this increased speed. The VTI needs to be open at both ends to allow mechanical shuttling of the sample between DNP stages, this means that the design of the cryostat is not optimised for low temperatures. The lowest temperature observed in this system is around 1.65 K, other DNP systems are capable of lower temperatures on the order of 1.2 K or lower [60, 95]. The increased temperature will limit the solid-state polarisation that can be achieved in this system.

The dissolution system has been simplified to increase its speed and reliability. Solvent can now be delivered so that it maintains its temperature until it makes contact with the frozen sample, increasing the efficiency of melting. A further development of this would be to send the heated solvent right up to the inlet of the dock prior to the dissolution process. This method was not enacted as the limited space on the dock would not allow the additional valve and air line to be included. However, the dissolution process has, over time, been made reliable. With correct operation, the system will produce a hyperpolarised sample with a success rate of around 80%.

There are still questions regarding the efficacy of the microwave system as the observed power should be more consistent over the frequency range, further analysis into the amount of microwave power being deposited onto the sample could lead to significant gains in polarisation level.

In general the system is now in the state where its application to more advanced molecular testing can be considered.

6

Simultaneous Polarisation of Multiple Nuclei with DNP

If your experiment needs statistics, you ought to have done a better experiment

– Ernest Rutherford

6.1 Introduction

The power of NMR to characterise molecules of interest is vastly expanded with the ability to observe multiple nuclei. Gathering data from different sets of 'molecular spies' allows one to build a more complete picture of the sample being studied. In efforts to increase the information extracted from a dissolution-DNP experiments, observing multiple nuclei is a logical path to follow. However, attempts to combine hyperpolarisation and multi-nuclear NMR acquisition have been limited by available NMR hardware [85].

As was introduced in previous chapters, the transfer of electronic spin polarisation in the solid state is characterised by the microwave sweep curve. Each nucleus on each molecule will have its own individual DNP frequency response profile, but it has been acknowledged in the previous chapter that ^{13}C & ^{15}N spins demon-

strate microwave profiles that overlap significantly. In such a case, both nuclei are polarised by DNP without changing any experimental parameters. This presents the most straight forward system for developing multi-nuclear DNP experiments as only the liquid-state probe hardware and pulse sequences need to be modified. This chapter looks at the initial development of multi-nuclear DNP with carbon and nitrogen spins first using spin labelled molecules and then molecules with natural abundance isotopes.

6.2   Hardware for Multi-nuclear dissolution-DNP

The acquisition of NMR data from multiple separate channels is becoming a standard procedure to increase the data extraction rate of NMR experiments. Parallel acquisition NMR spectroscopy (PANSY) is a technique that records NMR data simultaneously across separate receiver channels. This has allowed multidimensional correlations to be observed from multiple different nuclei simultaneously, resulting in a decreased experiment time [96]. This is advantageous for thermally polarised NMR when experiments are often long and time on the equipment is at a premium. This technique has been extended into Parallel acquisition NMR, an all-in-one combination of experimental applications (PANACEA) which is able to provide 1D spectra as well as 2D and 3D correlation information across a single experiment [97].

Procedures such as those outlined above have not yet been translated into the hyperpolarised NMR community. And in general, the simultaneous analysis of multiple nuclei through dissolution-DNPhas been limited by the hardware available. As previously introduced the spectrometer console available in Nottingham includes six independent acquisition channels. Hence the limiting factor for liquid state experiments is the NMR probe. The dual iso-centre system has been specifically designed to allow the use of any commercial 400 MHz (^{1}H) probe. For the experiments performed in this chapter a Bruker Triple resonance Broadband Ob-

serve (TBO) probe was used. This probe has two saddle coils for Tx/Rx of RF signals. The inner coil is a broadband coil designed for the detection of nuclei from ^{15}N to ^{31}P[1]. The outer coil is triple tuned to ^{1}H, D and ^{13}C. By design, the outer coil is designated for the decoupling of spins connected to the nucleus of interest, which would then be observed through the inner coil. For the purpose of this project, both the inner and outer coils were used for observation of nuclei (^{13}C and ^{15}N). The outer coil was also used for proton decoupling. While using the outer coil for NMR detection provides additional information from the dissolution experiment, it also has a inherent problem: As the coil is larger and further away from the sample the filling factor, and therefore sensitivity, of the coil is significantly lower, around 3.5 times less sensitive then using the inner coil.

6.2.1 Double nucleus detection with proton decoupling

The use of proton decoupling is important to the study of biologically relevant chemicals. By comparing spectra with and without decoupling it is possible to gain insights into the distribution of proton spins on the molecule of interest and assign peaks correctly. It also has an effect on the sensitivity as the integrals of the multiplets will combine in the individual decoupled peak. By developing a pulse sequence that incorporates proton decoupling for multi-nuclear dissolution DNP experiments, the sensitivity of the experiment can be further enhanced. Figure 6.1 shows the pulse sequence that was used for this project.

Many decoupling schemes include an extra decoupling pulse on the proton channel prior to FID acquisition. This extra pulse exploits the Nuclear Overhauser Effect (NOE) to enhance the observed spectrum. NOE enhances the observed NMR signal by

---

[1] This includes any nucleus with between 40 MHz and 162 MHz at a field strength of 9.4 T
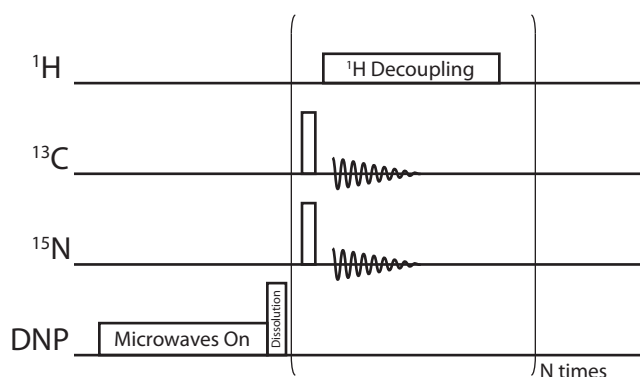
Figure 6.1: Pulse sequence for double acquisition with proton decoupling. In this sequence a train of N pulses follows the sample dissolution. This pulses can be small to allow an analysis of dynamics such T_1 relaxation or chemical exchange, or they can be large to observe a spectrum arising from the full magnetisation.

6.3   Analysis of [1-^{13}C] Sodium Acetate and ^{15}N Urea by multi-nuclear dissolution DNP

Initially, to determine the effectiveness of multi-nuclear DNP, dissolution tests were carried out with samples that contained both [1-^{13}C] Sodium Acetate and ^{15}N Urea. These molecules are both highly soluble and unreactive, so stably provide both carbon and nitrogen spins in the absence of doubly labelled compounds.

A 3 M [1-^{13}C] Sodium Acetate, 2 M ^{15}N Urea sample was dissolved in approx. 50:50 (by mass) water/glycerol. The radical was 15 mM of Trityl (OX63). A 20μL aliquot of this sample was polarised for around 50 minutes with microwaves at a frequency of 93.86 GHz. The sample temperature was held at about 1.7 K for the duration of polarisation. Following the dissolution, a train of small flip angle pulses was recorded (approx. 0.5° for carbon and 1° for nitrogen) in the presence of WALTZ-16 proton decoupling. Decoupling power was 3 W. The complete experimental parameters are included in table 6.1 and the results are shown in figure 6.2[2].

---

[2]The spectral width of the carbon detection was not sufficiently large to include either the Sodium Acetate methyl carbon or glycerol peaks.

The separate sweep curves presented in the previous chapter suggest that the microwave frequency that provides optimum DNP enhancement for both the Sodium Acetate and the Urea samples coincide at 93.86 GHz. This means that the enhancement of each spin species should be similar. A dual tuned solid state coil would be required to monitor the respective polarisation build ups of the nuclear spins. However, a measure of the relative polarisations can be estimated through a comparison of the enhancement of the liquid state spectra. A ratio 'R' can be calculated that corrects for all of the relative acquisition parameter, in initial form of the equation is

$$R = \frac{\epsilon_N}{\epsilon_C} \approx \frac{S_N}{S_C} \cdot \frac{C_C}{C_N} \cdot \frac{N_C}{N_N} \cdot \frac{\sin(\theta_C)}{\sin(\theta_N)}, \tag{6.1}$$

where ϵ_i is the enhancement of the nucleus i, S_i is the liquid-state signal to noise of that spin (which is defined as the ratio of the most intense peak in the spectrum and the noise level calculated from a region of the spectrum that contains no peaks. This region uses around $1/16$ of the total number of points on the spectrum), C_i is the concentration of the molecule, N_i is the number of contributing spins on that molecule (1 for [1-^{13}C]-Sodium Acetate and 2 for ^{15}N-Urea) and θ_i is the flip angle of the pulse applied to the spin.

For this experiment, where there is 3 M of Sodium Acetate and 2 M of Urea, the SNR values obtained produce $R_{SNR} = 0.98$, which suggests that the two spins are indeed polarising to similar levels. A direct comparison of the signal enhancements observed for the two spins gives $R_\epsilon = 0.93$, so both metrics while different, indicate a comparable level of enhancement of both spin species. It is important to note that this equation provides only an estimate of the relative polarisation levels, it does not take into account of other factors such as DNP build up time or relative abundance, however such factors could easily be included if required. The enhancement values of $\epsilon_C = 4870$ and $\epsilon_N = 5230$ are consistent with the values found in dissolution experiments on individual spin species in the experiments

presented in the previous chapter.

Figure 6.2:c shows the integrals of the nitrogen and carbon peaks as a function of time following dissolution. As the pulses are so small, even after 128 scans there is a negligible reduction of z-magnetisation due to the pulses, therefore the decay of the peak integrals over time is purely down to longitudinal relaxation within the sample. By fitting the data with an exponential decay curve, the T_1 of each chemical can be extracted. In this sample the Sodium Acetate carbonyl carbon demonstrated a T_1 of 20.3 ± 0.2 s and the Urea nitrogen T_1 was 34.1 ± 0.3 s. These values are shorter than those obtained in previous experiments. As the concentration of Trityl is consistent between samples, there should not be a difference in paramagnetic relaxation. However the increase in the total solute concentration will change the constituency of the sample. Both Urea and Sodium Acetate solutions do show an increase in liquid viscosity as a function of concentration [98, 99]. Such a change in viscosity would be small for the dissolved sample but could change the correlation time of the molecules. Also, with increased concentrations in the sample there would also be a lower average inter-molecular distance, this would encourage dipole-dipole relaxation pathways.

6.3.1 Sensitivity of the double nucleus DNP

The results presented are based on spin labelled compounds at reasonably high concentration. By starting with 3 M of [1-^{13}C]-Sodium Acetate and 2 M ^{15}N-Urea means that the final sample contains a significant number of observable carbon and nitrogen spins, on the order of 75 mM of Sodium Acetate and 50mM Urea. For the labelled Urea, the first spectrum has a SNR of 346. Therefore an equivalent experiment at natural abundance should provide SNR of about 1.2. This can easily be improved by increasing the the flip angle of the pulse. Going from 1° used above to 90° would increase the SNR to 68 at the sacrifice of information on the dynamics. Urea has the advantage of having two magnetically equivalent nitrogen spins, doubling the observed signal. But even inequivalent nitrogen spins at 2 M
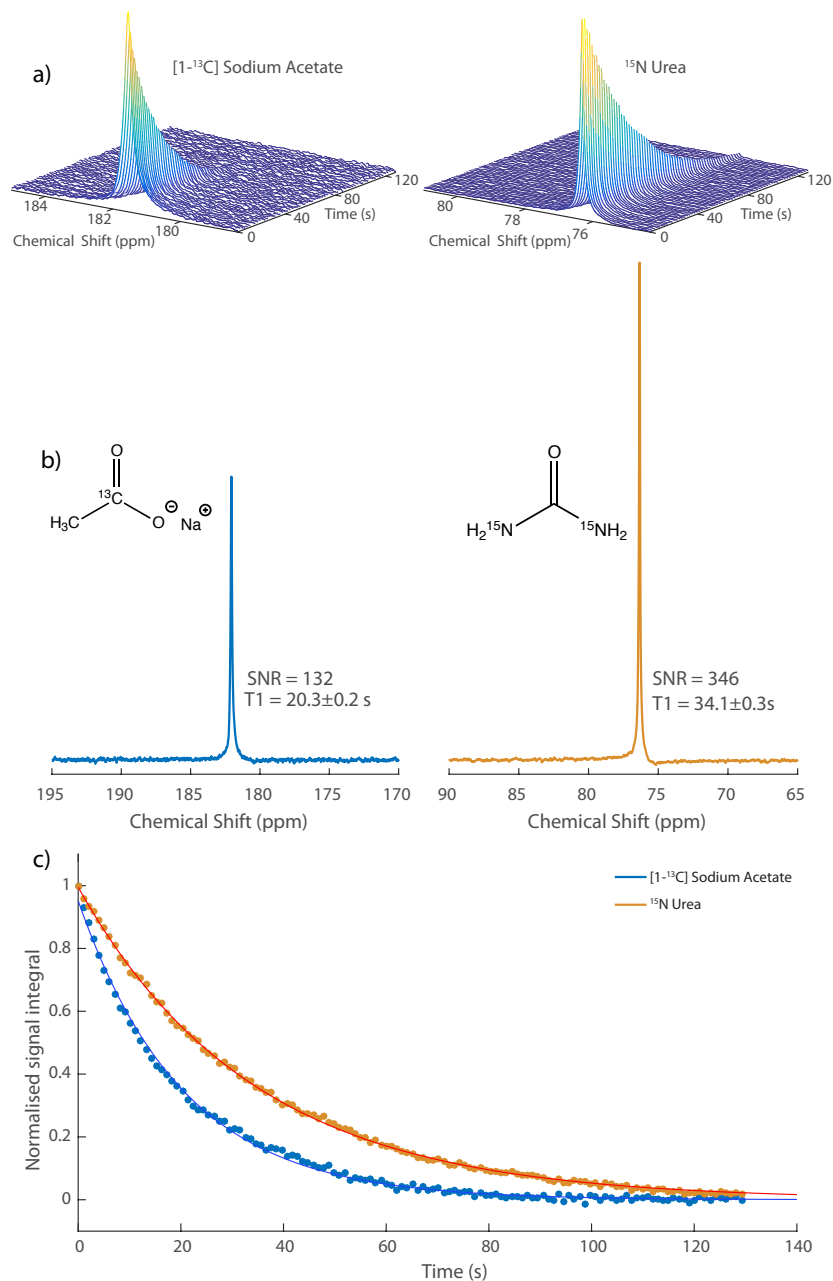
Figure 6.2: Results of multi-nuclear dissolution DNP performed on a sample containing both ^{15}N-Urea and [1-^{13}C]-Sodium Acetate. a) The time course of the NMR spectrum for both chemicals acquired simultaneously. b) The first spectrum of each acquisition with SNR and T_1 values for each resonance. c) The evolutions of the integrals of both resonances, normalised to the first spectrum. Mono-exponential fits allow determination of the relaxation times of 20.3 s for the sodium acetate and 34 s for the urea.

Parameter	Carbon	Nitrogen
DNP build up	50 minutes	
FID acquisition		
Power	3 W	3 W
Duration	3 μs	3 μs
Flip angle	0.5°	1°
Number of points	10058	6666
Acquisition duration	1 s	1 s
Spectral Width	50 ppm	82 ppm
Zero-filling	16384	16384
Apodisation	3 Hz	2 Hz
^{1}**H-Decoupling**		
Scheme	WALTZ-16	
Power	3 W	
90° Duration	37.5 μs	
DNP enhancement	4870	5230

Table 6.1: Experiment parameters for multi-nuclear dissolution DNP analysis of spin labelled Urea and Sodium Acetate. This co-acquisition included WALTZ-16 proton decoupling.

concentration should give a SNR of around 35.

6.4 Analysis of N-Acetyl-L-Aspartic Acid at Natural Abundance

To determine the sensitivity of the spectrometer with natural abundance molecules, N-Acetyl-Aspartic Acid (NAA) was tested. NAA provides an interesting test bed for quantifying the system's performance with both carbon and nitrogen spin species and a range of T_1s from around 300 ms up to 5 s. Initial characterisation of the molecule involved producing spectra both with and without proton decoupling (figure 6.3). The multiplet patterns of the aliphatic carbons makes assignment straightforward.
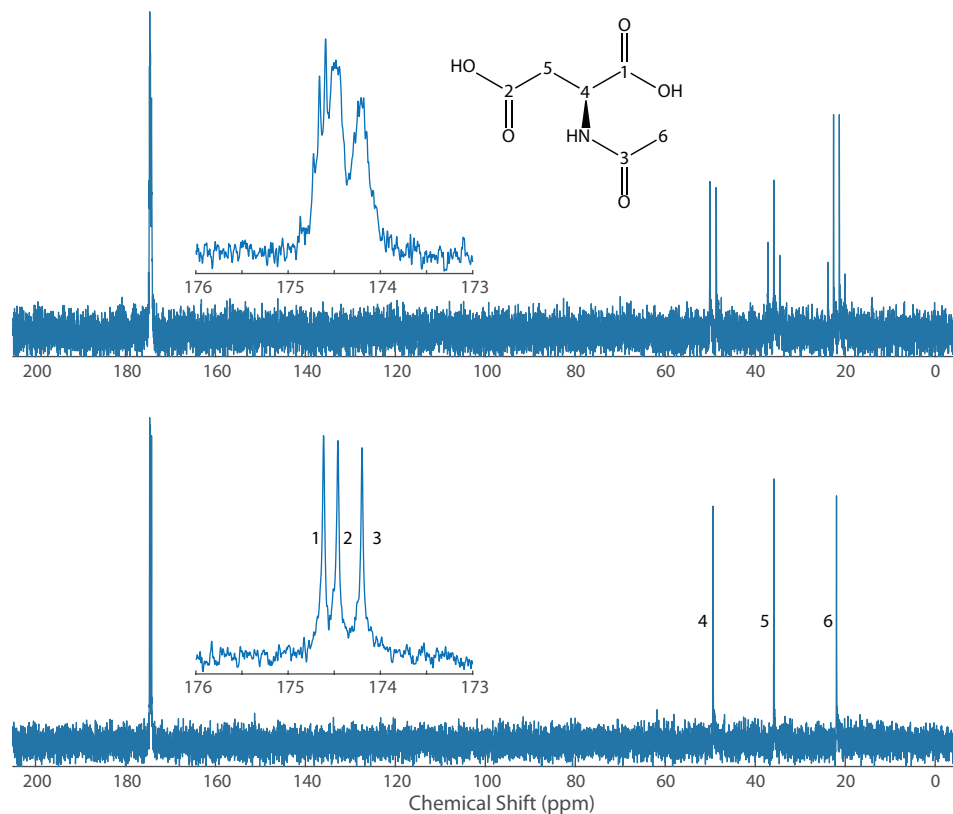
Figure 6.3: Carbon spectra for NAA acid TOP: *without Proton decoupling* BOTTOM: *with Proton decoupling* INSETS: *Zoom in on group of three carbonyl carbons. Also included is the molecular structure of NAA with the carbons labelled*

Two sets of experiments were performed. First, proton-decoupled carbon spectra were obtained using the inner coil of the TBO probe. Following this double acquisition was used to observe both carbon and nitrogen signals following sample dissolution.

Single species acquisition

For the single acquisition experiments a 200 μL 1M NAA sample was prepared with 15 mM Trityl in a 50:50 (by mass) H_2O/Glycerol mixture. 20 μL aliquots of this sample were then polarised for approximately 150 minutes at a temperature of around 1.65 K. Following sample dissolution, a single, triggered, 90° pulse was applied after a settling delay of 300 ms. Proton decoupling was performed with a

WALTZ-16 sequence with pulse power 3 W and a $90°$ pulse duration of 37.5 μs. For the FID, 64K complex points were acquired and zero-filled up to 128K points and apodised with a 4 Hz exponential decay window.

Peak	Chemical Shift (ppm)	Enhancement	Line width (Hz)
NAA			
1	174.8	5520	21.2
2	174.8	*	*
3	173.8	1970	13.8
4	49.8	3020	13.5
5	36.3	2800	16.7
6	21.8	200	14.9
Glycerol			
1	72.2	3410	13.2
2	62.7	4160	12.9
Ethanol			
1	57.5	†	13.6
2	16.9	†	13.6

Table 6.2: Peak data for N-Acetyl Aspartic Acid ^{13}C spins following dissolution DNP. The second NAA peak was not observed during the dissolution, however the first peak demonstrates significantly higher values for enhancement and line width, suggesting that the chemical shifts of the two peaks have overlapped. The enhancement values of the ethanol peaks have not been calculated as they arise from an unknown amount of sample contaminant.

Double species acquisition

Double acquisition followed the same protocol as described above. In this case, the nitrogen acquisition was performed on the inner coil and the carbon acquisition on the outer coil. The rough calculations presented in section 6.3.1 suggest that with 1 M of NAA, a signal to noise of around 17 should be achievable.

Peak	Dissolution (ppm)	Thermal (ppm)	Δ (Hz)
NAA			
1	174.8	174.4	39.6
2	*	174.2	(55.7)*
3	173.8	173.9	-13.0
4	49.8	49.3	54.3
5	36.3	35.8	46.1
6	21.8	21.9	-4.9
Glycerol			
1	72.2	72.3	7.8
2	62.7	62.7	0

Table 6.3: Table showing the change in chemical shift between the spectrum obtained through dissolution DNP and the one acquired from the same sample at thermal equilibrium. In this data, the spectra are calibrated to the second glycerol peak as shown on the bottom row.

6.4.1 Results

Single species acquisition

Figure 6.4 shows the hyperpolarised ^{13}C NAA spectrum acquired from the inner coil. The enhancement value for this molecule appear slightly lower than previous observed in spin labelled cases. The data for each peak is displayed in table 6.2. The peaks display enhancement values of around 2500 to 3000 for the NAA molecule. The first peak shows a higher value of 5520, however the second peak, another carbonyl that displays a chemical shift very close to the first, is not observed. The line width of the first peak is 7 Hz larger than the average of the other NAA peaks. It is reasonable to assume that the chemical shifts of the first two peaks have overlapped during the dissolution. This is most likely caused by the slight temperature dependence of the chemical shifts of these peaks. The change in chemical shift for the peaks of the sample post dissolution and then from the subsequent thermal scans is shown in table 6.3. In this table, the chemical shifts for the two sets of data are quoted with a reference of the second glycerol peak, hence its chemical shift difference is zero between data. The largest difference observed between data

Parameter	Carbon
DNP build up	150 minutes
FID acquisition	
Power	39 W
Duration	11 μs
Flip angle	90°
Number of points	10240
Acquisition duration	0.125 s
Spectral Width	404 ppm
Zero-filling	32k
Apodisation	5 Hz
^{1}H-Decoupling	
Scheme	WALTZ-16
Power	3 W
90° Duration	37.5 μs

Table 6.4: *Experimental parameters for acquisition of ^{13}C NAA at natural abundance*

sets is for the aliphatic CH carbon labelled as carbon-4, it has a shift of 54.3 Hz. If the sample temperature is the cause of the shift of the carbon-2 resonance then it would need to display a greater temperature dependence, with a shift of around 55.7 Hz. Confirmation of the cause of the chemical shift discrepancy will require further investigation.

Additional peaks are observed at around 17 ppm and 57 ppm, these peaks are associated with the ethanol used to clean the glass syringe used for loading the sample. The thermally acquired spectrum for NAA in figure 6.3 shows the aliphatic carbons appearing at roughly the same intensity. This is reasonable as there should be the same number of spins contributing to each peak. However the spectra produced after the dissolution experiment show significantly reduced intensities for the methyl carbon, to the extent that it does not appear in figure 6.6. Initially it was thought that this was due to the methyl carbon having a significantly short T_1 time. Figure 6.5 shows the T_1 relaxation times of the six NAA peaks for a range
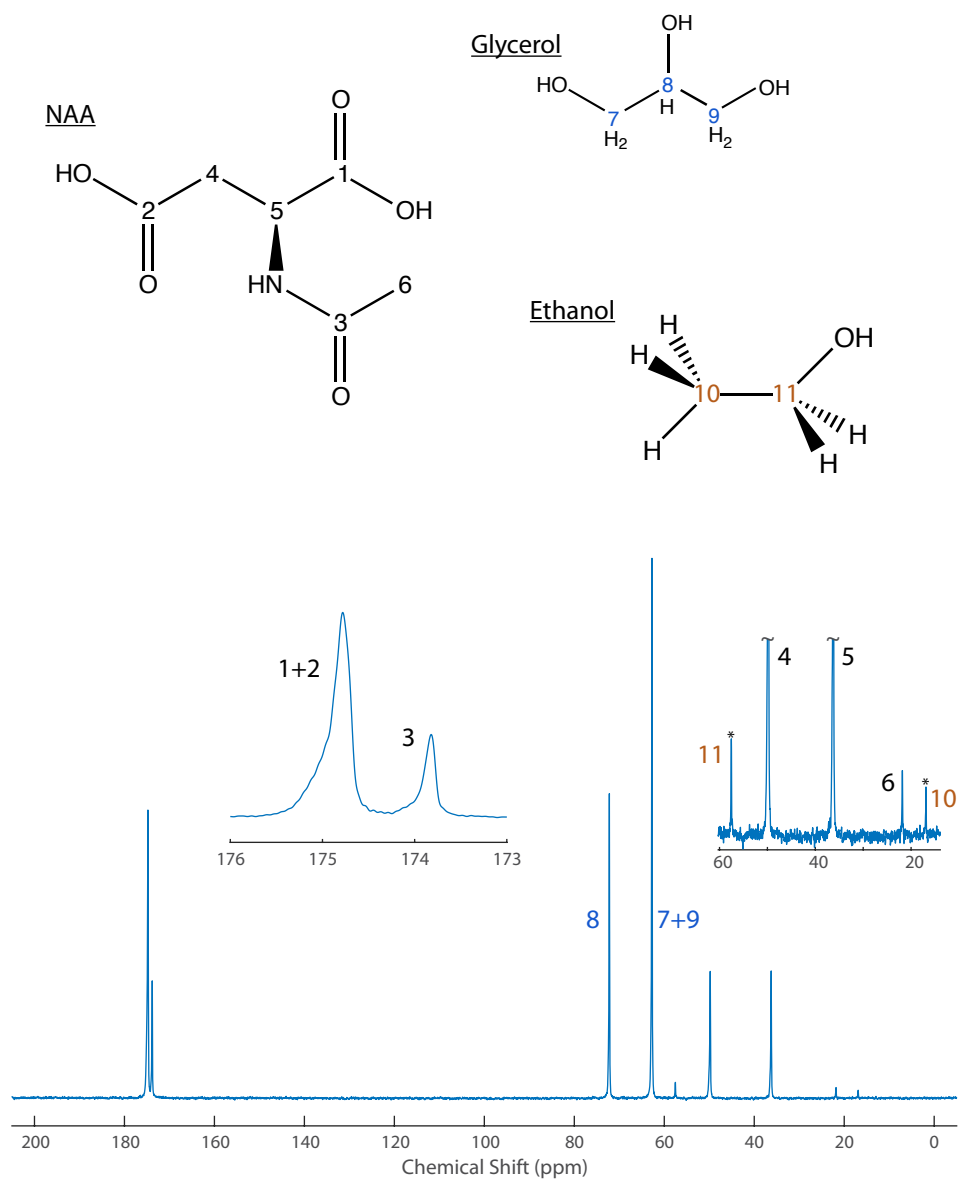
Figure 6.4: Hyperpolarised ^{13}C spectrum of NAA Acid at natural abundance. In the dissolution-DNP enhanced acquisition, two of the carbonyl resonances overlap, this is shown in the left inset. The right inset shows the small methyl resonance and the containment ethanol peaks
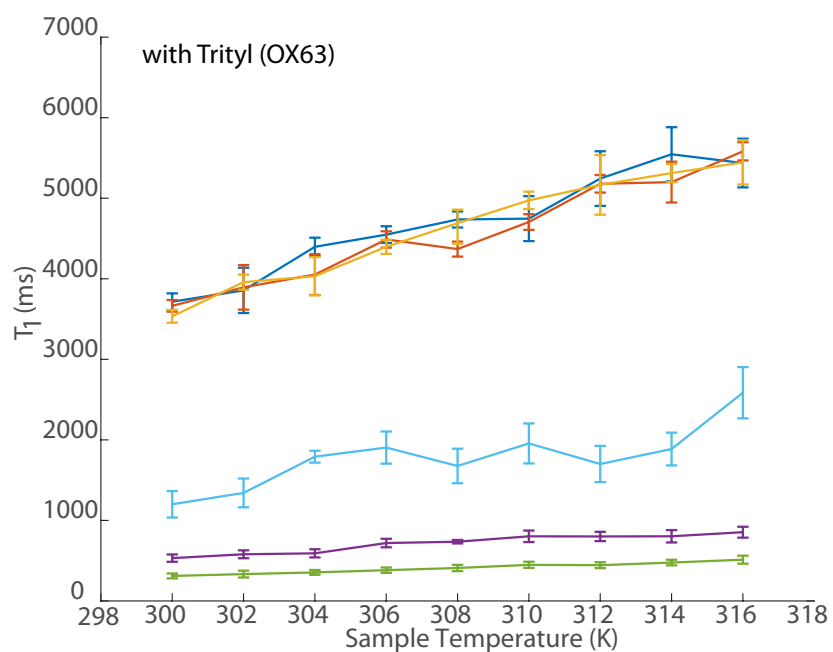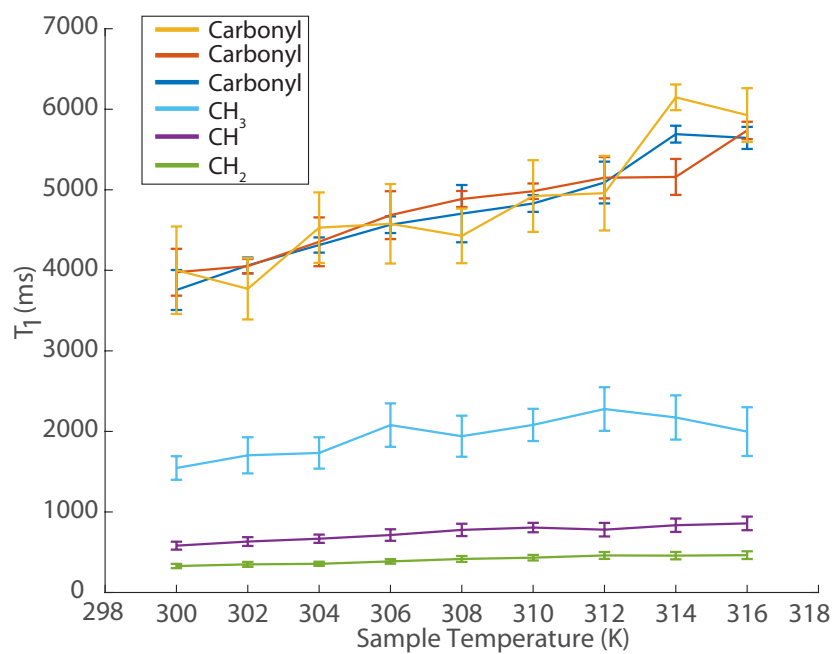
Figure 6.5: T_1 times for NAA as a function of temperature. The peak labels remain the same as those of the NAA molecule on previous spectra. TOP: *T_1 times with no Trityl.* BOTTOM: *T_1 times with approximately 1.5 mM Trityl. The concentration of Trityl radical of 1.5 mM is considerably larger than it would be in a dissolution sample but there is still no significant change in the nuclear relaxation rates. The methyl carbon, peak 6, shows T_1 relaxation times on the order of 1 to 2 seconds, significantly longer than the other aliphatic carbons.*

of applicable temperatures (300 K up to 316 K) both with and without Trityl (1.5 mM Trityl concentration). These values were acquired through inversion recovery experiments. At all temperatures, the carbonyl carbons relax at very similar rates, with only a slight increase in T_1 with temperature. However, also at all temperatures, the methyl carbon shows relaxation times that are longer than the other aliphatic carbons, between 1 and 2 seconds for the methyl spins as opposed to between 300 and 800 ms for the other aliphatic spins. This means that relaxation effects do not explain the reduced signal intensity of the methyl carbons. Rather, the methyl carbons simply do not accrue the same level of polarisation as the other carbons on the NAA molecule. At cryogenic temperatures, methyl groups act as quantum rotors, with T_1 times that are significantly shorter than other carbons in the solid state [100]. Such short T_1s would mean that the methyl carbon will reach its saturated polarisation level quickly, however the polarisation will be much lower than that observed in other carbons. Günther and co-workers also suggest that at temperatures below 1.5 K these methyl rotors exhibit Quantum Rotor induced Polarisation [101]. This polarisation pathway can build up polarisation spontaneously on methyl spins if they are kept at low temperatures for duration on the order of 20 hours. This sample was polarised at low temperatures for only around 2.5 hours, so a destructive build up of quantum rotor polarisation seems unlikely. However they also state that this process can interfere with the build-up of polarisation through DNP. The most likely explanation for the lack of polarisation build up is that methyl groups at low temperatures demonstrate relatively short T_1 times. This is because, even in the solid-state, the methyl group is reasonably free to rotate [102]. If this is the case then the methyl spins would reach a saturated polarisation level significantly lower than the other spins.

Double species acquisition

The co-acquisition of carbon and nitrogen spins was successful in observing both species. The carbon spectrum in figure 6.6 show similar characteristics to figure 6.4. The enhancement values were calculated from comparison to a 1 M NAA sample.

The enhancements calculated are around half of what was observed in the previous dissolution. The cause of the reduction in signal it not clear, however many parameters such as microwave alignment, sample temperature and concentrations of radical and glassing agent will all effect the efficiency of the DNP processes between experiments. One major cause of the reduction of nuclear spin polarisation is through a reduction in spin diffusion. As spin diffusion is mediated through space, the strength of the interaction between spins decays significantly with inter-spin distance ($1/r^3$). In spin labelled samples, the inter-spin distance will be reduced through the isotropic labelling of the sample. This in turn increases the rate at which spin polarisation will proliferate around the sample, increasing the nuclear polarisation build up time. There would also be a abundant source of nitrogen-14 in the sample. This spin-1 quadrupole would provide and additional relaxation pathway for the surrounding nuclear spins, reducing the saturation polarisation level.

The nitrogen spectrum shows a single resonance for the molecule. The signal to noise of the peak is 5.3, only around one third of the value predicted in section 6.4. As the sample was polarised for 150 minutes, this suggests that the nitrogen on the NAA molecule has a DNP build up time of significantly longer than 30 minutes. The enhancement of the peak was not determined as, even with a 1 M reference sample, a comparative thermal signal could not be acquired in a reasonable amount of time.

The sensitivity of the instrument can be determined by considering the concentration of spins that are providing the observed signals. Here, the initial sample contained 1 M of NAA would produce a dissolved sample with a NAA concentration of approximately 25 mM. Of this concentration there would be around 250 nM of contributing ^{13}C spins and around 90 nM of ^{15}N spins. This means that with current experimental parameter natural abundance nitrogen signals should be observable at final concentrations of above 10 mM. Allowing the initial frozen

sample concentration to be reduced down to around 400 mM. Using spin labelled samples would allow a further reduction in initial sample concentration down to only a few mM. However this is an extreme case that displays the instrument's ability to observe mass-limited compounds.

Peak	Enhancement	Line width (Hz)
NAA		
1	5010	19.0
2	*	*
3	1730	10.8
4	1790	18.0
5	1600	15.2
6	*	*
^{15}N	†	13.0
Glycerol		
1	1460	14.2
2	1230	14.9

Table 6.5: Peak data from multi-nuclear dissolution-DNP. The enhancements observed following dissolution are less than previous experiments. The NAA nitrogen resonance was successfully observed during the experiment, however an enhancement value could not be calculated as a thermal signal was not obtainable.

6.5   Conclusion

This chapter presents a method for increasing the data acquired following a dissolution DNP experiment by observing two nuclear spin species simultaneously. While the feasibility to use DNP to polarise two nuclei at the same time has been presented previously, it remains a generally under-explored avenue for the development of dissolution DNP experiments. Carbon and nitrogen provide a convenient pair to test multi-nuclear DNP as they exhibit very similar DNP sweep curves at the experimental conditions used.

The results presented suggest that multi-nuclear DNP has the ability to determine

Parameter	Carbon	Nitrogen
DNP build up	150 minutes	
FID acquisition		
Power	39 W	39 W
Duration	45 μs	23 μs
Flip angle	90°	90°
Number of points	163k	43k
Acquisition duration	2 s	2 s
Spectral Width	405 ppm	268 ppm
Zero-filling	262k	65k
Apodisation	5 Hz	8 Hz
^{1}**H-Decoupling**		
Scheme	WALTZ-16	
Power	3 W	
90° Duration	37.5 μs	

Table 6.6: Experimental parameters for multi-nuclear DNP acquisition of NAA at natural abundance.

molecular information from natural abundance sample using a 90° pulse from both carbon and nitrogen spins at low concentration. This method should speed up the characterisation of arbitrary molecules by providing complimentary data from each species. However, the main advantage of multi-nuclear DNP is additional information provided by monitoring spin labelled samples with small pulses, and could be useful when observing chemical reactions or conformational changes in organic molecules containing both ^{13}C and ^{15}N nuclei. This process is also assisted by the speed at which NMR acquisition can be performed with the dual-core spectrometer, allowing spins with T_1 relaxation times of below half a second to be observed with a reasonable enhancement factor. The limiting factor in the experiments presented here is the total level of polarisation produced by the dual iso-centre system.

This process could be extended by incorporating cross-polarisation methods into the polarisation stage [103]. During cross-polarisation, DNP is first performed on
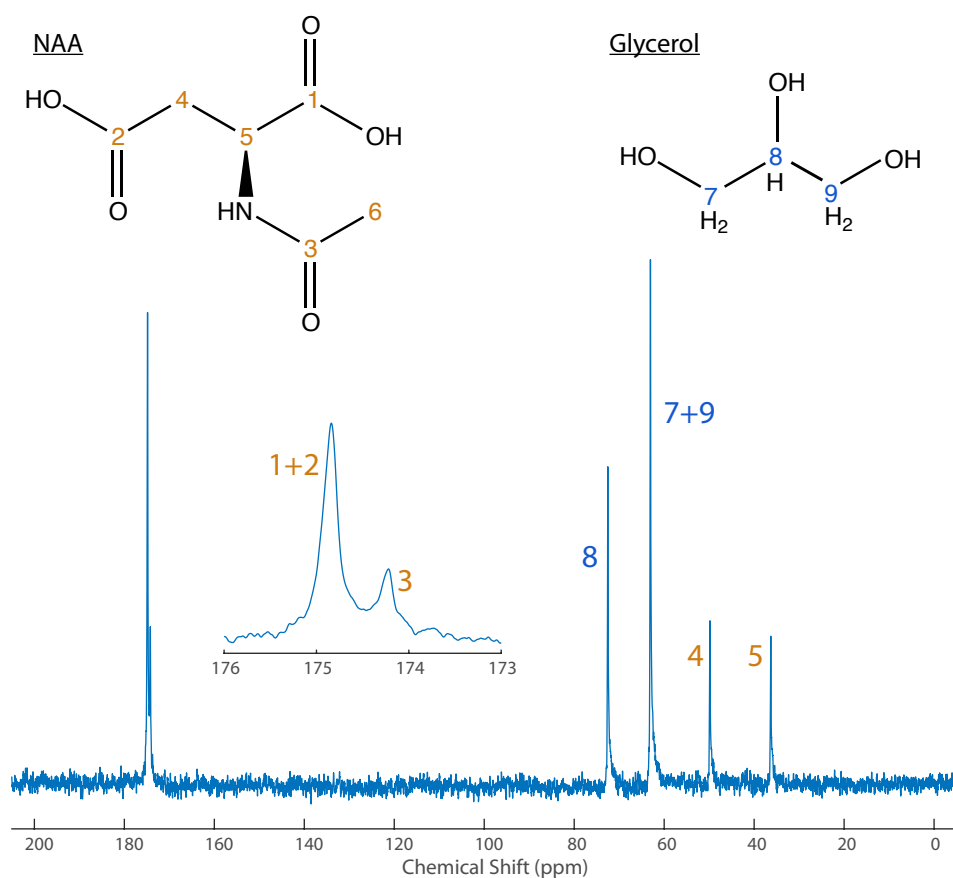
Figure 6.6: Hyperpolarised ^{13}C NAA at natural abundance observed during double acquisition. Again, the first two carbonyl peaks demonstrate overlapping chemical shifts. The signal to noise of the carbon resonances is significantly lower than previous experiments using the inner coil of the TBO probe. This is partly due to the lower sensitivity of the coil and partly down to the lower polarisation level achieved through DNP. This spectrum was acquired from a dissolution sample that contained approximately 25 mM of NAA with the natural abundance of each isotope. Therefore there is a concentration of about 250 nM of contributing molecules containing ^{13}C.

to protons before a transfer scheme sends the polarisation from proton onto the second nucleus, usually carbon [64]. CP schemes could be tailored for different sets of nuclei that do not polarise at similar frequencies.

SNR = 5.3

Chemical Shift (ppm)
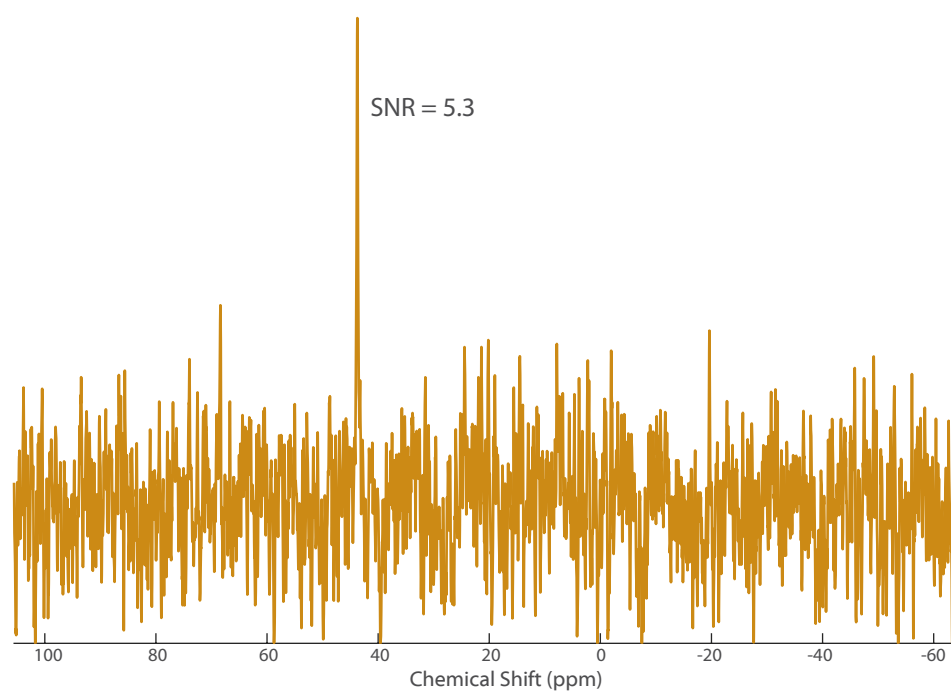
Figure 6.7: Hyperpolarised ^{15}N spectrum of NAA at natural abundance observed during during proton-decoupled dual acquisition. The signal to noise of the acquisition is 5.3. This spectrum was acquired from a dissolution sample that contained approximately 25 mM of NAA with nitrogen isotopes at natural abundance. Therefore there is approximately 90 nM of NAA containing ^{15}N spins.

7

Nuclear Magnetic Resonance with Multiple RF Acquisition Channels

It could be argued with some vehemence that the biggest bane of a high-resolution NMR spectroscopist's existence is the ritual of "magnet shimming." This black art can provoke hyperbole and hypertension...

– Chmurny & Hoult *The Ancient and Honourable Art of Shimming*

7.1   Introduction

The previous chapter discussed the use of multi-nuclear acquisition to increase the information extracted from a dissolution DNP experiment. Another method is to observe the same nucleus with a number of coils situated in different positions along the sample. For conventional NMR, previous work has shown that using n coils can speed up data acquisition by factor of n. Wang and co-workers have pioneered the use of multiple acquisition coils for increasing the throughput of NMR experiments [104]. They showed a probe, housing 8 solenoid micro-coils, which was connected to a 4 channel spectrometer. Each channel was connected to two coils on the probe, so radio-frequency switches were used to duplex each acquisi-

147

tion channel and interlace the recording of data. This was then extended in the use of a 4 coil probe to increase the acquisition speed of 2D spectra [105], here they showed that by distributing the evolution times across different channels, the 2D acquisition could be sped up by a factor of the number of coils, in this case 4.

These developments have looked to speed up data acquisition that usually takes a prohibitively long time to complete. Conversely, combining a multi-coil approach with the highly enhanced signal produced by dissolution DNP looks to solve the opposite problem, where the data simply can't be acquired quickly enough.

A six micro-coil probe head has been designed to be used in conjunction with a modified version of an Avance III console (Bruker Biospin GmbH). This system, nicknamed Godzuki[1], contains six sets of Tx/Rx hardware interfaced to the same control unit. This means that each of the channels can be used entirely independently from one another. Previous work with multiple coils required the channels of the spectrometer to be multiplexed [106, 107].

This chapter introduces the use of the six-coil probe in conjunction with dissolution-DNP. The design of the probe is discussed and how it connects with both the dissolution apparatus and the spectrometer. Initial testing was done using a fluid flow through the probe as well as optimising the parameters controlling probe filling during a dissolution experiment. A method is proposed to iteratively shim the six coils using a modified version of the simplex algorithm. A simulation program was developed to determine the advantage of using multiple coils for acquisition of dynamic information from a simple chemical reaction. Then the probe was then used to determine a *pseudo* rate coefficient of a controlled flow of fluid. Finally, initial work carried out into acquiring DNP enhanced liquid-state NMR with the six-coil probe is presented.

---

[1]Godzuki is the child of Godzilla in the famous Japanese canon. The first incarnation of the six channel console was nicknamed Godzilla by Bruker engineers

7.2   Design and geometry

The design of the six-coil probe is based around a modified Bruker flow probe. Inside a flow probe, the sample sits in a narrow (0.4 mm i.d.) capillary rather than a NMR tube, this means that samples can be flowed through the probe easily [108]. Another advantage is that the coils can be made to fit snugly around the capillary outer wall, this increases the fulling factor of the coil and increasing its signal-to-noise level. Many flow probes contain a small sample cell (with volumes on the order of 40-60 μL), these cells are then filled by injecting the sample into an inlet at the base of the probe. The advantage of filling the probe from the bottom is that the cell fills in a laminar fashion, with the air inside the cell reliably expelled from an outlet at the top.

The sample injection capabilities of flow probes is advantageous dissolution experiments as it allows the dissolution flow path to be coupled directly to the flow path within the probe, removing the sample spraying produced during the experiments introduced in previous chapters.
The six-coil probe is different in that it does not contain sample cells and it is filled from above. In the dual-core system the hyperpolarised liquid sample is delivered from the dissolution dock directly above the NMR probe. It is therefore useful for the six-coil probe to be filled directly from the dissolution dock. In this situation it would not be possible to precisely fill a sample cell while removing the gas inside. Instead, the six NMR coils have been designed to fit almost directly on the narrow capillary that travels though the probe. This capillary has dimensions 1 mm o.d. and 0.4 mm i.d. and runs for around 300 mm down the length of the probe.

Figure 7.1 shows how the coils are situated in two layers of three coils. The capillary path comes down from the top of the probe and passes through two coils before making a u-bend and passing through two more coils, a second u-bend takes the path back down, through the last two coils and on towards the base of the probe.
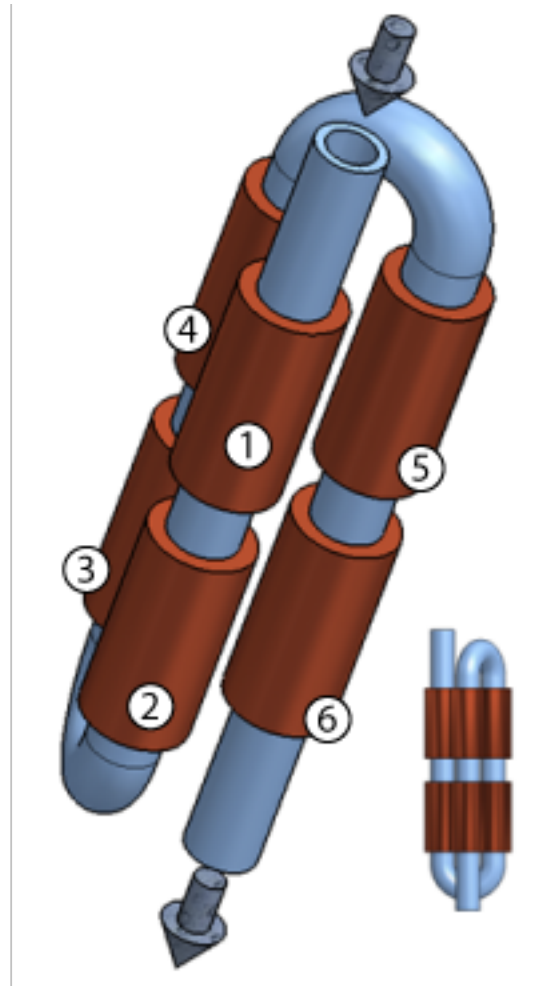
Figure 7.1: Illustration of the lay out of the six coils in the six-coil flow probe. Micro-coils have been designed to sit perfectly around the capillary flow path in two layers of three. The coils are 4 mm in length. The capillary fixes to the top of the probe to allow delivery of fluid from the dissolution dock. The capillary leave the probe though an outlet at the base of the probe. (Diagram provided by Ed Breeds)

Five of the six coils are tuned exclusively to ^{13}C. The sixth coil is dual tuned to ^{13}C and ^{2}H.

7.2.1   Flow rate through the probe

Dissolution experiments that were performed into the BBI and TBO probes involved injecting the solution directly into a NMR tube through the *rocket* connector. The six coil probe does not attach to the dock with the rocket, rather it connects directly to the proboscis with a PEEK extender. And, when connecting the flow path of the six coil probe directly to the dissolution system it is important to consider the flow rate of the liquid down the capillary. Tests were performed to determine the liquid flow rate through the probe with a range of different fluid viscosities and driving pressures.

To vary the viscosity of the fluid, tests were performed with distilled water that contained a small admixture of glycerol. Glycerol is used as the glassing agent for dissolution experiments. The range of glycerol amounts used included values that were far above what could be expected during a dissolution experiment. In a standard dissolution sample there is 10 μL of glycerol, after dissolution this volume is dispersed in an overall sample volume of around 600 μL. If the hyperpolarised sample is dissolved consistently during solvent delivery, then the percentage of glycerol in the flowing liquid should never exceed 1.7%. It is unlikely that this is the case, so glycerol percentages of up to 7.6% were tested. To determine the flow rate through the system 10 ml of water and glycerol mixtures were placed in the solvent reservoir. With a driving pressure of 2.5 bar, the time was measured between the start of the liquid flow and the points when all the liquid had drained out of the probe. This process was repeated 5 times per glycerol concentration. Figure 7.2:TOP shows how the flow time changed as a function of glycerol percentage. As expected, the increased viscosity reduces the rate at which the fluid can flow through the probe, however this change is small for all reasonable glycerol concentrations.

151

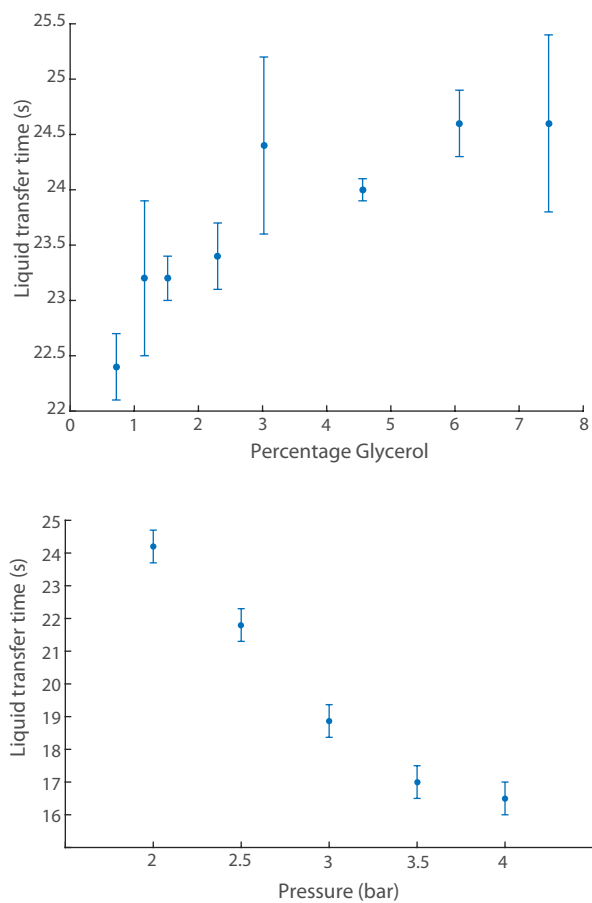*Figure 7.2: TOP: Time of flow experiments for different glycerol concentrations. A set of 10 mL samples were produced with varying concentrations of glycerol. These samples were then flowed through the probe with a driving pressure of 2.5 bar and the time recorded. BOTTOM: Flow rate experiments as a function of driving pressure. These trials used 10 mL of demineralised water with a range of driving pressures.*

7.2.2 Coil Cross talk

The six-coil probe used in this project was the second generation probe developed by Bruker, building on the improvements suggested in [26]. In the original probe, the two layers of coils were shielded from each other by a grounded copper sheet, but it lacked RF shielding between the individual coil in-layer. This meant that there was significant coupling between the coils. Van der Drift presented a method to quantify this coupling that involved sending an NMR pulse to an individual coil but acquiring FIDs on all channels simultaneously [26]. Each FID was Fourier transformed and the integral of the resultant peaks calculated. The effective coupling between two coils was then defined as the percentage of the active coil spectral integral observed on the passive coil. Her tests acquired spectra from neat ^{13}C-methanol. The percentage coupling observed is presented in table 7.1. These numbers provide a good indication of the effective cross talk between two coils and were considered unsatisfactory to produce reliable NMR data. Hence the second generation probe incorporates significantly improved RF shielding between the individual coils. The design of this shielding is not introduced here as it remains propriety technology owned by Bruker Biospin GmbH.

The initial cross-talk tests of the second generation probe revealed that no NMR signal was observable at the other coils when using the method presented above. To determine the level of coupling between these coils a more sensitive method was required. The probe was connected up to a network analyser (Agilent - HP 4396B) and a frequency-sweeping test signal sent to the coils individually. By attaching a second (observe) coil to the secondary input of the network analyser it is possible to observe the frequency-dependent inductive coupling between the two coils. This provides coupling information down to levels around -50 dB. Table 7.2 shows the inductive coupling observed between coils. The levels observed in decibels have been converted to percentages for comparison with table 7.1. The new six-coil probe demonstrates inductive coupling which is around two orders of magnitude
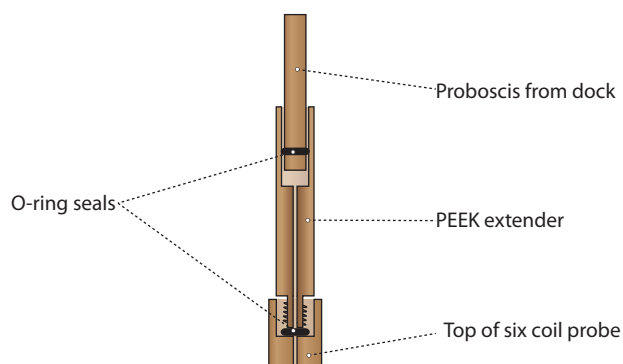
Figure 7.3: PEEK extender between dissolution dock and six coil probe. The extender screws onto the top of the six coil probe and forms an o-ring seal. The probe is then inserted into the bore of the magnet and is located with delrin spacers to the proboscis which is protruding out of the bottom of the dock. The o-ring on the end of the proboscis forms another seal with the with the extender. This allows a fully sealed connection between the dissolution flow path and the flow probe.

smaller than its predecessor. No coil sees more than 0.44% of the power emitted from other coils. The transfer of power through inductive coupling between the coils can be considered negligible.

7.2.3   Interfacing with dissolution system

The top of the six coil probe has a 6 mm threaded hole. To connect the probe with the proboscis (outlet extension) at the bottom of the dissolution dock, a PEEK tube extends up from the probe (see figure 7.3). The o-ring on the proboscis forms an air-tight seal with this extender and an o-ring sitting in the top of the probe also stops any fluid leaks from that fitting. This fitting allows reliable liquid transfer at pressures of up to 4.5 bar.

7.3   Shimming the six-coil probe

Shimming individual micro-coils should be a relatively easy process as the sensitive volume is small compared to the field inhomogeneities present in NMR magnets. However the six-coil probe demonstrated significant ^{13}C line widths prior

	Active Coil:	1	2	3	4	5	6
	1	100	6	15	7	21	1
	2	0	100	0	9	2	13
Observe Coil:	3	18	10	100	11	22	2
	4	10	28	11	100	5	14
	5	24	3	17	4	100	3
	6	6	40	2	30	8	100

Table 7.1: *Percentage cross talk of original six coil probe. Numbers are calculated from integral of NMR peak when pulsing on the active coil and observing on all others. Data taken from [26].*

	Active Coil:	1	2	3	4	5	6
	1	100	0.07	0.01	0.12	0.33	0.00
	2	0.08	100	0.43	0.01	0.03	0.02
Observe Coil:	3	0.01	0.44	100	0.01	0.03	0.19
	4	0.12	0.01	0.01	100	0.12	0.00
	5	0.32	0.01	0.03	0.12	100	0.14
	6	0.00	0.02	0.26	0.00	0.13	100

Table 7.2: *Percentage cross talk between coils of the second generation six coil probe with advanced RF shielding between coils. Direct electrical coupling between the coils was measured by network analyser as described in section 7.2.2*

	Active Coil:	1	2	3	4	5	6
	1	-	-31	-40	-29	-25	-50
	2	-31	-	-24	-40	-35	-37
Observe Coil:	3	-40	-24	-	-40	-35	-27
	4	-29	-40	-40	-	-29	-50
	5	-25	-40	-35	-29	-	-29
	6	-50	-37	-26	-50	-29	-

Table 7.3: *Cross talk between coils in dB attenuation. This is the same data as that provided in table 7.2.*

to shimming. Samples of high concentration [2-^{13}C] Sodium Acetate gave widths of 80 Hz and higher when no shim fields were applied to the system.

The design of the coils mean that shimming the probe is not a trivial process. Firstly, the separation of coils within the probe is on the order of the overall expected homogeneous region of the wide-bore magnet. Rather than producing a single set of shim current values that give narrow resonance on a single coil, a compromise is required that minimises the inhomogeneity of all the coils simultaneously. Secondly, as the coils are only tuned to ^{13}C, thermally polarised samples with large line widths produce only small signal-to-noise ratios even after signal averaging. As the probe does not have the ability to perform gradient shimming an iterative process was required. The lack of signal, especially early in the shimming routine, means that the time required to produce a reasonable shim set was around about eight hours, even with high concentration, spin-labelled, samples. Finally, NMR probes tend to store samples co-axially with the bore of the magnet, for example NMR tubes sit perfectly in the centre. This means that line broadening caused by field inhomogeneities that are a function of x or y position will be restricted to a level defined by the inner diameter of the sample tube, this is similarly true for multi-coil systems with coils that are distributed only along z. In the case of multiple coils separated in x, y and z then in-plane inhomogeneities will have a significant effect and will need to be corrected for.

The Simplex algorithm has been used for a number of years as a means of producing shim current values that are close to optimum for a given probe [109]. An introduction to the Simplex algorithm can be found in section 3.2.1. For shimming, usually either the strength of the lock channel signal or the integral of an observed FID is used as the quality parameter. This parameter is calculated by summing the absolute value of all the complex points that make up the FID. This value is not able to provide a qualitative description of the efficacy of the shimming, however changes to this value across successive iteration of the simplex algorithm

156

is capable of efficiently optimising shim current values. The FID area is a good parameter to shim to as it increases directly in response to the duration of the time series signal; the longer the signal, the greater the FID area. In terms of shimming, the FID will increase in duration as T_2* approaches T_2 i.e. when the magnetic inhomogeneities are minimised.

7.3.1 Individually shimmed coils

Initially, the Simplex algorithm was applied to each coil individually. The most likely outcome of individual shims was the minimisation of line width on that coil, entirely at the expense of the other coils. Line widths of 6M [2-^{13}C] Sodium Acetate of between 4 and 7 Hz were observed for individual coils with no signal at all being observed on the other channels. Occasionally however the Simplex would find a local minimum that also produced relatively narrow lines on the other coils. Table 7.4 shows the best line width values obtained through individual coil application of the Simplex algorithm.

The line widths presented in table 7.4 were not deemed narrow enough for adequate NMR analysis so work was carried out into modifying the Simplex algorithm so that it took information from all six coils at the same time.

	Observe Coil:	1	2	3	4	5	6
	1	**9**	11	10	7	20	35
	2	43	**8**	14	15	65	270
Shimmed Coil:	3	20	8	**7**	8	14	200
	4	15	15	15	**10**	14	220
	5	15	22	15	10	**11**	200
	6	41	100	50	47	38	**15**

Table 7.4: Line widths of the six coil probe following successful simplex shimming on individual coils. The coil that was shimmed is numbered in the first column and the result line widths shown on each row.

7.3.2 Modified simplex algorithm

The Simplex method used in the previous section uses the integral of the acquired FID as the quality parameter which defines the topology. To take information from all six coils, the first step was to simply add together the integrals of the six acquired FIDs. This process tended to preferentially shim the coils which reacted most to the initial steps the simplex algorithm took.

By defining the quality parameter such that the variance between the FID integral of each coil is considered, the algorithm was given a quality parameter that both encouraged shimming but attempted to maintain a compromise between coils. Mathematically, the Simplex algorithm worked with a quality parameter defined by the equation

$$Q = \bar{I}_{FID} - A \times \sigma(I_{FID}),\tag{7.1}$$

where,

$$\sigma(I_{FID}) = \sqrt{\frac{\sum_{i=1}^{6}(I_i - \bar{I}_{FID})}{5}}.\tag{7.2}$$

The coefficient A included in equation 7.1 allows the contribution of the standard deviation to be changed and more or less emphasis placed on the homogeneity between coils. Initial tests involved running the Simplex algorithm with $A = 1$. The results of these tests were broadly the same as they were prior to the inclusion of the standard deviation. The tests were then repeated with a more significant weighting for the standard deviation.

To test this quality parameter, the six-coil probe was loaded with a 6 M [2-^{13}C] Sodium Acetate sample in water. In this case, the methyl label was chosen as it demonstrates significantly faster nuclear relaxation (with a T_1 time of around 5 s), this means that thermal averages can be obtained more quickly. Four 30° pulses

were used to produce the FIDs used in the quality parameter. The Simplex algorithm was run to optimise the shims: Z, Z^2, X, Y and XYZ.

Figure 7.4 shows the averaged results following 28 multi-coil simplex trials with a variance weighting factor $A = 1.25$. In these tests, the Simplex algorithm still tended to optimise some coils over others. As is shown in panel a) of the figure, coils two and three improve most significantly over the course of a simplex trial. This is most like a result of those coils being more sensitive than the others.

Values of A of 2 or higher consistently maximised the Q-factor by ruining the signal on all coils, thus minimising the variance. Shim current trajectories for each Simplex trial are shown in figure 7.6, these data show that four of the five shim values tended to converge onto a small range of values, suggesting that the algorithm is capable of locating minima within the shim topology. However the wide variety of trajectories shown for the XYZ shim shows that global minima or not always easily found. An example of one of the observed shim sets with the modified Simplex algorithm can be seen in figure 7.7. The line widths, while usable, are still high for micro-coil spectroscopy. The average signal to noise observed for all observed shim sets is shown in figure 7.5. Coils 2, 3 and 5 consistently react better to the algorithm than the other coils.

The multi-coil Simplex method is significantly more reliable at shimming the six-coil probe than shimming coils individually. Including the variance of signal between the coils has stopped individual coils maximising the Q-factor. However, the shim sets produced do not provide line widths that are any narrower than set produced with some single-coil Simplex trials. The variance coefficient of $A = 1.25$ provided the most reliable shimming routine, however only a small range of values were tested: $A = [1, 1.25, 2, 5]$ as each multi-coil simplex trial took too long to perform a systematic test.
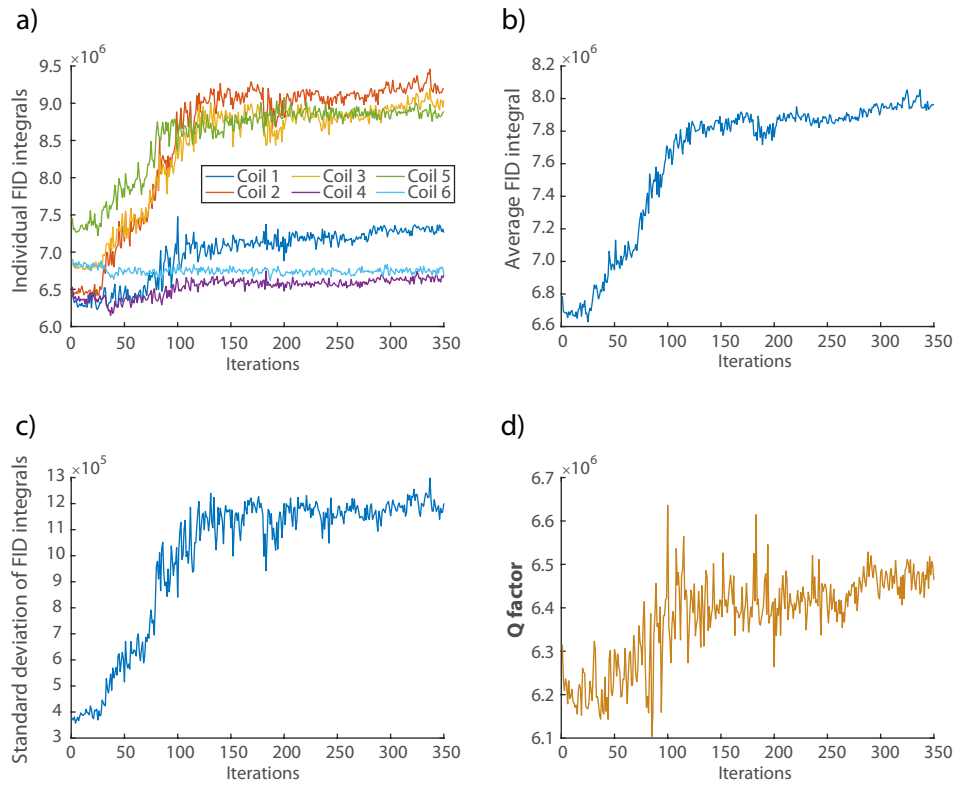
Figure 7.4: Results of modified simplex shimming routine. a) The FID area of each coil as a function of the number of iterations of the simplex algorithm. b) The average FID area of all six coils. c) The square root of the signal variance between the coils. d) The resultant Q-factor.
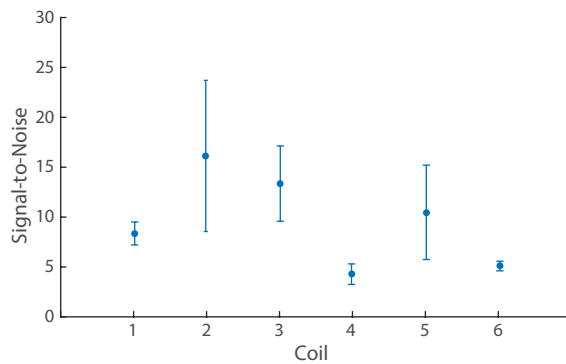
Figure 7.5: Average SNR of the six coils following shimming with modified Simplex algorithm following 28 trials
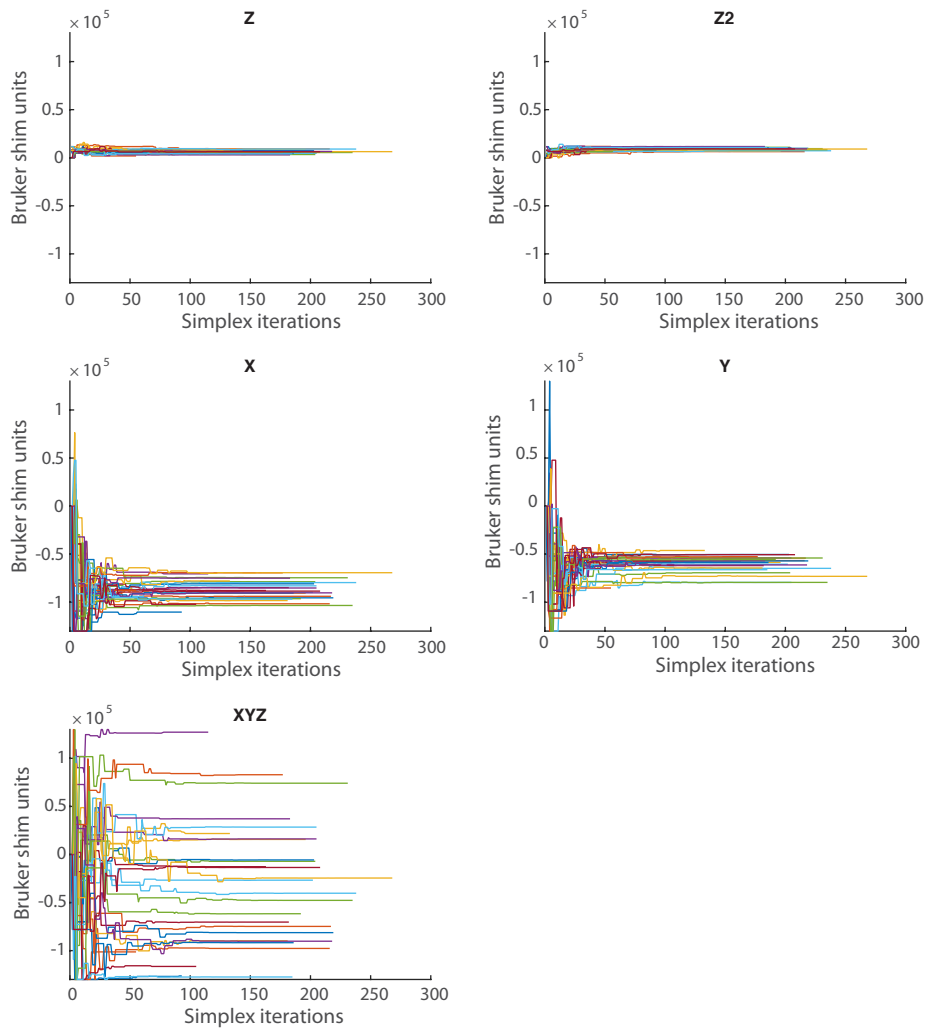
Figure 7.6: Evolution of shim currents as a function of Simplex iterations. 28 individual trajectories show that low order shims settle into certain regions of shim value, however higher orders such as XYZ do not converge. This means that the field inhomogeneities that are a function of XYZ are not important for optimising the line widths.

Coil 1
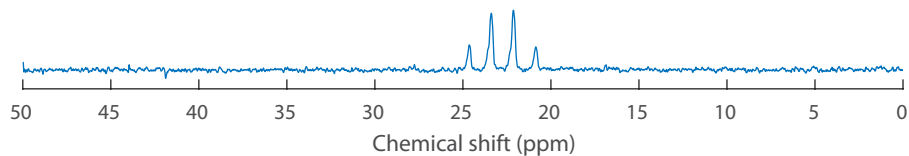
Coil 2
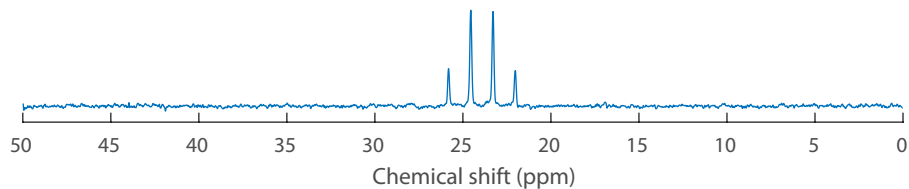
Coil 3
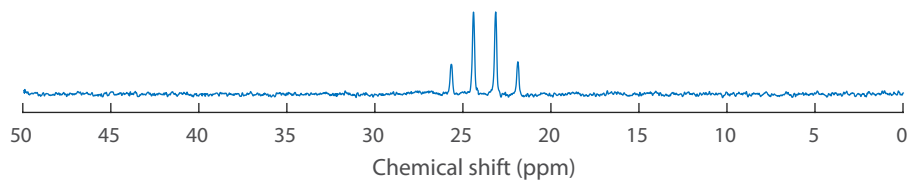
Coil 4
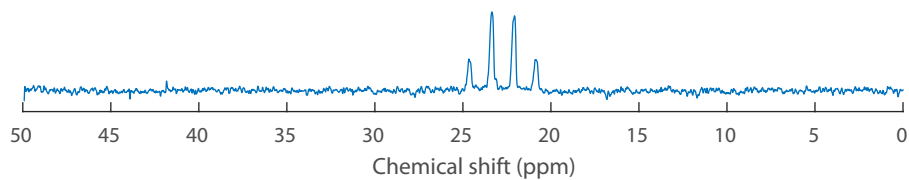
Coil 5
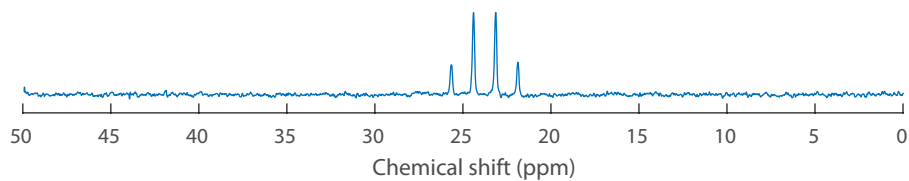
Coil 6
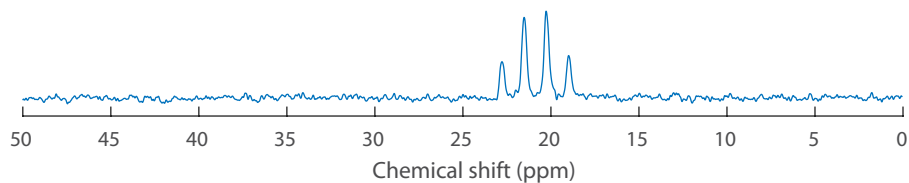
Figure 7.7: Spectra acquired using the six-coil probe and a 6 M [2-^{13}C] Sodium Acetate sample following shimming with the modified Simplex Algorithm. Coils 2, 3 and 5 show the greatest improvement following shimming.

162

7.4 Simulations using extended Bloch-McConnell equations

One of the principle goals of the six-coil probe is to analyse molecular dynamics that are too fast for individual coils to observe. To simulate such dynamics, a simulation based on the Bloch-McConnell equations was created. The basis of the simulation was an extension of the work carried out by Helgstrand and co-workers [110]. They present a method for obtaining NMR data from a system in non-equilibrium exchange. They simulate these spectra using both a classical Bloch approach and a quantum mechanical master equation approach. The work presented in this section is an extension of the Bloch approach.

As was introduced in section 2.1.6, the Bloch equations are descriptors for the dynamics of the magnetisation vector in each of the orthogonal Cartesian axes. In a matrix form they can be written as

$$\frac{d}{dt}\begin{bmatrix} M_x \\ M_y \\ M_z \end{bmatrix} = \begin{bmatrix} r_2 & \Omega & -\omega_y \\ \Omega & r_2 & \omega_x \\ \omega_y & -\omega_x & -r_1 \end{bmatrix}\begin{bmatrix} M_x \\ M_y \\ M_z \end{bmatrix} + \begin{bmatrix} 0 \\ 0 \\ r_1 M_0 \end{bmatrix} \tag{7.3}$$

where $r_{1,2}$ are the nuclear relaxation rates $(1/T_{1,2})$. The term Ω is the offset between the resonant frequency of the nucleus and the carrier frequency of the RF pulse

$$\Omega = \omega_0 - \omega_{rf}. \tag{7.4}$$

The terms $\omega_{x,y}$ are the strength of the x and y components of the applied RF field. In this form it is straightforward to apply pulses of arbitrary strength and phase. Before and after the pulse the terms Ω and $\omega_{x,y}$ equal zero. During the pulse, the $\omega_{x,y}$ components rotate the magnetisation into the x-y plane.

Equation 7.3 assumes that the equilibrium magnetisation always returns to the same value M_0. However if the level of equilibrium magnetisation is defined as being concentration dependent then the chemical exchange can be included as a variation of the equilibrium magnetisation level.

$$\frac{d}{dt}\begin{bmatrix} C \\ M_x \\ M_y \\ M_z \end{bmatrix} = \begin{bmatrix} 0 & 0 & 0 & 0 \\ 0 & r_2 & \Omega & -\omega_y \\ 0 & \Omega & r_2 & \omega_x \\ -r_1 M_0 & \omega_y & -\omega_x & r_1 \end{bmatrix} \begin{bmatrix} C \\ M_x \\ M_y \\ M_z \end{bmatrix}. \tag{7.5}$$

The additional constant C is a function of time. During a chemical reaction, this constant takes the value of the concentration of each spin. For a direct exchange reaction, the evolution of C can be described mathematically by the differential equation

$$\frac{d}{dt}C = -kC, \tag{7.6}$$

with the general solution

$$C(t) = C_0 e^{-kt}. \tag{7.7}$$

Equation 7.6 can be extended to include two spins (I and S) that exchange with each other with characteristic rates k_{IS} and k_{SI},

$$\frac{d}{dt}\begin{bmatrix} [I] \\ [S] \end{bmatrix} = \begin{bmatrix} -k_{IS} & k_{SI} \\ k_{SI} & -k_{IS} \end{bmatrix} \begin{bmatrix} [I] \\ [S] \end{bmatrix}. \tag{7.8}$$

In such a two spin system, there will be a Bloch matrix of the form of equation 7.5 describing the dynamics of each spin. Following [110], the overall Bloch-McConnell equation can then be obtained by constructing a Liouvillian state-space based on equations 7.8 and 7.5. This provides the full matrix form of the Bloch-McConnell equations as shown in equation 7.9. To extend this equation to incorporate six coils, the matrix is further expanded to include twelve sets of Bloch dynamics, one

for each spin on each coil. The state vector is also extended to include independent x, y and z magnetisations for each spin at each coil. As the reaction is assumed to be coil independent, only one set of concentration components are required. The result is a 1×38 state vector that contains 36 Bloch elements and 2 elements based on the time varying concentration. The Bloch-McConnell matrix has dimensions of 38×38. This system can then be solved numerically with the MATLAB ODE45 differential equation solver. In the simulation, arbitrary NMR pulses can be triggered simultaneously or staggered in time. Acquisition time and time domain points of the FIDs of each coil can be defined as they would on the spectrometer. During the simulation, it is assumed the spins are thermally polarised.

$$
\frac{\mathrm{d}}{\mathrm{d}t}
\begin{bmatrix}
M_{I0} \\
M_{S0} \\
I_x \\
I_y \\
I_z \\
S_x \\
S_y \\
S_z
\end{bmatrix}
=
$$

$$
\begin{bmatrix}
k_{IS} & -k_{SI} & 0 & 0 & 0 & 0 & 0 & 0 \\
-k_{IS} & k_{SI} & 0 & 0 & 0 & 0 & 0 & 0 \\
0 & 0 & r_{2I} + k_{IS} & \Omega_I & -\omega_y & -k_{SI} & 0 & 0 \\
0 & 0 & -\Omega_I & r_{2I} + k_{IS} & \omega_x & 0 & -k_{SI} & 0 \\
-r_{1I} & 0 & \omega_y & -\omega_x & r_{1I} + k_{IS} & 0 & 0 & -k_{SI} \\
0 & 0 & -k_{IS} & 0 & 0 & r_{2S} + k_{SI} & \Omega_B & -\omega_y \\
0 & 0 & 0 & -k_{IS} & 0 & -\Omega_S & r_{2S} + k_{SI} & \omega_x \\
0 & -r_{1S} & 0 & 0 & -k_{IS} & \omega_y & -\omega_x & r_{1S} + k_{SI}
\end{bmatrix}
$$

$$
\times
\begin{bmatrix}
M_{I0} \\
M_{S0} \\
I_x \\
I_y \\
I_z \\
S_x \\
S_y \\
S_z
\end{bmatrix}
\quad (7.9)
$$

Six-coil simulations

Simulations were performed using the extended Bloch-McConnell method for two proton spins at chemical shifts of 1 ppm and 2 ppm from the resonance frequency at 9.4 T. The reaction rates were set to $k_{IS} = 3$ s^{-1} and $k_{SI} = 0$ s^{-1} so that there was a direct conversion from one spin resonance into the other. At points staggered by 200 ms, 10 kHz pulses were applied for 25 μs, resulting in a 90° nutation of the z magnetisation at each coil. Both spins were given a T_1 relaxation time of 1 s and a T_2 relaxation time of 200 ms. The FID acquisition was 10^4 complex points over a duration of 800 ms. The FIDs were Fourier transformed and each peak was integrated. The results of the simulation are shown in figure 7.8. In the bottom panel of this figure, the integrals of the two peaks are plotted against the pulse times. This data provides two exponential fits, one decay and one build up, that can be fitted to extract the original reaction rate. For the simulation presented above the fits gave the rate coefficients:

Parameter	Value ($\pm 95\%$ confidence)
k_{IS}	3
Build up	2.5 ± 1.0
Decay	2.8 ± 0.4

Table 7.5: *Results showing reconstructed rate parameters obtained through simulated NMR data. The predefined k was successfully obtained through six NMR spectra taken at staggered intervals of 200 ms. The main source of error with these fits is the lack of points are long times following the reaction. These points would provide a baseline to which the reaction tend to.*

Within error, the data acquired from six channels can reconstruct the true reaction constant. This is a rather basic example of how the six coil probe could help with determining fast rate constants. In reality, individual FID acquisition could be shortened to speed up acquisition rate at the expense of spectral resolution. The limiting factor in this case is the resolution required to accurately characterise the peaks involved in the reaction. It is in these situations that using multiple acquisition coils should prove most effective.

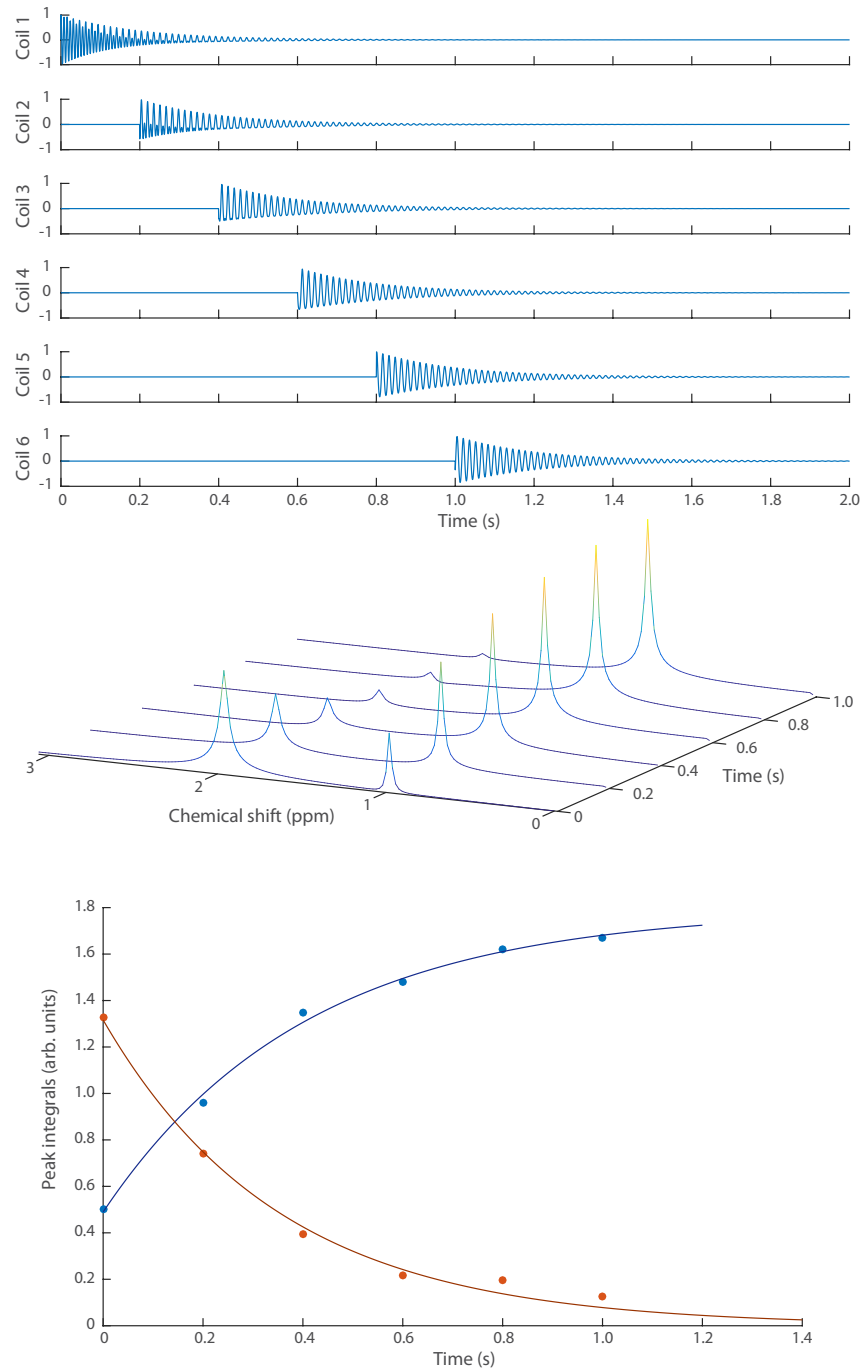*Figure 7.8: Simulated dynamics observed through a six-coil probe. TOP: The real components of the magnetisation in the x-y plane following NMR pulse. The FIDs were produced by sampling these dynamics. MIDDLE: The six spectra produced by simulated NMR acquisition. BOTTOM: Integrals of the spectral peaks are fitted with exponential curves to recover the initially defined rate parameter*

7.5 Determining pseudo rate coefficients with the six-coil probe

To test the ability of the six coil probe to determine rate coefficients of fast chemical reactions, an analogous non-chemical process was used. By flowing chemicals through a mixing vessel, a time-varying concentration gradient was produced. This time varying mixture was then guided through the six channel probe while NMR data were acquired.

7.5.1 Mixing cell design and characterisation

To produce a controllable pseudo-rate coefficient, two liquids were passed through a mixing vessel. If the first liquid is placed inside the mixing vessel and then a second liquid is pumped into it, the resultant out flow of liquid should contain a constantly varying combination of both liquids. During perfect mixing, the concentrations of the two liquids flowing out of the cell is an exponential change of the form shown in equation 7.6. In essence, the time variation of a such a flow can be an analogue for the stopped flow analysis of molecules that undergo the non-equilibrium exchange introduced in previous sections.

To produce a flow of consistently changing chemical concentration, a small mixing vessel was made that fitted to the top of the six-coil probe. This vessel was constructed of transparent perspex. Figure 7.9 shows the design of the cell along with initial fluid flow simulations produced in AutoDesk CFD (Autodesk - San Rafael, Ca, United States). The mixing vessel was simply a cylindrical 2 ml volume with an inlet and outlet at each end. The inlet and outlet were on opposite faces of the cylinder. The axes of the inlet and outlet were offset from one another to increase mixing performance. The streamlines shown in figure 7.9:c indicate the path of fluid flowing through the cell, this indicates that fluid injected through the inlet should not have the ability to flow straight out without mixing.

To test the mixing vessel, distilled water and water that contained green food colouring were flowed through the vessel. Initially the distilled water was placed inside the vessel and the green liquid was located in a 2 mm i.d. nylon tube fixed onto a syringe pump (Nexus 3000 - Chemyx). The syringe pump can precisely define a volumetric flow rate that can be used to define a pseudo rate coefficient

$$k = \frac{F}{V},\tag{7.10}$$

where F is the volumetric flow rate and V is the volume of the mixing vessel.

Setting up the apparatus outside the magnet allowed optical analysis of the mixing vessel performance with video at 120 fps (Apple iPhone 5S - Cupertino, USA) against a white background. This video was then analysed in MATLAB to extract how the green fluid mixed. Figure 7.10 shows the normalised increase of the green colour within the mixer volume. In this test, the volumetric flow rate of the syringe pump was set to 3 mL s^{-1} so that the pseudo rate coefficient was 1.5 s^{-1}.

7.5.2 Results using high concentration [1-^{13}C] Sodium Acetate

The mixing vessel was then used to test the ability of the six-coil probe to obtain dynamic information from thermally polarised NMR data. A 6 M [1-^{13}C] Sodium Acetate sample was placed in the mixing cell, above the six-coil probe in the 9.4 T lower iso-core. Distilled water was fed into the mixing vessel at a rate of 50 μL s^{-1}. This produced a decaying concentration curve with a pseudo reaction constant of 0.025 s^{-1}. The fluid flow rate was restricted to low values because at higher values, spins that are flipped during the NMR pulse would flow out of the coil's sensitive region before data acquisition.

NMR acquisition was limited to four of the six coils. A train of 6° pulses were applied to the flow of liquid and the FIDs were made of 5k complex points with
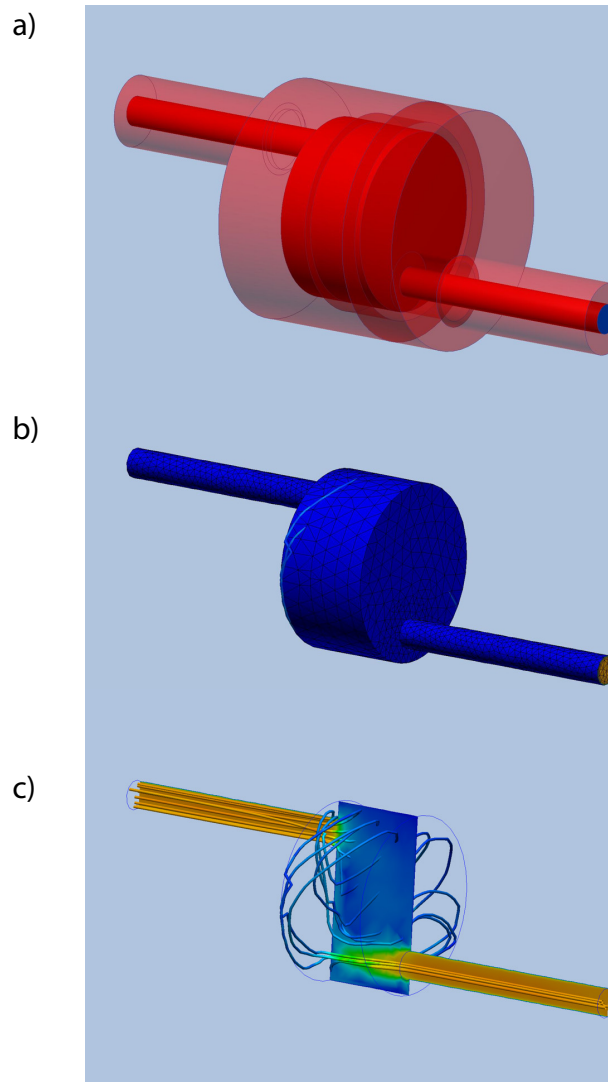
Figure 7.9: Geometry and analysis of small mixing vessel. a) The geometry of the mixer is shown in transparent red, the inner volume is shown in opaque red. b) The mesh constructed by AutoDesk CFD for fluid flow analysis. c) Results of fluid flow analysis, stream lines indicated the direction of fluid flow through the cell, the colour map of the slice indicates the magnitude of the fluid velocity.
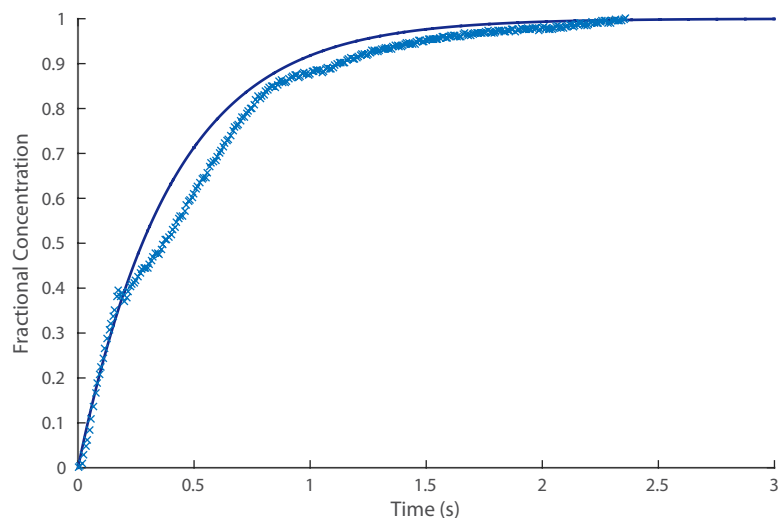
Figure 7.10: Distribution of green food colouring in the mixing vessel as a function of time. The mixing vessel was recorded at 120 fps and the video was analysed in MATLAB, the green RGB layer was extracted and the average green value across the mixing vessel was observed and then fitted with an expected build up curve. The equivalent decay curve is also included.

Coil	A	B	C	D
1	0.54 ± 0.07	0.036 ± 0.007	0.47 ± 0.07	0.003 ± 0.001
2	0.55 ± 0.09	0.028 ± 0.006	0.45 ± 0.09	0.003 ± 0.001
3	0.52 ± 0.11	0.027 ± 0.010	0.44 ± 0.12	0.003 ± 0.001
4	0.55 ± 0.06	0.034 ± 0.009	0.49 ± 0.08	0.003 ± 0.002
All data	0.53 ± 0.04	0.031 ± 0.008	0.47 ± 0.06	0.003 ± 0.001

Table 7.6: Fit coefficients for multi-coil acquisition of [1—^{13}C] Sodium Acetate with a varying concentration produced by the mixing vessel.

an acquisition duration of 100 ms. The FIDs where then apodised with a 20 Hz exponential window function prior to Fourier transform. Figure 7.11 shows the evolution of the normalised signal integral through the experiment. The data has been fitted with a double exponential curve of the form

$$\mathrm{f(t) = A \times exp\left(-Bt\right) + C \times exp\left(-Dt\right).} \tag{7.11}$$

The fit coefficients can be found in table 7.6. For each fit there are two distinct sets of dynamics. First there is a fast decay with time constants given in table 7.6 column B. Within error, these values fit with the predefined rate constant of 0.025. This implies that it is the first exponential decay which includes the dynamics associated with the variation of Sodium Acetate concentration. The additional exponential decays an order of magnitude slower than the first, however it is consistent between coils in both decay rate and amplitude. It is not clear where these additional dynamics arise from. However, as the sample is stored directly above the six-coil probe it is not in the homogeneous region of the lower iso-centre. Therefore it could be that the initial magnetisation of the ^{13}C spins will not be fully saturated.

The final row of table 7.6 shows the fit associated with all of the data together. Again, within error the fit agrees the predefined value, however the data as a whole is disappointing. Even with a high-concentration labelled sample, the maximum signal to noise was only around 9. As the concentration reduces over time, the signal quickly becomes unobservable. The six-coil probe is not sensitive enough for flow experiments such as this, however during stopped flow trials it is possible to acquire data with larger flip angle pulses, increasing the SNR. This is also not as much of a problem if hyperpolarised liquids are used.
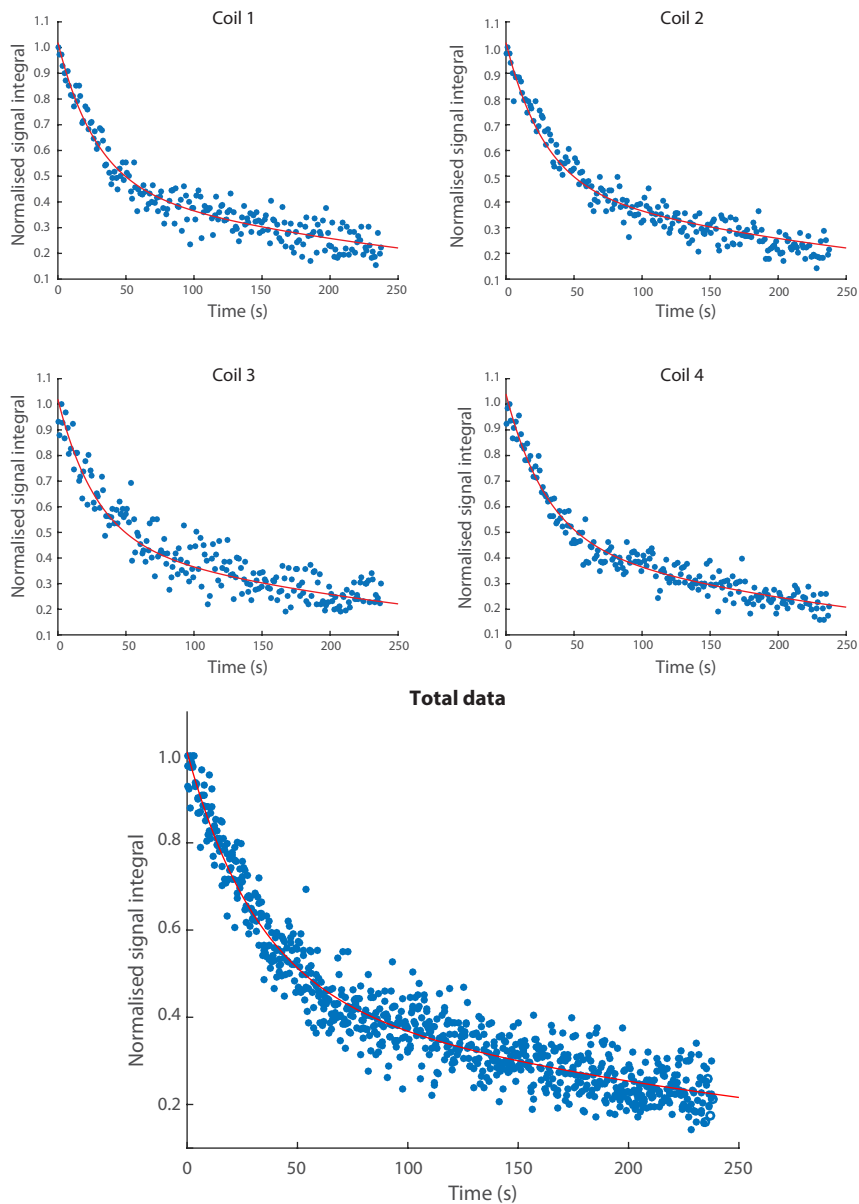
Figure 7.11: Fitted data showing the evolution of Sodium Acetate concentration as a function of time during determination of a pseudo rate coefficient. Each point represents the integral of the [1-^{13}C] peak observed following a 6° pulse observed on four of the six coils. Total data shows the fit extracted with all of the data included.

7.6 Dissolution DNP tests with the six-coil probe

7.6.1 Determining valve timings for six-coil probe

To reliably fill the six-coil flow path, the time taken for fluid to reach the probe outlet was measured. To do this, a capillary fluid sensor (TT electronics OCB350L062Z - Woking, UK) was placed on the tube just before the outlet at the bottom of the probe. The sensor passes light from a LED through the capillary towards a LDR. The sensor outputs a TTL voltage based on the presence ('high'= +5 V) or absence ('low'= 0 V) of fluid in the sensor region.

The LabVIEW control VI was modified so that the valves were automatically closed when the dissolution liquid reached the bottom of the probe. Room temperature dissolutions were performed ten times with the sensor in place. During these tests the driving pressure was maintained at 2.5 bar. The fluid arrived at the base of the probe after a time of 1030 ± 30 ms.

The fluid sensor gives accurate readings about how quickly fluid reaches the base of the probe, however it cannot provide information about the concentration of the dissolved sample in the capillary. When the hyperpolarised liquid reaches the TBO or BBI probe following dissolution, the sample concentration is averaged through mixing within the NMR probe. This is not the case for the six coil probe. Determining the distribution of dissolved sample along the six-coil flow path is important for maximising the signal produced by the dissolution experiment. Such measurements could be performed by incorporating an optical system that can measure the optical absorption of the fluid flowing through the capillary. This equipment was not available during the project.

7.6.2 Dissolution tests

Dissolution tests were performed on 2 M [1-^{13}C] Sodium Acetate samples with 15 mM Trityl in approx. 50:50 (by mass) water glycerol mixture. 20 μL aliquots were cooled to 1.7 K and polarised at a frequency of 93.86 GHz for one hour.

Following dissolution, a train of $\approx 20°$ pulses was applied simultaneously to each coil. The FIDs were acquired with 24k complex points over a duration of 300 ms. They were then zero-filled up to 48k points and apodised with a 16 Hz exponential function prior to Fourier transformation. A large apodisation window was required as there was significant electrical noise apparent on the spectra obtained with the probe. This noise was removed with significant smoothing of the data. The valves were open for a duration of 1030 ms, however NMR acquisition was started alongside the opening of the valves to determine whether any signal would be observed during sample transit. No signal was observed in the first three scans, indicating that the fluid is moving too quickly to be observed. The fourth scan, performed 200 ms after valve closing was the first to provide a signal, the resultant spectra can be seen in figure 7.12.

The spectra produced by dissolution DNP in the six-coil probe show significantly enhanced carbon signal. Direct enhancement was not calculated as a thermal signal from the dissolution sample could not be acquired in a reasonable time. However an estimate of the enhancement can be obtained by comparison to the high concentration sample observed in the previous section. The maximum signal to noise observed with the 6° pulse applied to the high concentration sample was 9. That sample was 6 M. To estimate the enhancement produced during the dissolution experiment an assumption needs to be made about the concentration of the sample at the coils following dissolution. If the dissolution into the six coil probe follows the dilution factor (1/40) introduced in previous chapters, then the sample concentration at the coil is around 50 mM. Using these parameters, an estimation

of the signal enhancement for each coil is provided in table 7.7. It is important to note that the enhancement produced by DNP and the temperature jump should be consistent for each coil, assuming that it the relative performance of each coil is the same. These values only provide an initial benchmark for performance of the experiment and should not be considered quantitative.

Coil	SNR	Line width (Hz)	Estimated enhancement	Decay constant (s)
1	100	45	3600	18.7±0.4
2	135	36	4900	12.9±0.4
3	99	46	3600	11.2±0.3
4	35	73	1200	8.2±0.2
5	110	35	4000	9.6±0.2

Table 7.7: Peak information following dissolution into the six-coil probe. The observed line widths are too large to take full advantage of the enhanced nuclear polarisation. The variation of the enhancement figure arises from the difference in performance between individual coils. The variation in the decay constants appears to arise from the discrepancy in flip angles produced by the individual coils. The decay constants shown here are a result of both the T_1 relaxation of the sample and the degradation of the magnetisation from the applied pulses. The discrepancy of these values arise from the uncertainty in the nutation angle produced by the pulses.

7.6.3 Determining T_1 relaxation with multiple coils

Measuring the T_1 relaxation of a hyperpolarised molecule can help determine the fluid dynamics following dissolution. This was introduced in section 5.8.3. The spectra produced by the dissolution experiment were integrated and analysed as a function of time. Figure 7.13 shows the signal decay. Even on first inspection it is clear that the data do not simply follow the T_1 relaxation of the carbon spins.

Figure 7.13 shows the signal decay as a function of time following dissolution into the six coil probe. Each data set was fitted with a mono-exponential decay and the decay constants are displayed in table 7.7. In dissolution tests into NMR tubes there is a small amount of additional dynamics caused by liquid motion within the
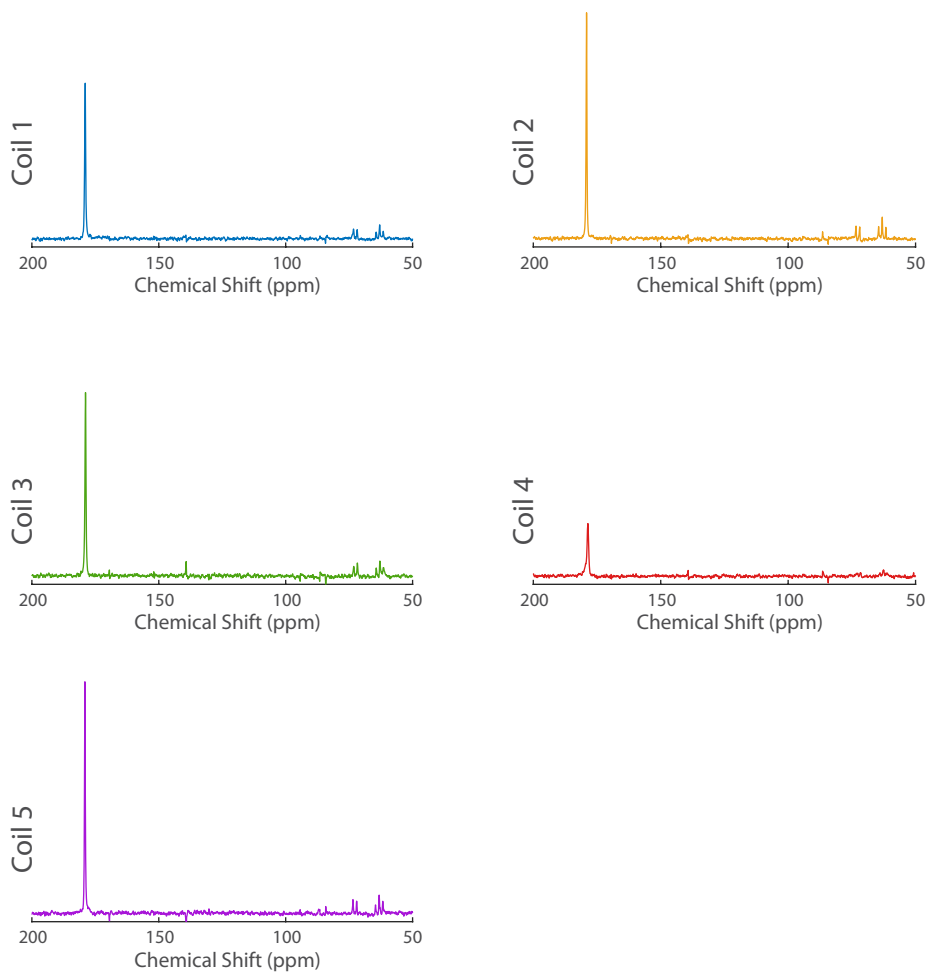
Figure 7.12: First spectra of each coil following dissolution DNP into the six-coil probe. The signal to noise levels of each coil are limited by the line width of the peak. Coil 4 demonstrates a line width of around 73 Hz. The data for each coil can be found in table 7.7. The variation in the line widths observed in each coil will produce a difference in the intensity of each peak, however the biggest form of variation is the performance of the coils, as they did not produced the flip angle expected in the set up of the experiment.

sample, however in such situations the T_1 relaxation is still the principle mechanism by which the signal decays. The decay constants displayed in table 7.7 are significantly shorter than were observed during previous experiments. The applied pulses are designed to perform a 20° nutation of the magnetisation vector during each scan, the decay of signal should be increased. By flipping the magnetisation through an angle θ a number of time times, the signal after the nth scan should be

$$S(n, t) = S_0 \sin(\theta) \cos(\theta)^{n-1} \exp\left(\frac{-t}{T_1}\right). \tag{7.12}$$

For the longitudinal relaxation, the signal decay is a function of time. The signal decay caused by the pulses is a function of number of previous scans. As the repetition time of the pulse sequence remains constant throughout the experiment the time variable can be substituted by the relation

$$t = T_R \cdot n, \tag{7.13}$$

where T_R is the repetition time of pulses. This allows the correct fitting of the signal fully as a function of number of previous scans. The pulses were set to produce a 20° nutation of the magnetisation, however by correcting for such pulses the does not produce a reliable fit.

There are two possible explanations for this discrepancy: First, the stopping of the flow is not entirely successful. If the filling of the probe is not complete then it could continue to flow once the Takasago valves have been closed. This would bring fresh hyperpolarised fluid into the sensitive coil region, increasing the lifetime of the observed signal. Second, the flip angle of the applied pulses are not as large as previously thought. The coils were tuned and the 90° pulses were calibrated with thermally polarised, spin-labelled sodium acetate present in the flow capillary. Differences between these conditions and those observed by the coils immediately could affect the coils performance by changing the tuning and matching characteristics of the resonant circuit. The inductance of the coil will be altered by changing

the dielectric constant of the region inside the coil. In turn the dielectric constant of the fluid will change with both radical concentration and temperature. It is unlikely that the relatively low radical concentration would be enough to change the tuning of the coil. The fluid observed during these scans could be up to 70° hotter than room temperature.

Experiments presented in the previous chapters have observed [1-^{13}C] sodium acetate carbonyl T_1 values of between 20 s and 46 s. So by assuming a longitudinal relaxation time in the region of these values it is possible to use equation 7.12 to determine an approximate value for the flip angle of the pulses produced by each coil. Figure 7.15 shows the nutation angles for each coil over a range of possible T_1 values. It is unlikely that the carbonyl longitudinal relaxation time falls outside of this range, therefore it was concluded that the nutation angle produced by the coil was not as large as originally estimated. To confirm this a more complete analysis of coil performance under experimental conditions is required.
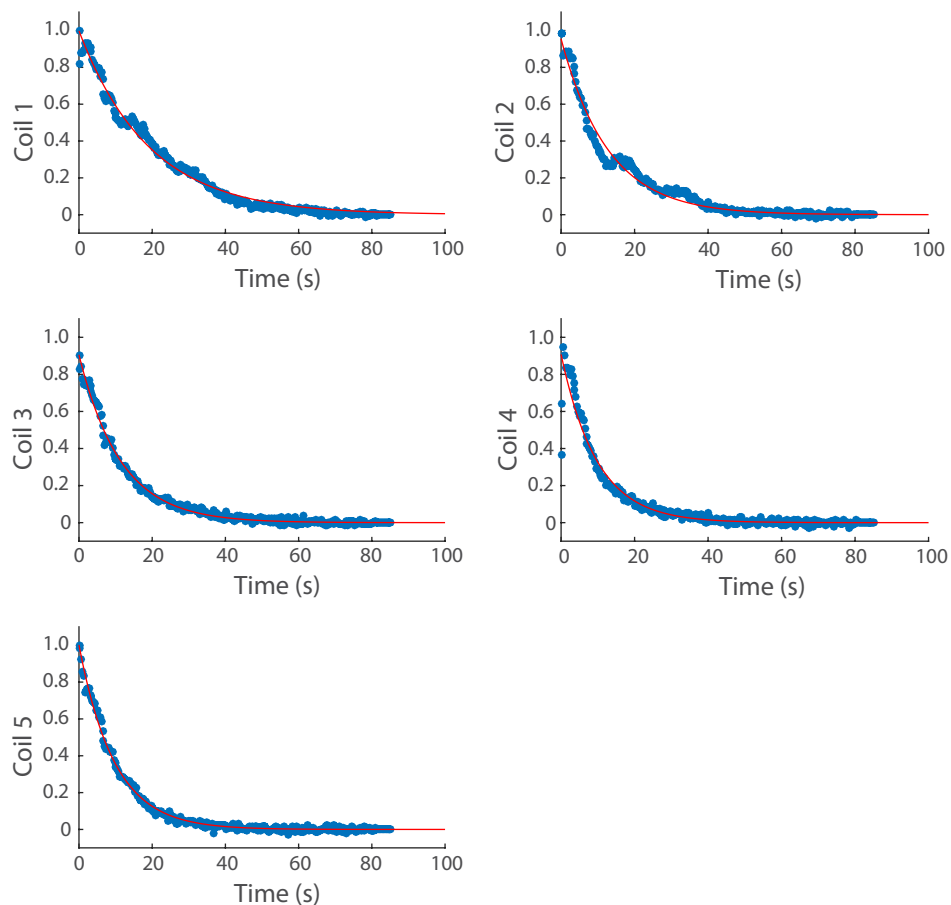
Figure 7.13: Decay curves of Sodium Acetate following dissolution into the six-coil probe. The mono-exponential fits of the 5 curves do not agree with the expected longitudinal relaxation of the [1-^{13}C] sodium acetate. The discrepancy of the decay of the data appears to be the result of the coils not performing as expected, and the pulses providing a nutation much lower than was intended. This could be as a result of the tuning and matching of the coils changing during the course of the dissolution experiment.
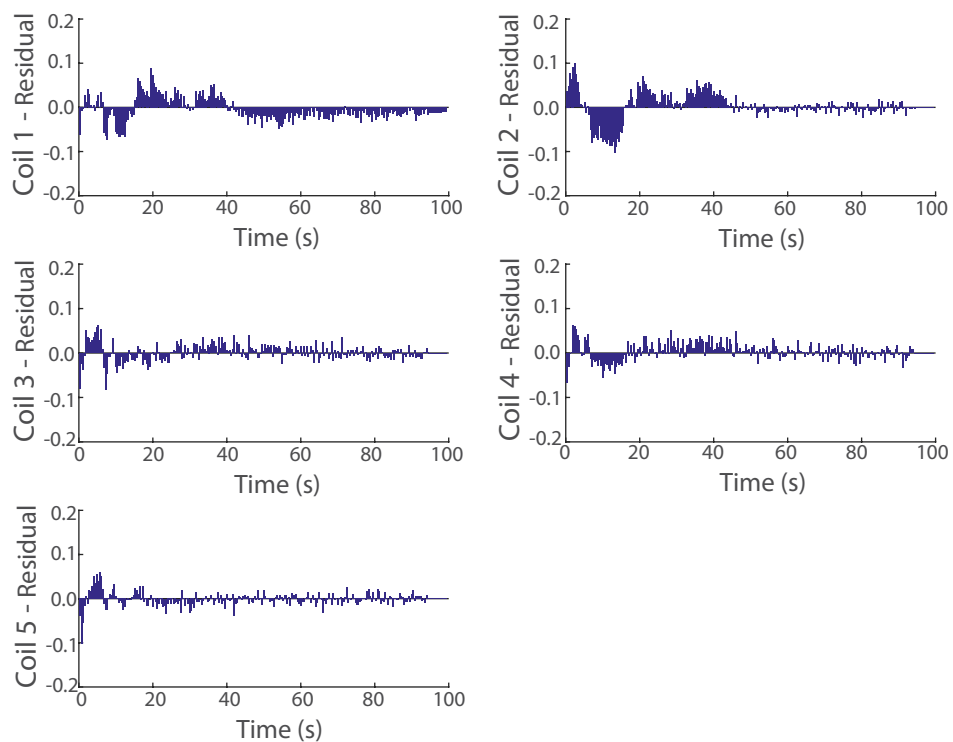
Figure 7.14: Residuals of the mono-exponential signal decay curves following sample dissolution. Coils one and two display similar slow oscillations to those observed in dissolutions into the TBO and BBI probes, however such dynamics do not explain the lifetime of the observed signals.
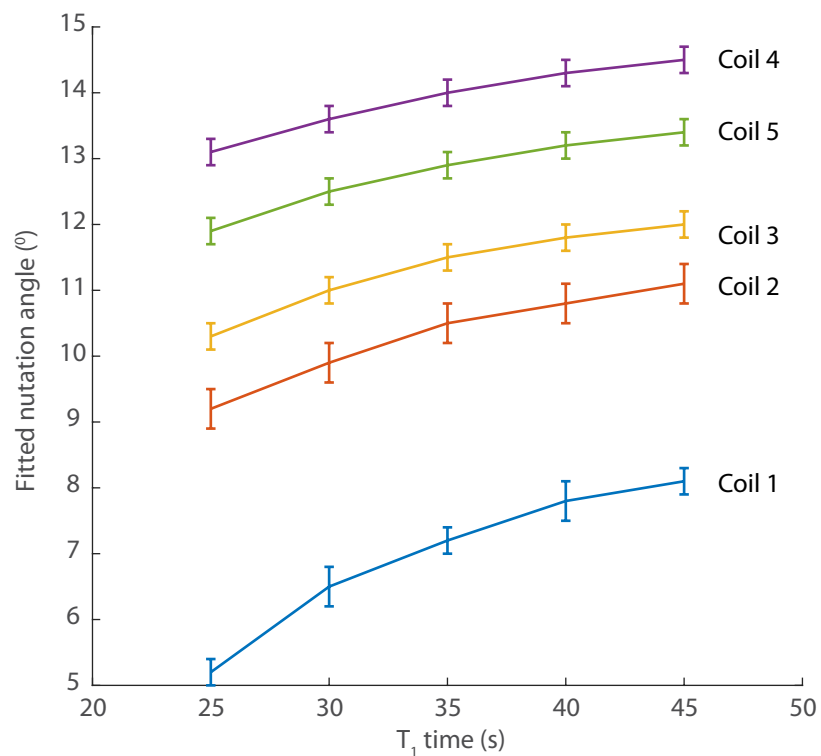
Figure 7.15: The flip angles calculated by fitting a decay model to the signal dynamics following dissolution into the six-coil probe. In this model rather than inserting a flip angle to correct the observed t_1 decay, a range of T_1 values have be used to extract possible flip angles from the un-optimised coils. The pulses were initially designed to flip the magnetisation by 20°, however across the whole range of possible relaxation times the maximum fitted nutation is around 14°.

7.7 Conclusion

This chapter presents the initial work carried out into setting up and analysing dissolution DNP in a six micro-coil probe head. Initial simulations and tests suggest that the six-coil probe should be useful in determining fast chemical dynamics through NMR experiments. The multi-coil Bloch-McConnell simulator could prove to be useful in the design and optimisation of stopped flow experiments. It could also easily be modified to incorporate hyperpolarised molecules.

The results presented in this chapter are very much preliminary testing of the apparatus. Further refinement of the system will be required before consistent and reliable data will be routine.

Attempts were made to use the six-coil probe to determine pseudo rate coefficients in thermally polarised samples. Within error, the predefined rate was successfully reconstructed, however low SNR meant that the observed error values were high. Hyperpolarised dissolution samples were successfully injected into the six-coil probe, however the injection process remains far from optimised. Questions remain as to the distribution of hyperpolarised sample though the probe flow path and to how well the flow is stopped prior to NMR scanning. Another current major disadvantage is that the line width of the observed spectra are far too wide to really take advantage of the increase in signal to noise produced by DNP. The cause of such massive line broadening is not currently clear as large field inhomogeneities are required to broaden resonances across such small diameter coils.

8

Conclusions

Over the last 20 years, DNP has developed into a principal research area for a number of groups around the world. A Google scholar search for DNP papers published in 1996 returns around 3,500 results, whereas by 2016 that number was over 23,000. This renaissance is in no small part down to the continued development of easily accessible microwave equipment.

DNP, for both NMR and MRI, is slowly becoming incorporated into biomedical research with potent diagnostic aspirations. Systems such as the SPINlab are bringing hyperpolarised fluids into human clinical trials. However, a truly revolutionary medical application, which justifies hardware and engineering difficulties, has yet to be realised. Even with its origins in the 1950s, DNP remains a *young* discipline.

One of the main open questions of DNP is how to make full use of the enhanced nuclear signal? This work attempts to, in a small way, help produce an answer to this question. While the results presented in this document are not necessarily ground-breaking, they do demonstrate the efficacy of the strategies and show that such methods are worthy of continued exploration.

The new dissolution system has been successfully set up for use with the dual iso-centre magnet. Through rigorous testing and refinement, it is now possible to deliver the hyperpolarised sample to a waiting NMR probe in 300 ms, though a liq-

uid settling time, of a further 300 ms, is required prior to NMR acquisition. This time remains the fastest recorded dissolution process for DNP experiments. Great strides have been made in improving the reliability of the system and only over the last few months has the use of the system become routine. One area in which the system struggles is the level of polarisation achieved in dissolution experiments. The build up curves obtained in the solid state suggest nuclear enhancements of the order of 50-80, resulting in an absolute polarisation of carbon spins of between $7.5 - 12\%$. These levels are low by modern DNP standards where polarisation levels of over 30% are commonplace [111] and maximal levels of over 70% have been seen in systems that exploit Cross Polarisation strategies [112].

The main cause of this lack of signal enhancement is the relatively high sample temperature during the polarisation stage. The VTI is capable of stable temperatures down to about 1.65 K, however other systems allow temperatures of close to 1 K. This reduction in temperature will have an appreciable effect on the efficiency of the DNP processes building up nuclear polarisation. Even with low solid state polarisation levels, the observed liquid state enhancement should be higher. For instance, with a solid state enhancement of 80, and a temperature jump from 1.6 K to 300 K, the observed liquid-state enhancement should be on the order of 15,000. However in practice we observed liquid-state enhancements of around a third of that value. This discrepancy could be down to the sample storage vessel during the polarisation stage. For the solid-state polarisation tests, the sample was housed in a dedicated solid-state probe. During the dissolution tests, this probe was replaced with the dissolution cup, which was design solely to increase the reliability of the dissolution process. It is not possible to monitor the solid-state polarisation build-up with this probe prior to dissolution. If a dissolution cup could be design so that could perform both of these tasks then more information about the performance of this set up could be acquired.

The concept of multi-nuclear DNP remains an unexplored, but relatively straight-

forward way of supplementing a dissolution-DNP experiment. This is especially true for molecules of interest that contain both carbon and nitrogen spins. It has been shown that this technique is sensitive enough to obtain both ^{13}C and ^{15}N spectra from molecules at natural abundance in a single scan. However, the real advantage of multi-nuclear DNP should be found using doubly spin labelled biologically relevant molecules. In such systems, the spins are easily observed with pulses of 1° and less. The experiments presented here show the power of the method to observe molecular dynamics from two spins simultaneously. Such a method could be used to monitor reaction dynamics such as chemical reactions or the conformational changes of biomolecules. Such experiments have been performed and documented by many groups, but analysing two spin species simultaneously should provide additional complimentary information that could prove useful in characterising dynamic processes. It should also be possible to combine multi-nuclear analysis with more advanced polarisation mechanisms such as cross colarisation (CP). Such methods would allow observations of sets of nuclei other than carbon and nitrogen and could extend the method to three or more species.

The experiments performed on the six-coil probe have been hindered by the field homogeneity observed at each coil and by inconsistencies in the fluid flow. True stopped-flow NMR has not been possible with the system in its current form. However, the inclusion of more advanced RF shielding between the coils has successfully eradicated the problem of coil-cross talk observed in the first generation probe. This has allowed the realisation of staggered NMR acquisition distributed across the coils. The simulation software which builds on the Bloch-McConnell equations demonstrated how a six-coil probe should be able to help in determining fast molecular dynamics and should prove useful in the characterisation and optimisation of future six-coil experiments.

Future work

The dissolution spectrometer is now in a reliable state and experiments can now push on in earnest. Presented here is an outline of the future work that could exploit the system and techniques outlined in this thesis.

There are a few ways of improving the level of polarisation obtained from solid-state DNP. First, chelates such as Gd^{3+} to increase electronic relaxation. This would increase the maximal polarisation level and decrease the build up time [113]. The added liquid state relaxation caused by the chelates would not significantly affect NMR acquisition because of the speed of the dissolution process. A more advanced step would be to modify the sample cup so that it can perform cross polarisation. This would massively increase the observed polarisation level and allow significantly more dissolution experiments to be performed on an experiment day.

The majority of the experiments presented in this thesis were performed with the most basic NMR pulse sequences. The first stage of developing experiments on this system is to reintroduce more sophisticated sequences to utilise the enhanced nuclear spin polarisation to extract more physical information. The speed at which the dissolution occurs allows these sequences to be applied to more molecules with shorter T_1 times. One such method is ultra-fast 2D spectroscopy, which could be incorporated to dissolution experiments [26, 114]. It could also be combined with double acquisition of ^{13}C and ^{15}N spin species. As the field inhomogeneities present in the dual iso-centre system are larger than those observed in other high-resolution systems, spin echo sequences could be used to reduce the observed spectral line widths.

To develop the experiments on the six-coil probe, there are a number of parameters that need to be optimised further. Initially, the reliability of the Takasago valves to the stop the flow of fluid needs to be tested further. A system that checks

the concentration of the incoming dissolved sample would also increase the performance of the delivery of hyperpolarised sample. As was suggested in the previous chapter, a system that could monitor the optical absorption of the fluid that passes through the capillary would be beneficial for sample delivery. This would also allow a much more refined optimisation of the solvent delivery pressure and valve timings in order to maximise the concentration of the hyperpolarised sample in the sensitive region of the flow-path. Testing needs to be performed that determines any changes of the electrical properties of the micro-coils during experimental conditions. Warm dissolutions could be performed while monitoring the coil resonance with the spectrometer or a network analyser. The current shim values obtained through the simplex algorithm need to be updated to minimise the line width observed during experiments. Other algorithms could also be tested to determine whether the performance of the simplex algorithm can be improved upon. Other methods of shimming, such as shim mapping are not possible without the development of a gradient system for the probe.

Bibliography

[1] A. W. Overhauser, "Polarization of nuclei in metals," *Physical Review*, vol. 92, no. 2, pp. 411–415, 1953.

[2] A. Abragam and M. Goldman, "Principles of dynamic nuclear polarisation," *Reports Prog. Phys.*, vol. 41, pp. 395–467, 3 1978.

[3] a. Abragam and M. Goldman, "Nuclear magnetism: Order and disorder," *Nuclear magnetism: Order and disorder*, pp. +626., 1982.

[4] J. H. Ardenkjaer-Larsen, B. Fridlund, A. Gram, G. Hansson, L. Hansson, M. H. Lerche, R. Servin, M. Thaning, and K. Golman, "Increase in signal-to-noise ratio of > 10,000 times in liquid-state NMR.," *Proceedings of the National Academy of Sciences of the United States of America*, vol. 100, pp. 10158–63, 9 2003.

[5] M. H. Levitt, *Spin Dynamics: Basics of Nuclear Magnetic Resonance*. Wiley, 2000.

[6] E. M. Purcell, "Research in Nuclear Magnetism.," *Science (New York, N.Y.)*, vol. 118, no. 3068, pp. 431–436, 1953.

[7] A. H. Morrish, *The Physical Principles of Magnetism*, vol. 1. 1965.

[8] M. Planck, "Ueber das Gesetz der Energieverteilung im Normalspectrum," *Annalen der Physik*, vol. 309, no. 3, pp. 553–563, 1901.

[9] W. Pauli, "Über den Zusammenhang des Abschlusses der Elektronengruppen im Atom mit der Komplexstruktur der Spektren," *Zeitschrift für Physik*, vol. 31, no. 1, pp. 765–783, 1925.

[10] A. Belyaev, "Chapter 5 Nuclear Shell Model," *Nuclei and Particles - Course notes*, vol. Chapter 5, pp. 35–44.

[11] W. Gerlach and O. Stern, "Der experimentelle Nachweis der Richtungsquantelung im Magnetfeld," *Zeitschrift f??r Physik*, vol. 9, no. 1, pp. 349–352, 1922.

[12] D. R. Lide, "CRC Handbook of Chemistry and Physics, 96th Edition, 2015-2016," *Handbook of Chemistry and Physics*, 2016.

[13] M. Brustolon and E. Giamello, *Electron Paramagnetic Resonance: A Practitioner's Toolkit.* 2008.

[14] M. J. N. Junk, "Electron Paramagnetic Resonance Theory," *Assessing the Functional Structure of Molecular Transporters by EPR Spectroscopy*, pp. 1–42, 2012.

[15] S. a. Dzuba and A. Kawamori, "Selective Hole Burning in EPR: Spectral Diffusion and Dipolar Broadening," *Concepts in Magnetic Resonance*, vol. 8, pp. 49–61, 1996.

[16] S. A. Dzuba, Y. Kodera, H. Hara, and A. Kawamori, "The use of selective hole burning in EPR spectra to study spectral," *Journal Of Magnetic Resonance Series A*, vol. 102, no. 2, pp. 257–260, 1993.

[17] W. B. Mims, K. Nassau, and J. D. McGee, "Spectral diffusion in electron resonance lines," *Physical Review*, vol. 123, no. 6, pp. 2059–2069, 1961.

[18] D. J. Kubicki, G. Casano, M. Schwarzwalder, S. Abel, C. Sauvee, K. Ganesan, M. Yulikov, A. J. Rossini, G. Jeschke, C. Coperet, A. Lesage, P. Tordo, O. Ouari, and L. Emsley, "Rational design of dinitroxide biradicals for efficient cross-effect dynamic nuclear polarization," *Chemical Science*, vol. 7, no. 1, pp. 550–558, 2016.

[19] F. Bloch, "Nuclear induction," *Physical Review*, vol. 70, no. 7-8, pp. 460–474, 1946.

[20] A. G. Redfield, "On the Theory of Relaxation Processes," *IBM Journal of Research and Development*, vol. 1, no. 1, pp. 19–31, 1957.

[21] D. Canet and I. Nancy, "General theory of nuclear relaxation," *Advances in Inorganic Chemistry*, vol. 57, no. 05, pp. 3–40, 2005.

[22] G. B. Chavhan, P. S. Babyn, B. Thomas, M. M. Shroff, and E. M. Haacke, "Principles, Techniques, and Applications of T2*-based MR Imaging and Its Special Applications1," *RadioGraphics*, vol. 29, no. 5, pp. 1433–1449, 2009.

[23] D. ter Haar, "Theory and applications of the density matrix," *Reports on Progress in Physics*, vol. 24, no. 1, p. 304, 1961.

[24] D. J. Griffiths, *Introduction to Quantum Mechanics*, vol. 1. 2005.

[25] Y. Hovav, A. Feintuch, and S. Vega, "Dynamic nuclear polarization assisted spin diffusion for the solid effect case," *Journal of Chemical Physics*, vol. 134, p. 074509, 2 2011.

[26] A. Van der Drift, *Progress in DNP Theory and Hardware*. PhD thesis, University of Nottingham, 2012.

[27] T. Claridge, *The Basics of Fourier Transform NMR Spectroscopy*. No. October, 2009.

[28] T. R. Carver and C. P. Slichter, "Polarization of nuclear spins in metals [15]," 1953.

[29] L. R. Becerra, G. J. Gerfen, R. J. Temkin, D. J. Singel, and R. G. Griffin, "Dynamic nuclear polarization with a cyclotron resonance maser at 5 T," *Physical Review Letters*, vol. 71, no. 21, pp. 3561–3564, 1993.

[30] S. Bowen and J. H. Ardenkjaer-Larsen, "Enhanced performance large volume dissolution-DNP," *Journal of Magnetic Resonance*, vol. 240, pp. 90–94, 2014.

[31] D. Shimon, Y. Hovav, A. Feintuch, D. Goldfarb, and S. Vega, "Dynamic Nuclear Polarization in the solid state: a transition between the cross effect and the solid effect." *Physical chemistry chemical physics : PCCP*, vol. 14, no. 16, pp. 5729–43, 2012.

[32] Y. Hovav, A. Feintuch, and S. Vega, "Theoretical aspects of dynamic nuclear polarization in the solid state–spin temperature and thermal mixing." *PCCP Phys. Chem. Chem. Phys.*, vol. 15, no. 1, pp. 188–203, 2013.

[33] Y. Hovav, A. Feintuch, and S. Vega, "Theoretical aspects of dynamic nuclear polarization in the solid state - The cross effect," *Journal of Magnetic Resonance*, vol. 214, pp. 29–41, 1 2012.

[34] K. N. Hu, C. Song, H. H. Yu, T. M. Swager, and R. G. Griffin, "High-frequency dynamic nuclear polarization using biradicals: A multifrequency EPR lineshape analysis," *Journal of Chemical Physics*, vol. 128, no. 5, 2008.

[35] P. J. Roberts, "EPR Relaxation: Progress in Hardware and Analysis Methods," *PhD Thesis*, 2014.

[36] S. Jannin, A. Comment, and J. J. van der Klink, "Dynamic Nuclear Polarization by Thermal Mixing Under Partial Saturation," *Applied Magnetic Resonance*, vol. 43, no. 1-2, pp. 59–68, 2012.

[37] M. Goldman, "Overview of spin temperature, thermal mixing and dynamic nuclear polarization," *Applied Magnetic Resonance*, vol. 34, pp. 219–226, 8 2008.

[38] E. D. Becker, "A brief history of nuclear magnetic resonance." *Analytical Chemistry*, vol. 65, no. 6, pp. 295A–302A, 1993.

[39] E. Fukushima and N. Boden, *Experimental pulse NMR: A nuts and bolts approach*, vol. 10. 1982.

[40] S. A. Richards and J. C. Hollerton, "Essential Practical NMR for Organic Chemistry," 2010.

[41] W. Hull, "NMR Tips for Shimming, part 2 - Computerized shimming with the Simplex algorithm," tech. rep., Bruker.

[42] J. Carpenter, "Understanding electromagnetism," *Engineering Science and Education Journal*, vol. 2, no. 4, p. 273, 1993.

[43] D. I. Hoult and R. E. Richards, "The signal-to-noise ratio of the nuclear magnetic resonance experiment," *Journal of Magnetic Resonance (1969)*, vol. 24, no. 1, pp. 71–85, 1976.

[44] D. M. Hoang, E. B. Voura, C. Zhang, L. Fakri-Bouchet, and Y. Z. Wadghiri, "Evaluation of coils for imaging histological slides: Signal-to-noise ratio and filling factor," *Magnetic Resonance in Medicine*, vol. 71, no. 5, pp. 1932–1943, 2014.

[45] J. B. Johnson, "Thermal agitation of electricity in conductors," *Physical Review*, vol. 32, no. 1, pp. 97–109, 1928.

[46] Bruker, "State-of-the-art sensitivity with CryoProbe™ products."

[47] V. D. Kodibagkar and M. S. Conradi, "Remote tuning of NMR probe circuits.," *Journal of magnetic resonance (San Diego, Calif. : 1997)*, vol. 144, no. 1, pp. 53–57, 2000.

[48] A. Heerschap, M. G. Sommers, H. ⊠. Zandt, W. K. J. Renema, A. A. Veltien, and D. W. J. Klomp, "Nuclear Magnetic Resonance in Laboratory Animals," in *Imaging in Biological Research, Part A* (B. T. M. i. Enzymology, ed.), vol. Volume 385, pp. 41–63, Academic Press, 2004.

[49] P. Goldsmith, "Quasioptical Systems, 1998," *IEEE Press*, pp. 1–6, 1998.

[50] P. Cruickshank, D. Bolton, D. Robertson, R. Wylde, and G. Smith, "Reducing standing waves in quasi-optical systems by optimal feedhorn design," *2007 Joint 32nd International Conference on Infrared and Millimeter Waves and the 15th International Conference on Terahertz Electronics*, vol. 0044, no. 0, pp. 1–2, 2007.

[51] R. I. Hunter, D. A. Robertson, P. Goy, and G. M. Smith, "Design of high-performance millimeter wave and sub-millimeter wave quasi-optical isolators and circulators," *IEEE Transactions on Microwave Theory and Techniques*, vol. 55, no. 5, pp. 890–897, 2007.

[52] J. Leggett, R. Hunter, J. Granwehr, R. Panek, A. J. Perez-Linde, A. J. Horsewill, J. McMaster, G. Smith, and W. Köckenberger, "A dedicated spectrometer for dissolution DNP NMR spectroscopy," *Physical Chemistry Chemical Physics*, vol. 12, no. 22, pp. 5883–5892, 2010.

[53] D. Pozar, *Microwave Engineering Fourth Edition*. 2005.

[54] M. P. DeLisio and R. A. York, "Quasi-optical and spatial power combining," 2002.

[55] J. Keeler, "Understanding NMR spectroscopy," tech. rep., University of Cambridge, Cambridge, 2002.

[56] M. Balci, "Basic 1H- and 13C-NMR Spectroscopy," *Basic 1H- and 13C-NMR Spectroscopy*, pp. 3–8, 2005.

[57] A. Shaka, "Decoupling Methods," in *Encyclopedia of NMR* (R. Harris and R. Wasylishen, eds.), pp. 1558–1563, 2012.

[58] S. Jannin, L. Helm, and G. Bodenhausen, "NMR of Insensitive Nuclei Enhanced by Dynamic Nuclear Polarization," *CHIMIA International Journal for Chemistry*, vol. 65, pp. 260–263, 4 2011.

[59] R. Balzan, L. Fernandes, A. Comment, L. Pidial, B. Tavitian, and P. R. Vasos, "Dissolution Dynamic Nuclear Polarization Instrumentation for Real-time Enzymatic Reaction Rate Measurements by NMR.," *Journal of visualized experiments : JoVE*, no. 108, 2016.

[60] J. H. Ardenkjaer-Larsen, S. MacHoll, and H. Jóhannesson, "Dynamic nuclear polarization with trityls at 1.2 K," *Applied Magnetic Resonance*, vol. 34, no. 3-4, pp. 509–522, 2008.

[61] A. Bornet and S. Jannin, "Optimizing dissolution dynamic nuclear polarization," *Journal of Magnetic Resonance*, vol. 264, pp. 13–21, 2016.

[62] W. Meyer, J. Heckmann, C. Hess, E. Radtke, G. Reicherz, L. Triebwasser, and L. Wang, "Dynamic polarization of 13C nuclei in solid 13C labeled pyruvic acid," *Nuclear Instruments and Methods in Physics Research, Section A: Accelerators, Spectrometers, Detectors and Associated Equipment*, vol. 631, no. 1, pp. 1–5, 2011.

[63] A. Kiswandhi, P. Niedbalski, C. Parish, P. Kaur, A. Martins, L. Fidelino, C. Khemtong, L. Song, A. D. Sherry, and L. Lumata, "Impact of Ho 3+ - doping on 13 C dynamic nuclear polarization using trityl OX063 free radical," *Phys. Chem. Chem. Phys.*, vol. 18, no. 31, pp. 21351–21359, 2016.

[64] E. Ravera, D. Shimon, A. Feintuch, D. Goldfarb, S. Vega, A. Flori, C. Luchinat, L. Menichetti, and G. Parigi, "The effect of Gd on trityl-based dynamic nuclear polarisation in solids," *Phys Chem Chem Phys*, vol. 17, no. 40, pp. 26969–26978, 2015.

[65] L. Lumata, M. E. Merritt, C. R. Malloy, A. D. Sherry, and Z. Kovacs, "Impact of Gd 3+ on DNP of [1- 13C]pyruvate doped with trityl OX063, BDPA, or 4-oxo-TEMPO," 2012.

[66] M. Batel, M. Krajewski, A. Däpp, A. Hunkeler, B. H. Meier, S. Kozerke, and M. Ernst, "Dissolution dynamic nuclear polarization efficiency enhanced

by Hartmann-Hahn cross polarization," *Chemical Physics Letters*, vol. 554, pp. 72–76, 2012.

[67] S. Jannin, A. Bornet, S. Colombo, and G. Bodenhausen, "Low-temperature cross polarization in view of enhancing dissolution Dynamic Nuclear Polarization in NMR," *Chemical Physics Letters*, vol. 517, no. 4-6, pp. 234–236, 2011.

[68] A. J. P. Linde, A. Bornet, J. Milani, B. Vuichoud, R. Melzi, S. Jannin, and G. Bodenhausen, "Cross polarization from 1H to quadrupolar 6Li nuclei for dissolution DNP," *Physical Chemistry Chemical Physics*, vol. 16, no. 45, pp. 24813–24817, 2014.

[69] A. J. Perez Linde, *No Title*. PhD thesis, University of Nottingham, 2010.

[70] Y. Hovav, A. Feintuch, S. Vega, and D. Goldfarb, "Dynamic nuclear polarization using frequency modulation at 3.34 T," *Journal of Magnetic Resonance*, vol. 238, pp. 94–105, 2014.

[71] A. Bornet, J. Milani, B. Vuichoud, A. J. Perez Linde, G. Bodenhausen, and S. Jannin, "Microwave frequency modulation to enhance Dissolution Dynamic Nuclear Polarization," *Chemical Physics Letters*, vol. 602, pp. 63–67, 2014.

[72] M. L. Guy, L. Zhu, and C. Ramanathan, "Design and characterization of a W-band system for modulated DNP experiments," *Journal of Magnetic Resonance*, vol. 261, pp. 11–18, 2015.

[73] R. I. Hunter, P. A. S. Cruickshank, D. R. Bolton, P. C. Riedi, and G. M. Smith, "High power pulsed dynamic nuclear polarisation at 94 GHz.," *Physical Chemistry Chemical Physics*, vol. 12, no. 22, pp. 5752–5756, 2010.

[74] A. Henstra and W. Wenckebach, "The theory of nuclear orientation via electron spin locking (NOVEL)," *Molecular Physics*, vol. 106, no. 7, pp. 859–871, 2008.

[75] T. V. Can, J. J. Walish, T. M. Swager, and R. G. Griffin, "Time domain DNP with the NOVEL sequence," *The Journal of Chemical Physics*, vol. 143, no. 5, p. 054201, 2015.

[76] M. Batel, M. Krajewski, K. Weiss, O. With, A. Däpp, A. Hunkeler, M. Gimersky, K. P. Pruessmann, P. Boesiger, B. H. Meier, S. Kozerke, and M. Ernst, "A multi-sample 94 GHz dissolution dynamic-nuclear-polarization system," *Journal of Magnetic Resonance*, vol. 214, pp. 166–174, 2012.

[77] M. Krajewski, P. Wespi, J. Busch, L. Wissmann, G. Kwiatkowski, J. Steinhauser, M. Batel, M. Ernst, and S. Kozerke, "A multisample dissolution dynamic nuclear polarization system for serial injections in small animals," 2016.

[78] C.-G. Joo, K.-N. Hu, J. A. Bryant, and R. G. Griffin, "In situ temperature jump high frequency dynamic nuclear polarization experiments: enhanced sensitivity in liquid state NMR spectroscopy," *Journal of the American Chemical Society*, vol. 128, no. 29, pp. 9428–9432, 2006.

[79] S. Bowen and J. H. Ardenkjaer-Larsen, "Enhanced performance large volume dissolution-DNP.," *Journal of magnetic resonance (San Diego, Calif. : 1997)*, vol. 240, no. January, pp. 90–4, 2014.

[80] T. Harris, C. Bretschneider, and L. Frydman, "Dissolution DNP NMR with solvent mixtures: Substrate concentration and radical extraction," *Journal of Magnetic Resonance*, vol. 211, no. 1, pp. 96–100, 2011.

[81] J. Milani, B. Vuichoud, A. Bornet, P. Miéville, R. Mottier, S. Jannin, and G. Bodenhausen, "A magnetic tunnel to shelter hyperpolarized fluids," *Review of Scientific Instruments*, vol. 86, no. 2, 2015.

[82] M. Mishkovsky and L. Frydman, "Principles and progress in ultrafast multidimensional nuclear magnetic resonance.," *Annual review of physical chemistry*, vol. 60, pp. 429–48, 1 2009.

[83] P. Giraudeau and L. Frydman, "Ultrafast 2D NMR: An Emerging Tool in Analytical Spectroscopy," *Annual Review of Analytical Chemistry*, vol. 7, no. 1, pp. 129–161, 2014.

[84] K. J. Donovan and L. Frydman, "HyperSPASM NMR: A new approach to single-shot 2D correlations on DNP-enhanced samples," *Journal of Magnetic Resonance*, vol. 225, pp. 115–119, 2012.

[85] I. J. Day, J. C. Mitchell, M. J. Snowden, and A. L. Davis, "Co-acquisition of hyperpolarised 13C and 15N NMR spectra.," *Magnetic resonance in chemistry : MRC*, vol. 45, no. 12, pp. 1018–1021, 2007.

[86] Comsol-Multiphysics: Cyclopedia, "The Joule-Thomson Effect," 2016.

[87] J. Granwehr, R. Panek, J. Leggett, and W. Köckenberger, "Quantifying the transfer and settling in NMR experiments with sample shuttling," *Journal of Chemical Physics*, vol. 132, no. 24, 2010.

[88] M. Brown, R. Semelka, and T. K. Nishino, *MRI: Basic Principles and Applications, 3rd edition*, vol. 31. 2004.

[89] P. Niedbalski, C. Parish, A. Kiswandhi, Z. Kovacs, and L. Lumata, "Influence of 13C Isotopic Labeling Location on Dynamic Nuclear Polarization of Acetate," *The Journal of Physical Chemistry A*, vol. 121, pp. 3227–3233, 5 2017.

[90] D. Shimon, Y. Hovav, I. Kaminker, A. Feintuch, D. Goldfarb, and S. Vega, "Simultaneous DNP enhancements of 1H and 13C nuclei: Theory and experiments," *Physical Chemistry Chemical Physics*, vol. 17, no. 17, pp. 11868–11883, 2015.

[91] Y. Hamuro, S. J. Coales, M. R. Southern, J. F. Nemeth-Cawley, D. D. Stranz, and P. R. Griffin, "Rapid analysis of protein structure and dynamics by hydrogen/deuterium exchange mass spectrometry.," *Journal of biomolecular techniques : JBT*, vol. 14, no. 3, pp. 171–182, 2003.

[92] W. de Boer, "Dynamic orientation of nuclei at low temperatures," *Journal of Low Temperature Physics*, vol. 22, no. 1-2, pp. 185–212, 1976.

[93] M. Afeworki, R. a. McKay, and J. Schaefer, "Selective observation of the interface of heterogeneous polycarbonate/polystyrene blends by dynamic nuclear polarization carbon-13 NMR spectroscopy," *Macromolecules*, vol. 25, no. 16, pp. 4084–4091, 1992.

[94] J. H. Ardenkjaer-Larsen, A. M. Leach, N. Clarke, J. Urbahn, D. Anderson, and T. W. Skloss, "Dynamic nuclear polarization polarizer for sterile use intent," *NMR in Biomedicine*, vol. 24, no. 8, pp. 927–932, 2011.

[95] B. Vuichoud, E. Canet, J. Milani, A. Bornet, D. Baudouin, L. Veyre, D. Gajan, L. Emsley, A. Lesage, C. Cop??ret, C. Thieuleux, G. Bodenhausen, I. Koptyug, and S. Jannin, "Hyperpolarization of Frozen Hydrocarbon Gases by Dynamic Nuclear Polarization at 1.2 K," *Journal of Physical Chemistry Letters*, vol. 7, no. 16, pp. 3235–3239, 2016.

[96] E. Kupče, R. Freeman, and B. K. John, "Parallel acquisition of two-dimensional NMR spectra of several nuclear species," *Journal of the American Chemical Society*, vol. 128, no. 30, pp. 9606–9607, 2006.

[97] E. Kupče and R. Freeman, "Molecular structure from a single NMR experiment," *Journal of the American Chemical Society*, vol. 130, no. 32, pp. 10788–10792, 2008.

[98] K. Kawahara and C. Tanford, "Viscosity and density of aqueous solutions of urea and guanidine hydrochloride.," *Journal of Biological Chemistry*, vol. 241, no. 13, pp. 3228–3232, 1966.

[99] S. J. Kharat, "Density, viscosity and ultrasonic velocity studies of aqueous solutions of sodium acetate at different temperatures," *Journal of Molecular Liquids*, vol. 140, no. 1-3, pp. 10–14, 2008.

[100] A. J. Horsewill and S. M. M. Abu-Khumra, "Dynamic tunneling polarization as a quantum rotor analogue of dynamic nuclear polarization and the NMR solid effect," *Physical Review Letters*, vol. 107, no. 12, 2011.

[101] C. Ludwig, M. Saunders, I. Marin-Montesinos, and U. L. Gunther, "Quantum rotor induced hyperpolarization," *Proceedings of the National Academy of Sciences*, vol. 107, no. 24, pp. 10799–10803, 2010.

[102] G. A. Webb, *Modern Magnetic Resonance*. 2006.

[103] A. J. Perez Linde, "Application of cross polarisation techniques to dynamic nuclear polarisation dissolution experiments," no. November, 2010.

[104] H. Wang, L. Ciobanu, A. S. Edison, and A. G. Webb, "An eight-coil high-frequency probehead design for high-throughput nuclear magnetic resonance spectroscopy," *Journal of Magnetic Resonance*, vol. 170, pp. 206–212, 10 2004.

[105] H. Wang, L. Ciobanu, and A. Webb, "Reduced data acquisition time in multi-dimensional NMR spectroscopy using multiple-coil probes," *Journal of Magnetic Resonance*, vol. 173, no. 1, pp. 134–139, 2005.

[106] G. Fisher, C. Petucci, E. MacNamara, and D. Raftery, "NMR probe for the simultaneous acquisition of multiple samples." *Journal of magnetic resonance (San Diego, Calif. : 1997)*, vol. 138, pp. 160–3, 5 1999.

[107] T. Hou, E. MacNamara, and D. Raftery, "NMR analysis of multiple samples using parallel coils: Improved performance using reference deconvolution and multidimensional methods," *Analytica Chimica Acta*, vol. 400, pp. 297–305, 11 1999.

[108] R. L. Haner and P. A. Keifer, "Flow Probes for NMR Spectroscopy," in *eMagRes*, John Wiley & Sons, Ltd, 2007.

[109] S. A. Richards and J. C. Hollerton, "Spectrum Acquisition," in *Essential Practical NMR for Organic Chemistry*, pp. 23–31, John Wiley & Sons, Ltd, 2010.

[110] M. Helgstrand, T. Hard, and P. Allard, "Simulations of NMR pulse sequences during equilibrium and non-equilibrium chemical exchange," *Journal of Biomolecular NMR*, vol. 18, no. 1, pp. 49–63, 2000.

[111] R. R. Rizi, "A new direction for polarized carbon-13 MRI.," *Proceedings of the National Academy of Sciences of the United States of America*, vol. 106, no. 14, pp. 5453–5454, 2009.

[112] S. Jannin, A. Bornet, R. Melzi, and G. Bodenhausen, "High field dynamic nuclear polarization at 6.7 T: Carbon-13 polarization above 70% within 20 min," *Chemical Physics Letters*, vol. 549, pp. 99–102, 10 2012.

[113] J. W. Gordon, S. B. Fain, and I. J. Rowland, "Effect of lanthanide ions on dynamic nuclear polarization enhancement and liquid-state T1 relaxation," *Magnetic Resonance in Medicine*, vol. 68, no. 6, pp. 1949–1954, 2012.

[114] L. Frydman and D. Blazina, "Ultrafast two-dimensional nuclear magnetic resonance spectroscopy of hyperpolarized solutions," *Nature Physics*, vol. 3, no. 6, pp. 415–419, 2007.

A note on the production of this thesis

This document was produced in LaTeX on the Overleaf online typesetting platform. All diagrams were produced in Adobe Illustrator CS6. All data was processed in MATLAB R2016a then exported to Illustrator for aesthetic modifications. NMR data was collected through TopSPIN 3.2 (pl3). Chemical structures were created in ChemDraw Professional 15.1. All figures presented were made by me unless expressly stated in the figure caption.